Radio Frequency Detector Arrays for High-Field Magnetic Resonance Imaging

by

Atefeh Kordzadeh

A thesis submitted in partial fulfillment of the requirements for the degree of

Doctor of Philosophy

Departments of Biomedical Engineering
and
Electrical and Computer Engineering
University of Alberta

Abstract

In magnetic resonance imaging (MRI), radio frequency (RF) detectors or "coils" are used to excite and receive signal from the nuclear spins. This thesis focuses on the design and development of RF coils and methods to achieve the best possible image quality at high static magnetic field strengths ($\mathbf{B}_0$). The coils are designed to operate at 200 MHz (4.7 tesla) for the human MRI system located in the Peter S. Allen MR Research Centre at the University of Alberta. This intermediate field strength is beneficial for body imaging because it takes advantage of MRI at fields that are higher than those of standard clinical scanners (1.5 T and 3 T) while avoiding the severe challenges of imaging deep targets in the body (e.g., torso, abdomen and pelvis) at ultra-high fields (7 T and 9.4 T). The image quality benefits of high-field MRI include higher signal-to-noise ratio (SNR), while the challenges are due to the short wavelength which introduces bright and dark areas in the images (respectively, constructive and destructive interference of RF fields). Moreover, due to the RF losses inside tissues, the penetration depth of the RF fields is significantly lower at higher $\mathbf{B}_0$ fields. The objective of this thesis is to address and overcome these issues and technical challenges to achieve high image quality (resolution, SNR and uniformity) while keeping the RF power deposition (SAR) values within acceptable limits.

High dielectric constant (HDC) pads or liners have been proposed in the literature to increase RF field homogeneity in the imaging region. The effects of HDC pads on the transmission and safety performance of an array are discussed in **chapter 2**, where it is found that there is an optimal value for the dielectric constant of the pads which is much lower than that currently used in the literature. Using HDC pads increases the magnetic field however it can affect SAR, matching and mutual coupling adversely. Therefore, a wise choice of dielectric constant as well as geometry of these pads is a necessity. A method (described in the **Appendix**) was also developed specifically to measure the dielectric constant of powders, liquids and suspensions used in HDC pads.

Using transmit coil arrays provides the ability to change amplitude and phase of each element which helps to achieve more homogenous RF magnetic field and also provides more control over the SAR. However, arrays introduce the challenge of maintaining mutual coupling within

acceptable levels. Coupling between elements in an array at high frequencies is quite sensitive to the presence of HDC liners. Therefore, in **chapter 3**, mutual impedance between elements in an eight channel array is investigated, and an appropriate method to mitigate coupling in the presence of an HDC liner is found. Results show that both real and imaginary parts of the mutual impedance can be removed using capacitive bridges with minimal degradation of the transmit performance.

The final aim of this thesis is to design a body array for 4.7 T. In **chapter 4** a transverse electromagnetic horn antenna is designed to image deep targets in the body. This element achieves better efficiency than dipoles that have been recently proposed as alternatives to traditional loop coils, especially for deep targets.

In all chapters of this thesis the theory is described and simulations are performed to assist with design and investigate the concepts. Structures are fabricated and tested on the bench before imaging using appropriate phantoms to verify the design and simulations.

Preface

This thesis is an original work by Atefeh Kordzadeh. The following chapters in this thesis have been published or submitted accordingly.

Chapter 2:

A. Kordzadeh, N. De Zanche, “Optimal-permittivity dielectric liners for a 4.7T MRI transceiver array”, submitted to Physics in Medicine and Biology.

Chapter 3:

A. Kordzadeh, N. De Zanche, "Control of Mutual Coupling in High-Field MRI Transmit Arrays in the Presence of High-Permittivity Liners," in IEEE Transactions on Microwave Theory and Techniques , doi: 10.1109/TMTT.2017.2668406

Appendix A:

A. Kordzadeh, N. De Zanche, "Permittivity Measurement of Liquids, Powders, and Suspensions Using a Parallel-Plate Cell", Concepts in Magnetic Resonance Part B: Magnetic Resonance Engineering, 46, 1; 19-24; 2016, DOI: 10.1002/cmr.b.21318.

Dedicated to my beloved Mother.

RIP

Acknowledgements

I am very fortunate to have a supporting family who encouraged me to follow my dreams by their limitless supports throughout my life. I would like to thank my father, Ahmad, and my mother, Motahhareh, for all the sacrifices that they had made, their love and encouragements. I owe my entire life to my precious mother whom I lost recently, you are in my heart forever. I would like to thank my sisters, Elham and Azadeh as my first teachers and role models.

I would like to express my sincere thanks and love to my husband, Daniel, without whom this accomplishment wasn't possible for me. He always stood by me and helped me to overcome difficulties.

I would like to extend my gratitude to my supervisors, Dr. Nicola De Zanche for his great mentorship and support during my PhD program. Moreover, I would like to thank my co-supervisor Dr. Abdulhakem Elezzabi for his trust and support to help me find my way in difficult moments. I also would like to acknowledge my committee members and examiners Dr. Alan Wilman, Dr. Atiyah Yahya, Dr. Roger Zemp and Dr. Scott King for reviewing my thesis thoroughly and for their insightful comments and encouragement.

Thank you to the support staff at the Peter S. Allen MR Research Centre. In particular, thanks to Mr. Peter Šereš for patiently helping me with running the 4.7 T console and Mr. Al-Karim Damji for very insightful conversions and comments. Thanks to Dr. Myrlene Gee for her fruitful advice and help with scanning.

I would like to thank my graduate colleagues specially Kelly McPhee for her advices, comments and supports.

Funding

I would like to acknowledge funding from the Natural Sciences and Engineering Research Council (NSERC) of Canada via my supervisor. Other awards including Faculty of Medicine and Dentistry 75th anniversary award and Queen Elizabeth II scholarships from the University of Alberta are also acknowledged.

Contents

Acknowledgements vi
Chapter 1 1
Introduction 1
1.1. Basics of NMR 1
1.1.1. NMR 1
1.1.2. Static magnetic field: B_0 3
1.1.3. Precession 3
1.1.4. RF excitation 4
1.1.5. Relaxation 6
1.1.6. Induced signal 8
1.1.7. NMR imaging 9
1.1.8. High fields: Pros and cons of high frequency 12
1.2. Radio frequency coils 13
1.2.1. Quality factor 14
1.2.2. Losses 15
1.2.3. SAR 16
1.2.4. Transmit efficiencies 16
1.2.5. Homogeneity of the RF field 17
1.2.6. RF penetration 18
1.2.7. Receive sensitivity 18
1.2.8. EM modeling 19
1.3. B_1 mapping 20
1.4. Electrical properties of tissues 20
1.5. Array configurations 21
1.5.1. Receive arrays 22
1.5.2. Transmit arrays 26
1.6. Motivation 30
1.7. Scope of This Thesis 31
Chapter 2 33
Optimal-permittivity Liners for a 4.7T Transceive Array 33

2.1. Introduction 33
2.2. Theory 34
2.3. Methods 37
2.3.1 Design 37
2.3.2 Simulation 39
2.3.3 Fabrication 45
2.3.4 Bench measurement 47
2.3.5 Scan 48
2.4. Discussion 50
2.5. Conclusion 51
Chapter 3 52
Control of Mutual Coupling in High-Field MRI Transmit Array in Presence of High Permittivity Liners 52
3.1. Introduction 52
3.1.1. Review of literature 53
3.1.2. Scope of this chapter 54
3.2. Theory 54
3.2.1. Mutual coupling 54
3.2.2. Mutual impedance in presence of dielectric liners 55
3.2.3. Capacitive decoupling 58
3.3. Methods 59
3.3. Design and simulation 59
3.4. Fabrication 64
3.5. Bench measurements 64
3.6. Scan 66
3.4. Discussion 68
3.5. Conclusion 69
Chapter 4 70
The TEM Horn: A New Array Element for High-field MRI 70
4.1. Introduction 70
4.2. Methods 72

4.2.1. Design 72
4.2.2. Simulation and Results 73
4.2.3. Array performance 82
4.3. Experiment 86
4.3.1. Fabrication 86
4.3.2. Bench Measurements 87
4.3.3. Scanner Measurements 89
4.4. Discussion 91
4.5. Conclusion 92
Chapter 5 93
Conclusion and Future Work 93
5.1. Conclusion 93
5.2. Future Directions 94
References 95
Appendix A 104
Permittivity Measurement of Liquids, Powders and Suspensions using a Parallel-Plate Cell 104
A.1. Introduction 104
A.2. Methods 105
A.2.1. Construction 105
A.2.2. Theory 106
A.2.3. Calibration and Measurement 106
A.2.4. Materials 108
A.2.5. Comparison to Coaxial Probes 109
A.3. Results and Discussion 109
A.4. Conclusions 116

List of Figures

Figure 1.1. (a) Spins in absence of the magnetic field, (b) spins in presence of magnetic field. 2
Figure 1.2. Bulk magnetization (M_0). 3
Figure 1.3. Precession of spins which sweeps a cone surface. 4
Figure 1.4.The effective magnetic field for exciting the spins. 6
Figure 1.5. Flip angle. 6
Figure 1.6. (a) Longitudinal and (b) transverse magnetization decay. 8
Figure 1.7. Transverse magnetization and FID signal 8
Figure 1.8. Gradient applied to B_0. 10
Figure 1.9. Sequence of gradients applied. 11
Figure 1.10. Loop wire coil. 14
Figure 1.11. *Q* of a resonant circuit. 15
Figure 1.12. RF wavelength compared to head model (Ansys Human body model) at high frequencies. 17
Figure 1.13. Ansoft human body model (male) with 2mm resolution and tetrahedral mesh. 21
Figure 1.14. Parallel imaging (SENSE) of head using a two element array of coils each contributing to generate a reduced FOV image shown in right. 24
Figure 1.15. *k*-space trajectory of a fast k_z 3D RF pulse [48]. 29
Figure 1.16 Inhomogeneity in B_1^+ field resulting in dark and bright areas at 4.7T. 30
Figure 2.1. Designed head coil array. 36
Figure 2.2. Different dielectric layers and boundaries. 39
Figure 2.3. Simulation of the structure in HFSS. 40
Figure 2.4. Comparison of the scattering (*S*) matrix (8-channel) [-60dB 0] (dB) at 200 MHz after matching for different dielectric liners (ε_r=1 (a), ε_r=17.5 (b), ε_r = 35 (c), ε_r=78 (d), and ε_r=150 (e), respectively) in the presence of an ideal matching network at each port (S_{ii}=0) 41
Figure 2.5. B_1^+ field over a transverse slice in the middle of the phantom with different liner permittivities (a) ε_r=1 (air), (b) ε_r=17.5, (c) ε_r=78, (d) ε_r=150. 42
Figure 2.6. B_1^+ in a transverse slice in middle of the phantom and a sagittal slice with different liner permittivities: ε_r=1 (a, f), ε_r=17.5 (b, g), ε_r=35 (c, h), ε_r=78 (d, i), and ε_r=150 (e, j). Note the longitudinal asymmetry resulting from high-permittivity liners. 43

Figure 2.7. Local SAR in a transverse slice in middle of the phantom and a sagittal slice with different liner permittivities: ε_r=1 (a, f), ε_r=17.5 (b, g), ε_r=35 (c, h), ε_r=78 (d, i), and ε_r=150 (e, j). Note the longitudinal asymmetry resulting from high-permittivity liners. 44
Figure 2.8. Fabricated dielectric pads: (a) high dielectric constant pad (ε_r=150), (b) water pad, (c) matching pad (ε_r=17.5). 46
Figure 2.9. Fabricated array with dielectric liner and phantom. 47
Figure 2.10. Bench measurement set-up. 48
Figure 2.11. S_{11} (a) measured on the bench, and (b) simulation for each case. 49
Figure 2.12. Coil array set-up for imaging 49
Figure 2.13. Comparison of simulated fields (top row) from a single element and fields measured using the double-angle method (bottom row). Liner permittivities: ε_r = 1 (a, e), ε_r = 17.5 (b, f), ε_r = 78 (c, g) and ε_r = 150 (d, h). 50
Figure 3.1. Two loops in presence of dielectric liner and phantom. 55
Figure 3.2. (a) Mutual resistance, (b) mutual reactance between two loops in presence of high permittivity liner and phantom. 57
Figure 3.3. Capacitive decoupling for two element array. 58
Figure 3.4. Designed 8 channel array in presence of liner and phantom. 59
Figure 3.5. Capacitor arrangement for each element. 60
Figure 3.6. B_1^+ field versus radius plotted in transverse plane in the phantom for coupled coil in presence and without HDC liner. 61
Figure 3.7. *S* matrix magnitude (dB) with liner present for (a) coupled, (b) R_{12}=0, (c) X_{12}=0, (d) Z_{12}=0, and (e) coupled without liner. 63
Figure 3.8. Simulated B_1^+ field pattern for (a) coupled, (b) R_{12}=0, (c) X_{12}=0, (d) Z_{12}=0. SAR field pattern for (e) coupled, (f) R_{12}=0, (g) X_{12}=0, (h) Z_{12}=0, each channel is excited with 1 A current excitation. 64
Figure 3.9. Fabricated arrays (a) coupled (b) decoupled. Decoupling bridges are highlighted by ellipses. 65
Figure 3.10. Experiment set-up including coil array, VNA and phantom. 65
Figure 3.11. Measured (a) $|S_{11}|$ and (b) $|S_{12}|$ (in dB) comparison for coupled and decoupled case with the HDC liner. 66

Figure 3.12. Coil array set-up for imaging (red and blue connections represent the set-up used for each subset of measurements). 67
Figure 3.13. Simulated B_1^+ field (0-2μT) for (a) coupled, (b) decoupled and SAR (0-1W/kg) for (c) coupled and (d) decoupled coil when one channel is excited, and measured flip angle (0-50º) or B_1^+ maps for (e) coupled, (f) decoupled coil. 68
Figure 4.1: Designed TEM horn antenna. 73
Figure 4.2. Simulation set-up.....74
Figure 4.3. S_{11} of the designed TEM horn antenna. 74
Figure 4.4. Horn antenna B_1^+ plot on (a) coronal at depth of 5 cm, (b) coronal slice at depth of 10 cm, central slice (c) sagittal and (d) transverse slice [0 1 μT]. 75
Figure 4.5. SAR plot on (a) coronal slice at depth of 5 cm, (b) coronal slice at depth of 10 cm, central slice (c) sagittal and (d) transverse slice [0 0.5W/kg]. 76
Figure 4.6. Designed dipole antenna (a) and bow tie antenna (b). 77
Figure 4.7. Dipole antenna B_1^+ field plotted on (a) coronal slice at depth of 5 cm, (b) coronal slice at depth of 10 cm, central slice (c) sagittal and (d) transverse slice [0 1μT]. 78
Figure 4.8. Dipole antenna SAR plotted on (a) coronal slice at depth of 5 cm, (b) coronal slice at depth of 10 cm, central slice (c) sagittal and (d) transverse slice [0–0.5 W/kg]. 79
Figure 4.9. B_1^+ plots on *y*-*z* plane for horn (left) and dipole (right).....79
Figure 4.10. B_1^+ field compared for horn antenna versus dipole in coronal slice at 10 cm depth. 80
Figure 4.11. B_1^+ field compared for horn and dipole antenna for different depths. 81
Figure 4.12. Two elements array of (a) horn and (b) dipole. 82
Figure 4.13. S_{12} of a two-element array of horn antennas compared to a two-element array of dipole antennas spaced according to Fig. 4.12b and so their centres are spaced the same as the horns in Fig. 4.12a.....83
Figure 4.14. Three-element array of horn antennas. 84
Figure 4.15. (a) S_{11} and (b) coupling level for the three element array. 85
Figure 4.16. B_1^+ field in the transverse plane (a) 2-D and (b) 3-D for three elements excited with phases (90º-0º-180º).....85
Figure 4.17. Fabricated horn antenna and phantom. 86
Figure 4.18. Measured S_{11} of the antenna in presence of phantom. 87

Figure 4.19. Bench measuremenet for (a) two element array and (b) three element array of horn antennas. 88
Figure 4.20. Measured coupling for (a) two element (b) three element horn array. 89
Figure 4.21. Flip angle maps [0 50̊] on (a) *x-z*, (b) *x-y* and (c) *z-y* planes and simulated B_1^+ for single element on (d) *x-z*, (e) *x-y* and (f) *z-y* planes. 91
Figure 4.22. Images acquired using single element horn on (a) *x-z*, (b) *x-y* and (c) *z-y*. 91
Figure 4.23. (a) Flip angle maps [0 50̊] on *x-y* and (b) and simulated B_1^+ for a three element array when one element is excited on *x-y* plane. 91

List of Tables

Table 1.1. Electrical properties some human tissues. 21
Table 2.1. Design parameters for the coil array. 38
Table 2.2. Transmit performance parameters of the coil array in presence of the different dielectric liners at 200 MHz (HFSS simulation, 1A quadrature excitation). 43
Table 2.3. Summary of results comparing fields and efficiencies for the case where no air-gap is present versus adding air-gap between phantom and liner. 45
Table 2.4. The required transmit gain to achieve a given flip angle. 50
Table 3.1. Designed dimensions of the structure. 60
Table 3.2. Designed values for tuning and decoupling capacitors as well as their locations. 61
Table 3.3. Summary of simulation results. 62
Table 4.1. Dimensions of the designed TEM horn. 73
Table 4.2. Design parameters of the dipole and bowtie antennas. 77
Table 4.3. Quantitative comparison between fields and efficiencies of dipole, bow-tie and horn antenna. 81

List of Acronyms

2D two dimensional

3D three dimensional

BOLD blood oxygen level dependent

COV coefficient of variation

DAM double angle method

EM electromagnetic

EMF electromotive force

FCC Federal Communication Commission

FDTD finite difference time domain

FEM finite element method

fMRI functional magnetic resonance imaging

GRAPPA generalized auto calibrating partially parallel imaging

HDC high dielectric constant

HFSS high frequency structure simulator

IEC International Electrotechnical Commission

MOM method of moments

MRI magnetic resonance imaging

MUT material under test

NMR nuclear magnetic resonance

RF radio frequency

ROI region of interest

R_x receive

SAR specific absorption rate

SENSE sensitivity encoding

SMASH simultaneous acquisition of spatial harmonics

SNR signal to noise ratio

TEM transverse electromagnetic

T_x transmit

VNA vector network analyzer

VOI volume of interest

Chapter 1

Introduction

1.1. Basics of NMR

1.1.1. NMR

Nuclear Magnetic Resonance (NMR) was first observed by Bloch and Purcell in 1946 [1], [2]. Not only used in chemistry for analysis of the chemical structures, it has been developed to image the human body [3], [4]. Today as a clinical imaging modality, magnetic resonance imaging (MRI) is widely used to image human anatomy as well as functional aspects such as brain activity [5], [6].

NMR comes from the interaction between the intrinsic spin angular momentum of nuclei (known as spin) and an external magnetic field. Spin can take integral values from 1/2 to 9/2. If the nuclei contain odd number of protons and/or neutrons the nuclei will have a magnetic moment, μ. For even number of protons and even number of neutrons, the value of I associated to the nuclei will be zero. To be NMR viable, a nucleus should contain magnetic moment, μ. For each nuclear species, spin angular momentum is related to the nuclear magnetic moment with a constant called magnetogyric ratio, γ.

$$\mu = \gamma I \hbar \tag{1.1}$$

where $\hbar = h/2\pi$ (h is plank's constant=6.63×10^{-34} J s).

In the absence of any external magnetic field, spins are randomly oriented. If an external static magnetic field, $\boldsymbol{B}_0$, is applied, spins orient in parallel and antiparallel to the applied field (**Figure 1.1**). According to the Zeeman effect, there is an energy difference (ΔE) between spins in these two states given by

$$\Delta E = \gamma \hbar \boldsymbol{B}_0. \tag{1.2}$$

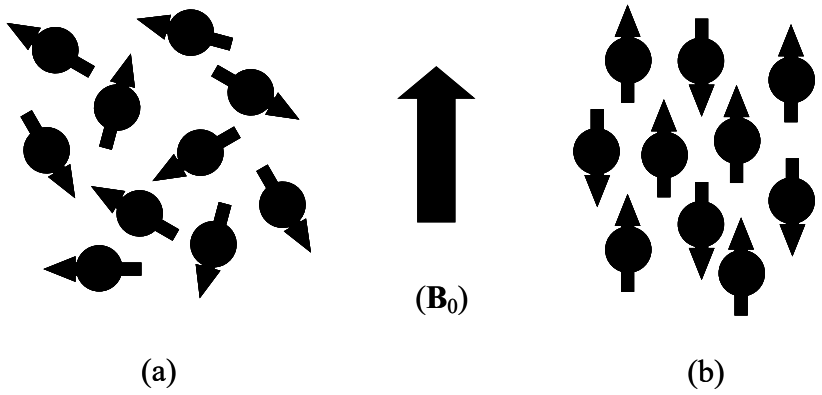

Figure 1.1. (a) Spins in absence of the magnetic field, (b) spins in presence of magnetic field.

As spins aligned with magnetic field are in lower energy level compared to antiparallel spins, more spins tend to be parallel to $\mathbf{B}_0$. Using the Boltzmann relationship, the difference in population of the spins in these two states is given by

$$\frac{N_\uparrow}{N_\downarrow} = \exp(\frac{\Delta E}{k_B T_s}), \tag{1.3}$$

where $N_\uparrow$ and $N_\downarrow$ are the number of parallel and antiparallel spins respectively, ΔE is the energy difference between them, T_s is the temperature (kelvin) and k_B is the Boltzman constant (1.38×10^{-23} JK^{-1}). As the energy difference between spins is small, (1.3) can be approximated by (1.4).

$$\frac{N_\uparrow}{N_\downarrow} \approx 1 + (\frac{\Delta E}{k_B T_s}) \tag{1.4}$$

Therefore, the difference in the spin population will be given by (1.5) where N_s is the total number of spins in the sample.

$$N_\uparrow - N_\downarrow \approx N_s(\frac{\gamma \hbar \boldsymbol{B}_0}{2k_B T_s}) \tag{1.5}$$

The population difference depends on the $\boldsymbol{B}_0$ showing that for higher magnetic fields, the spin difference will be higher.

The most abundant magnetic nuclei in living tissues is ^{1}H (proton) making it the best candidate for MRI.

1.1.2. Static magnetic field: B_0

Static magnetic field, $\mathbf{B}_0$, is a strong magnetic field along z-axis (as shown in **Figure 1.2**). When $\mathbf{B}_0$ is applied to the spins in thermal equilibrium, the net transverse magnetization is zero due to randomly distributed transverse magnetization. Therefore, bulk magnetization of the sample would be in the *z* direction and is found using (1.6).

$$\boldsymbol{M}_0 = \sum_{n=1}^{N_s} \mu_z = \frac{\gamma^2 \hbar^2 \boldsymbol{B}_0 N_s}{4 k_B T_s} \tag{1.6}$$

(1.6) states that for a given sample, the magnetization depends on the sample temperature and the magnetic field strength. As sample temperature can not be changed, the magnetization is mainly determined by $\mathbf{B}_0$. Hence increasing the static field strength will increase magnetization which consequently increases the NMR signal.

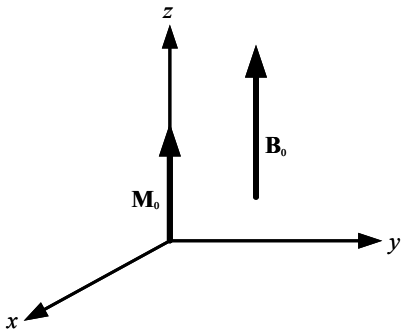

Figure 1.2. Bulk magnetization ($\mathbf{M}_0$).

1.1.3. Precession

The magnetic moment of the nuclei is oriented at an angle to the main magnetic field as shown in **Figure 1.3**. Therefore, the magnetic field exerts a torque to the magnetic moment given by $\mu \times \boldsymbol{B}_0$. The generated torque results in oscillating magnetic moment around $\mathbf{B}_0$ which is called

precession. The frequency of precession is related to the Zeeman energy of (1.2) using Planck's law:

$$E = \hbar\omega_0. \tag{1.7}$$

Simplifying, the nuclear precession frequency which is called Larmor frequency, is given by

$$\omega_0 = \gamma \boldsymbol{B}_0 \tag{1.8}$$

For field strength of 4.7 T, the Larmor frequency of proton is 200.1072MHz (γ=42.577 $MHzT^{-1}$ for proton).

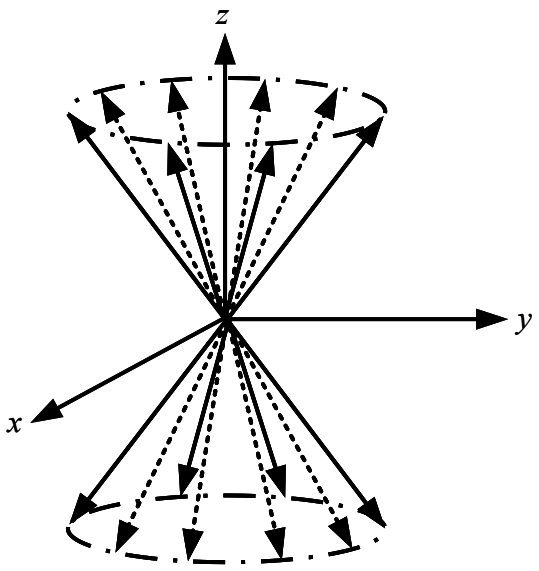

Figure 1.3. Precession of spins which sweeps a cone surface.

1.1.4. RF excitation

To excite the spin system, the net equilibrium magnetization should be deflected from its orientation along $\mathbf{B}_0$. To do that, a second magnetic field, called $\mathbf{B}_1$, is needed to exert a torque to the magnetization. This field is a time varying magnetic field perpendicular to $\mathbf{B}_0$ (in the transverse plane) and it should be synchronized to the Larmor frequency of the nuclei as shown

in **Figure 1.4**. It can be shown that the sample magnetization precesses around the total field applied to it which is $\mathbf{B_0} + \omega/\gamma$[1].

In the laboratory frame, $\mathbf{B}_1$ field can be decomposed into two counter rotating components, $\mathbf{B}_1^+$ and $\mathbf{B}_1^-$.

$$\boldsymbol{B}_1(t) = \boldsymbol{B}_1^+(t) + \boldsymbol{B}_1^-(t) \tag{1.9}$$

$$\boldsymbol{B}_1^+(t) = B_1(t)\{\cos(\omega_1 t)\,\hat{x} + \sin(\omega_1 t)\,\hat{y}\} \tag{1.10}$$

$$\boldsymbol{B}_1^-(t) = B_1(t)\{\cos(\omega_1 t)\,\hat{x} - \sin(\omega_1 t)\,\hat{y}\} \tag{1.11}$$

In a frame of reference rotating at the Larmor frequency the $\mathbf{B}_1^+$ field appears stationary.

Using (1.10) it is inferred that $\mathbf{B}_1^+$ component is rotating with the same direction as the spins, therefore this component is used to excite the spins. Conversely, $\mathbf{B}_1^-$ component rotates in the negative sense compared to the precession [7].

$$\boldsymbol{B}_1^+ = \frac{\boldsymbol{B}_{1x} + j\boldsymbol{B}_{1y}}{2} \tag{1.12}$$

$$\boldsymbol{B}_1^- = \frac{(\boldsymbol{B}_{1x} - j\boldsymbol{B}_{1y})^*}{2} \tag{1.13}$$

Because of exciting the spins with the $\mathbf{B}_1$ field, the magnetization is perturbed from its orientation along $\mathbf{B}_0$ as shown in **Figure 1.4**. The angular displacement of the magnetization measured compared to z axis is called the flip angle, α which is shown in **Figure 1.5**. For a $\mathbf{B}_1$ pulse (i.e., an RF pulse) of duration τ, the flip angle is given by

$$\alpha = \int_0^\tau \gamma \boldsymbol{B}_1(t)dt. \tag{1.14}$$

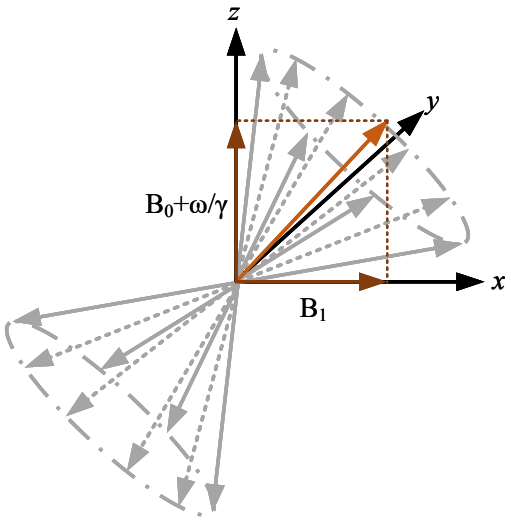

Figure 1.4.The effective magnetic field for exciting the spins.

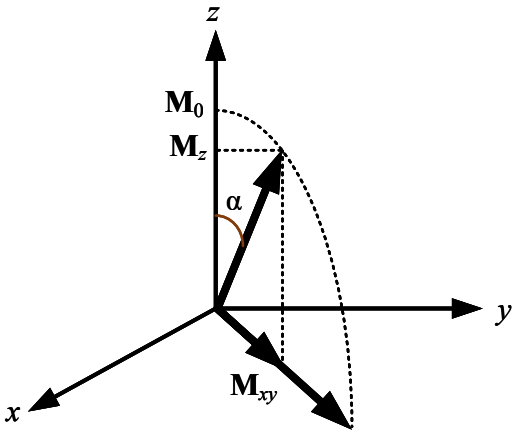

Figure 1.5. Flip angle.

1.1.5. Relaxation

Once the excitation is removed, the spins return to thermal equilibrium through the process of relaxation. There are two types of relaxation: spin-lattice (or longitudinal) and spin-spin (or transverse relaxation). The longitudinal magnetization ($\mathbf{M}_z$) recovers by releasing energy through interactions between spins and the lattice. This recovery rate is characterized by a time constant called T_1.

$$\frac{d\boldsymbol{M}_z(t)}{dt} = \frac{[\boldsymbol{M}_z(t) - \boldsymbol{M}_0]}{T_1} \tag{1.15}$$

(1.15) describes the recovery of $\mathbf{M}_z$ over time, where $\mathbf{M}_0$ is the longitudinal magnetization at equilibrium.

On the other hand, relaxation of transverse magnetization is due to interactions between spins at macroscopic level leading $\mathbf{M}_{xy}$ to zero.

$$\frac{d\boldsymbol{M}_{xy}}{dt} = -\frac{\boldsymbol{M}_{xy}}{T_2} \tag{1.16}$$

T_2 is called the transverse relaxation constant. In practice, imperfections in static field such as inhomogeneities will result in small shift in resonant frequency therefore can lead to dephasing and thus faster transverse magnetization decay. Therefore, transverse magnetization decay is happening with an accelerated rate called T_2^* defined by

$$\frac{1}{T_2^*} = \frac{1}{T_2} + \frac{1}{T_2'} \tag{1.17}$$

where T_2 is spin-spin relaxation due to interactions between nuclei in molecules, and T_2' is due to inhomogeneities in static magnetic field. As can be seen in equation (1.17), T_2^* combines both effects.

Including longitudinal and transverse relaxation in the Bloch equations, the evolution of sample magnetization over time can be written as (1.18).

$$\frac{d\boldsymbol{M}}{dt} = \gamma \boldsymbol{M} \times \boldsymbol{B} - \frac{\boldsymbol{M}_x\hat{x} + \boldsymbol{M}_y\hat{y}}{T_2} - \frac{(\boldsymbol{M}_z - \boldsymbol{M}_z^0)\hat{z}}{T_1} \tag{1.18}$$

Figure 1.6 shows longitudinal and transverse magnetization decay.

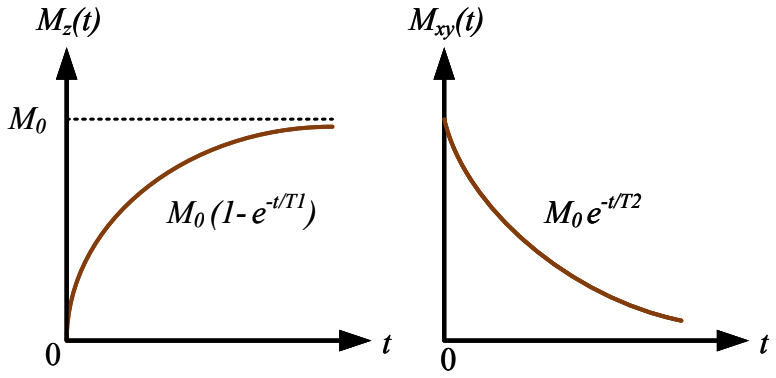

Figure 1.6. (a) Longitudinal and (b) transverse magnetization decay.

1.1.6. Induced signal

The transverse magnetization, $\mathbf{M}_{xy}$, is rotating with Larmor frequency. As $\mathbf{M}_{xy}$ is a time varying magnetization, if a radio frequency coil is placed in the transverse plane, there will be an electromotive force induced in that coil (see **Radio frequency coils** section). This is the time domain NMR signal that is received and it is an exponentially decaying signal as shown in Figure 1.7.

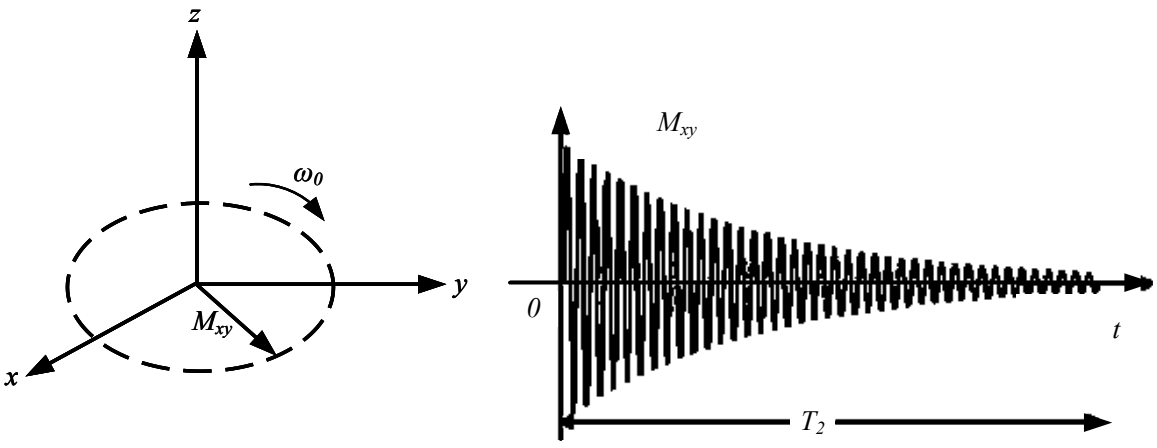

Figure 1.7. Transverse magnetization and FID signal.

1.1.7. NMR imaging

1.1.7.1. Contrast

Contrast is the ability of an imaging modality to differentiate tissues. There are many different contrast mechanisms measurable with NMR. The main ones are proton density, diffusion weighted, T_1-weigthted and T_2- weighted images. As most soft tissues have similar proton density, contrast based on spin density is not usually great. It is found that relaxation times are different in normal and abnormal tissues [8]. This makes relaxation difference the main contrast mechanism used in clinical diagnosis.

To measure differences in relaxation rates, a sequence of pulses is typically used. There are two timing parameters used in imaging sequences called repetition time and echo time. Generally repetition time (T_R) is the time between successive excitation RF pulses for a particular slice. Echo time (T_E) is the time between applying the RF pulse and the peak of echo as sown in **Figure 1.9**. Controlling these two parameters in an imaging sequence will determine the imaging contrast peformance.

Choosing short T_R (comparable to T_1) and short T_E, facilitates acquiring T_1 weighted images as $\mathbf{M}_0$ does not have enough time to fully recover. On the other hand, chosing long T_R and T_E will lead to T_2 weighted images as spins have more time to dephase and $\mathbf{M}_0$ fully relaxes.

1.1.7.2. Signal localization

To generate an image using NMR, spatial information must be encoded into the signal. All spins resonate at the same frequency, ω_0, in presence of the uniform static magnetic field. Therefore, by applying a spatially varying magnetic field to $\mathbf{B}_0$, e.g., a linear gradient, the resonant frequency of the spins will be dependent on the location.

1.1.7.2.1. Slice selection

The first step in signal localization is to select a slice, e.g., in the direction of the main magnetic field, z. This slice is excited selectively using a linear gradient field in the direction normal to the slice as shown in **Figure 1.8**.

$$\omega(z) = \gamma(\boldsymbol{B}_0 + \boldsymbol{G}_z z) \tag{1.19}$$

As can be seen slice thickness is determined by the RF pulse bandwidth and the slice location is determined by the center frequency of the applied RF pulse.

$$BW_{RF} = \gamma \boldsymbol{G}_z \Delta z \tag{1.20}$$

$$\omega_{center} = \gamma(\boldsymbol{B}_0 + \boldsymbol{G}_z z_0) \tag{1.21}$$

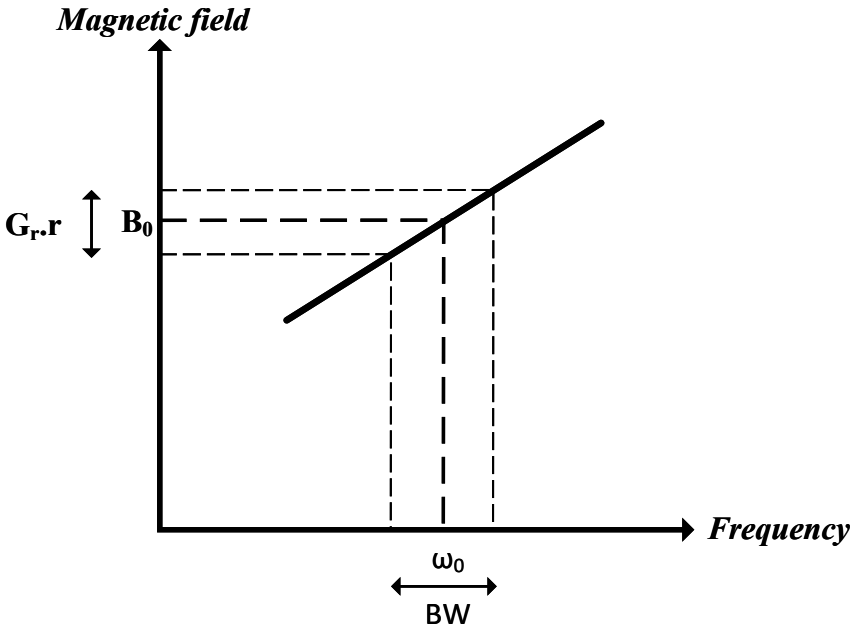

Figure 1.8. Gradient applied to $\mathbf{B}_0$.

1.1.7.2.2. Phase encoding

Phase encoding gradient is used to encode position for the orthogonal direction to frequency encode one. This is done by inducing a phase to the signal before doing the acquisition period. The accumulated phase during a gradient with duration τ and strength $\boldsymbol{G}_y$ is given by (1.22).

$$\emptyset(y) = \gamma \boldsymbol{G}_y y \tau \tag{1.22}$$

By repeated application of phase encode gradients before frequency encode gradient as shown in **Figure 1.9**, information is encoded in the phase of the signal. The strength of phase encode gradient is changing before each acquisition.

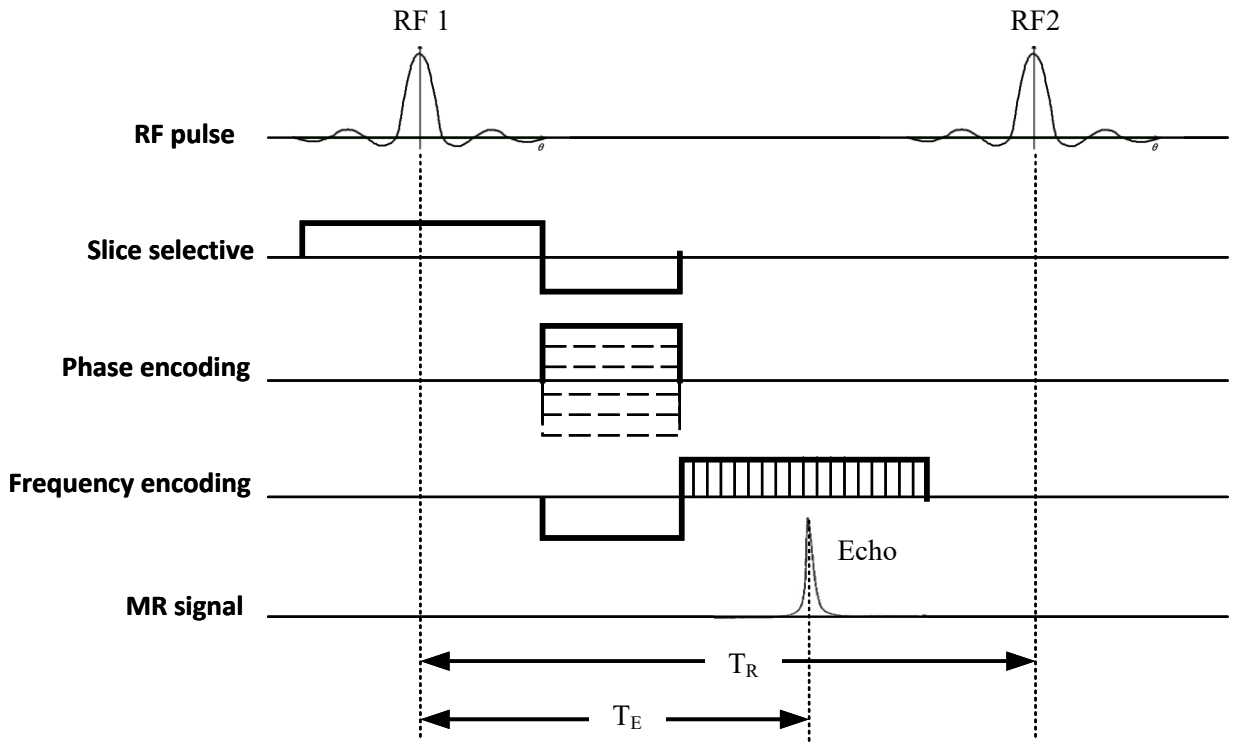

Figure 1.9. Sequence of gradients applied.

1.1.7.2.3. Frequency encoding

Once the slice is selected along z, a gradient field is now applied in one of the transverse directions to encode location into frequency. This gradient is called frequency encoding gradient and is applied during image readout (data acquisition). The received signal after applying frequency encode gradient will be

$$s(t) = \int \boldsymbol{M}_{xy}(x) e^{-j(\omega_0 + \gamma \boldsymbol{G}_x x)t} dx \tag{1.23}$$

The term including ω_0 can be removed in the rotating frame. Then the time domain signal has the form of a Fourier transformation of $\mathbf{M}_{xy}$. We can use inverse Fourier transform to find $\mathbf{M}_{xy}$ from the observed signal.

$$\boldsymbol{M}_{xy}(x) = \gamma \boldsymbol{G}_x \int S(t) e^{j\gamma \boldsymbol{G}_x x t} dt \tag{1.24}$$

This gradient is assumed to be constant over the duration of the readout.

1.1.7.3. *k*-space

Data acquired during successive readouts fills the spatial frequency space (*k*-space) which is then Fourier transformed to recover the image. As mentioned in the previous sections, the acquired data phase is given by (1.25).

$$\emptyset(r) = \int \omega(r) dt = r\gamma \int \boldsymbol{G} dt = rk \tag{1.25}$$

In which *r* is the spatial component (assumed constant in time) and *k* is the new defined variable for *k*-space. Therefore, *k* in units of *radian/m* can be written as

$$k = \gamma \int \boldsymbol{G} dt \tag{1.26}$$

During image readout *k* is swept in the *k*-space in different trajectories to fill the *k*-space. Fourier transformation of *k*-space will yield the image.

1.1.8. High fields: Pros and cons of high frequency

There is an ever-increasing tendency to go to higher field strength MRI [9]. This is mainly due to increase in SNR with increasing the magnetic field strength. It also benefits the recent parallel imaging techniques in which SNR is traded off for imaging speed [10]. Moreover functional MRI (fMRI) [11], spectroscopy [12] and other nuclei imaging (such as sodium imaging) [13] which have intrinsically low SNR will benefit from high field strengths.

By increasing field strength, T_1 gets longer which can be useful for suppressing the background signal, e.g., in MR angiography [10], [14]. On the other hand, the trend for T_2 is more

complicated. However it is shown that T_2 as well as T_2^* decrease with increasing field strength [14], [15]. Applications which are based on susceptibility difference will noticeably benefit from high field due to increased contrast. BOLD-contrast (blood-oxygen-level dependent) used in functional MRI is an example [16].

Other than the above-mentioned advantages, there are several challenges associated with high field imaging, such as acoustic noise because of fast gradient switching. The first RF issue is Joule heating of tissue due to RF excitation fields (see **SAR** section below), which generally increases with field strength [10]. This poses challenges in maintaining RF safety at high fields. Moreover, as field strength is increasing, the Larmor frequency increases as well leading to short wavelength. As will be discussed in the **Homogeneity of the RF field** section, there will be inhomogeneous fields generated in the region of interest. The inhomogeneity causes non-uniform excitation of the spins with consequent bright and dark areas in the resulting images. There will also be areas with significant electric fields leading to SAR hot spots.

Moreover, there are significant technical challenges associated with RF coil design at higher frequencies that need to be addressed.

1.2. Radio frequency coils

A radio frequency coil is responsible for producing the excitation fields and for receiving the NMR signal. In the transmit mode (see **RF excitation**) it is responsible for generating the time varying $\mathbf{B}_1^+$ field. When a time varying current source excites an RF probe, its currents will generate a time varying magnetic field.

During reception, the time-varying transverse magnetic field generated inside the sample will induce an electromotive force on the coil which is the detectable signal. This is described by Faraday law of induction:

$$EMF = \oint_C \boldsymbol{E}.dl = -\frac{d}{dt}\iint_S \boldsymbol{B}.dS. \tag{1.27}$$

An RF coil in its simplest form is a loop of wire, as shown in **Figure 1.10**, which is equivalent to an inductor L and N capacitors having capacitance C/N are placed along its length. These capacitors are usually placed uniformly around the coil perimeter to ensure that current is

uniformly distributed over the coil and the electric fields generated by the loop is minimized (typically this requires the conductive segments to be at most $\lambda/20$ in length [17]). This LC circuit will resonate at an angular frequency given by $(LC)^{-1/2}$. At this frequency, the circuit is able to transfer electric/magnetic field efficiently to and from the environment around it. The RF coil's resonance frequency should therefore be tuned to the Larmor frequency of the nuclei of interest.

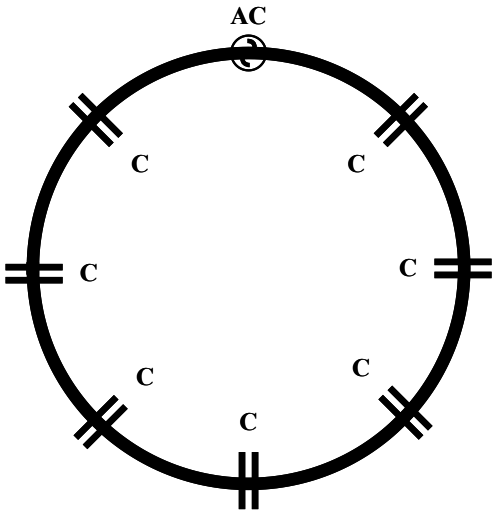

Figure 1.10. Loop wire coil.

1.2.1. Quality factor

Q factor is an important feature for resonant circuits that determines how efficiently that circuit stores energy.

$$Q = 2\pi \frac{Energy\ stored}{Energy\ dissipated\ per\ cycle} \tag{1.28}$$

One can measure Q as the ratio of the resonant frequency over -3dB bandwidth, Δf as shown in **Figure 1.11**.

$$Q = \frac{f_0}{BW} \tag{1.29}$$

When the coil is in proximity of a lossy medium such as human tissue, the amount of power lost will increase therefore the Q of the RF coil is reduced. This reduction in Q indicates the how well the coil and the load are coupled. Q in the presence of the load is called loaded Q_{loaded}.

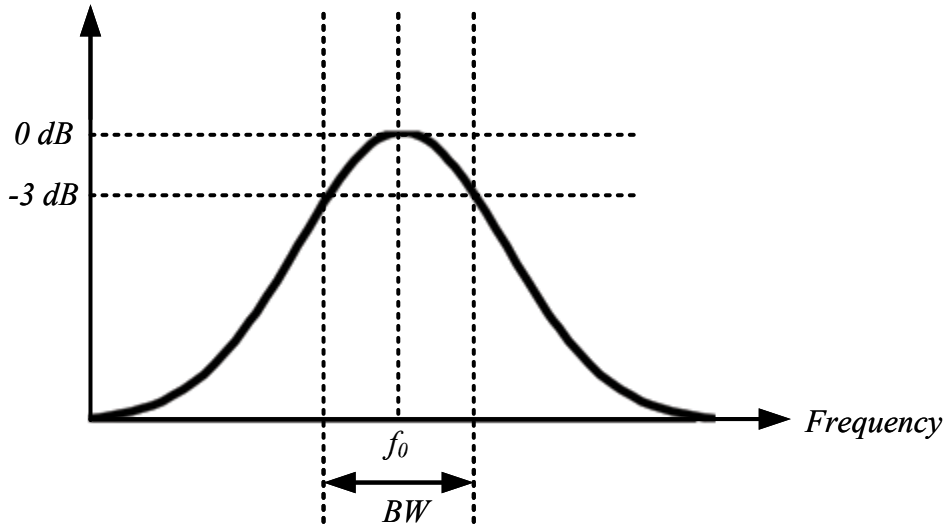

Figure 1.11. Q of a resonant circuit.

1.2.2. Losses

RF Losses are due to power lost inside the phantom, in the RF coil and as a result of radiation. Power lost in the conductive areas (phantom and on conductive RF coil) is due to conductivity, σ, and is found using equation below [18].

$$P = 0.5 \iiint_V \sigma |\boldsymbol{E}|^2 dV \tag{1.30}$$

The resistance of a conductor as well as the load and radiation resistances are frequency dependent (as $\sqrt{\omega}, \omega^2, \omega^4$ respectively). As we move to higher frequencies, these resistances can change dramatically, and at high enough frequencies the radiation loss will dominate [18].

1.2.3. SAR

Specific absorption rate (SAR) is a parameter defined to assess the safety of RF coils. As stated by Faraday's law, time varying magnetic field will generate electric field. Due to conductivity of the tissues, the induced currents result in Joule heating. SAR is defined as the amount of power absorbed in the tissue divided by the mass of the sample [18].

$$SAR = \frac{RF\ power\ absorbed\ in\ sample}{weight\ of\ sample} \tag{1.31}$$

Often, SAR is averaged over the whole body, or 1 or 10 grams of tissue to obtain a local measurement. As the electric fields within a phantom or body, cannot be measured with an MRI scanner, the local distribution of SAR is usually found using electromagnetic simulations. SAR is calculated using the simulated electric fields, conductivity (σ) and mass density of the material (ρ).

$$SAR = \frac{\sigma}{2\rho}|\boldsymbol{E}|^2 \tag{1.32}$$

The International Electrotechnical Commision (IEC) has set safe limits for SAR in different parts of the body [19]. In the normal operating mode, SAR is limited to 10 W/kg for any 10grams of tissue, 4 W/kg over whole body and 3.2 W/kg over the head. These limits are averaged for a 6-minute period. Peak SAR should not exceed twice the aforementioned values over a 10 second period [19].

The clinical scanners can monitor 10s and 6 min averages of total power and therefore average SAR based on the available data and estimated RF power [20]. To account for high local SAR, the 10g peak to average SAR ratio from simulations is used as a safety factor to set the trip thresholds.

1.2.4. Transmit efficiencies

In order to assess the efficiency of an RF coil in the transmit mode, array transmit parameters are defined [21]. Transmit efficiency, E_v, is defined as the ability of RF coil to generate $\mathbf{B}_1^+$ field at a

point in the volume of interest (VOI) over the power that is absorbed over the whole sensitive volume of the coil, P_V.

$$E_{V\_B} = \frac{|\boldsymbol{B}_1^+|}{\sqrt{P_V}} \tag{1.33}$$

Safety excitation efficiency is the considered for both peak SAR over 10gram of tissue and and average SAR over the VOI and are defined as (1.34) [21].

$$E_{V\_SAR} = \frac{|\boldsymbol{B}_1^+|}{\sqrt{SAR}} \tag{1.34}$$

1.2.5. Homogeneity of the RF field

RF wavelength is linearly dependent on the main magnetic field strength, $\mathbf{B}_0$, according to (1.35). Consequently, as $\mathbf{B}_0$ increases, wavelength decreases and becomes more comparable to the size of the imaging target. Moreover, the wavelength is further reduced inside dielectric media due to the permittivity of the medium according to

$$\lambda_r = \frac{\lambda}{\sqrt{\varepsilon_r}}. \tag{1.35}$$

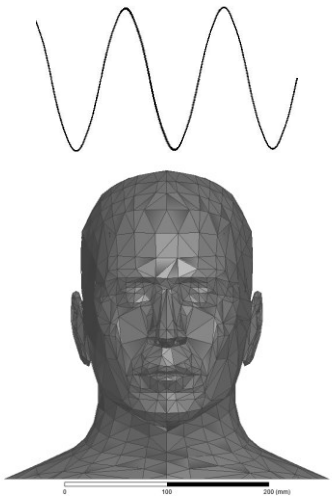

Figure 1.12. RF wavelength compared to head model (Ansys Human body model) at high frequencies.

For example, at 4.7 T used in this thesis, the RF wavelength inside brain with a typical $\varepsilon_r = 56$ (https://www.fcc.gov/general/body-tissue-dielectric-parameters) at 200 MHz, is 20 cm. This is comparable to the size of an adult head (**Figure 1.12**). When the object being imaged is comparable or smaller than the wavelength, there will be destructive and constructive interferences of the RF field, and therefore in the image dark and bright regions will appear which degrade the diagnostic quality of the image. It is important to have homogeneous fields in transmit because many sequences perform best with uniform excitation of the spins [22].

1.2.6. RF penetration

The RF penetration, or skin, depth, δ, is the parameter that defines how much electromagnetic fields can penetrate a lossy medium and for a transverse electromagnetic (TEM) field it is given by [23]

$$\delta = \frac{1}{\alpha} = \frac{1}{\omega\sqrt{\mu\varepsilon}\left(0.5\left[\sqrt{1+(\sigma/\omega\varepsilon)^2}-1\right]\right)^{1/2}}. \tag{1.36}$$

At this depth, the amplitude of uniform plane waves impinging on an infinite half plane of material decay by 1/e. RF penetration depends on the frequency (ω) as well as the permeability of the medium (μ_0=4π×10^{-7}), and conductivity of the tissue (σ) [23], [24]. Working at high frequencies is challenging due to reduced penetration depth of the RF fields. Hence imaging deep targets will be challenging.

1.2.7. Receive sensitivity

The EMF induced in the RF coil is as a result of precessing magnetization in the transverse plane. The receive sensitivity of the RF coil created at the sample, $\mathbf{B}_1^-$, contributes to the detected signal strength according to [7]

$$EMF = \frac{\partial}{\partial t}\int_{sample} \boldsymbol{B}_1^-.\boldsymbol{M}\, dV = V_s \boldsymbol{B}_{1tr}^- \boldsymbol{M}_T \omega_0. \tag{1.37}$$

Here ω_0 is the Larmor frequency, $\boldsymbol{B}_{1tr}^-$ is the transverse counter-rotating circularly polarized component of RF magnetic field, $\mathbf{M}_T$ is the transverse magnetization and V_s is the sample

volume. The second equality is valid in the case of an ideal uniform sensitivity and magnetization. As the sample magnetization is proportional to the main static field, $\mathbf{B}_0$, and Larmor frequency is also linearly related to $\mathbf{B}_0$, $\omega_0 = -\gamma \boldsymbol{B}_0$, the detectable signal is proportional to the square of the static magnetic field. Conversely, noise in the detected signal is mostly thermal (Johnson-Nyquist) noise and can be found using **(1.38)**.

$$N = \sqrt{4k_B T R \Delta f} \tag{1.38}$$

Consequently, the signal-to-noise ratio is

$$SNR = \frac{\sqrt{2}\omega_0 \Delta V \boldsymbol{M}_0 |\boldsymbol{B}_t|}{\sqrt{4k_B T \Delta f R}}. \tag{1.39}$$

Here k_B is the Boltzmann's constant, T is the absolute temperature, R is the resistance of the coil and Δf is the RF bandwidth. As discussed in (**Losses** section) the resistance of the conductor and sample are dependent on frequency ($\sqrt{\omega}, \omega^2$ respectively) hence noise is accordingly related to frequency. If there is no or small load, the dominant noise will be due to coil conductors and $SNR \propto \omega_0^{7/4}$. If the coil is heavily loaded then load resistance will dominate and SNR will be linearly dependent on the frequency, $SNR \propto \omega_0$[25].

1.2.8. EM modeling

To investigate the performance of RF coils in terms of magnetic field, efficiency, SAR, etc. electromagnetic field simulations are needed. Full-wave simulation methods solve the full Maxwell equations without static or quasi-static approximations. Different numerical solution methods exist including finite difference time domain (FDTD), method of moments (MoM) and finite element method (FEM). Each has specific characteristics in terms of accuracy, solution time, resolution etc. In this thesis, we use a full wave simulator called HFSS (High frequency structure simulator) to simulate the RF coil in presence of the phantom/human model. This simulator uses FEM to solve differential equations in the presence of boundary conditions. The advantage of FEM is its adaptive tetrahedral meshing which is advantageous for complex structures like the human anatomy. Adaptive meshing optimizes the accuracy and resolution of the simulation in each region of the structure. In addition to the electromagnetic fields, HFSS

generates *S* (scattering) and *Z* (impedance) parameters when appropriate excitation ports are used which allow the performance of the RF coil to be assessed and compared to bench measurements.

1.3. B_1 mapping

Determining the transmit RF field, $\mathbf{B}_1^+$, can provide valuable information. The homogeneity of the $\mathbf{B}_1^+$ field of an RF coil will significantly change when it is loaded due to conduction and displacement currents generated in the load. Hence it is desirable to find $\mathbf{B}_1^+$ field using acquired image data [22]. A simple method used to do $\mathbf{B}_1^+$ mapping in this thesis is the double angle method (DAM) [22] in which the ratio of image intensity obtained using two flip angles, α_1 and $2\alpha_1$ are compared. The ratio of these two images is independent of receive sensitivity, spin density and relaxation times as long as there is complete relaxation ($T_R \geq 5T_1$). The ratio of the image intensities can be written as

$$\frac{I_2(x)}{I_1(x)} = \frac{\sin(2\alpha_1)}{\sin(\alpha_1)} = 2\cos(\alpha_1). \tag{1.40}$$

Therefore

$$\alpha_1 = \arccos\left(\frac{I_2(x)}{2I_1(x)}\right). \tag{1.41}$$

Using this technique we are able to find the flip angle map for any arbitrary load using the image data [22].

1.4. Electrical properties of tissues

To model different tissues in electromagnetic simulations, we need to know the electrical properties of tissues. As there is conductivity, σ, associated with biological tissues due to ions in solution, the human body is dissipative or lossy. Therefore, the permittivity is complex ($\hat{\varepsilon} = \varepsilon' - j\varepsilon''$) where $\varepsilon'' = \sigma/\varepsilon_0\omega$ (assuming conduction is the only loss). Gabriel et al. in [26] has a detailed list of permittivity and conductivity of different biological tissues versus frequency which can also be accessed through Federal Communication Commission (FCC)

(https://www.fcc.gov/general/body-tissue-dielectric-parameters). Table 1 summarizes the approximate electrical properties of tissues used in this thesis at 200 MHz using data from FCC.

Table 1.1. Electrical properties some human tissues.

	ε_r	σ (S/m)
Grey matter	65.06	0.64
White matter	47.06	0.37
CSF	76.82	2.19
Skin	55.71	0.58
Fat	5.74	0.04
Muscle	60.86	0.76

In this thesis, we have used phantoms as well as an accurate body model designed by Ansoft in which each organ is defined in terms of the electrical properties with high accuracy (**Figure 1.13**).

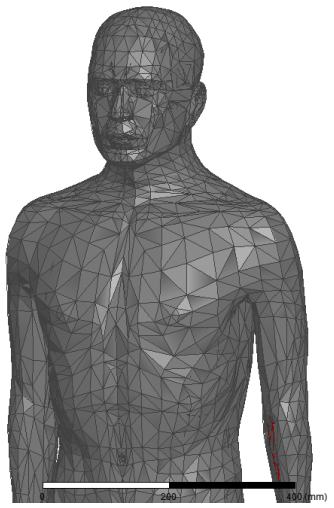

Figure 1.13. Ansoft human body model (male) with 2mm resolution and tetrahedral mesh.

1.5. Array configurations

Arrays are formed when two or more RF coils are used to image the same region and signal is acquired simultaneously from those elements [27]. In addition to allowing faster imaging, having

multiple smaller RF elements can increase image SNR [27]. Array elements will be positioned in a way to cover the volume of interest. Each element in an array may have its own separate receive/transmit chain to process signals coming from each channel independently in receive mode and send independent RF pulses through each channel in transmit mode [28].

1.5.1. Receive arrays

Receiving the signal with an array of elements will enhance the SNR while facilitating large FOV imaging. The most important parameter in receive mode is the SNR of the signal. In order to optimize SNR of an array, the signal from each element is recorded independently and will be post processed. The data is combined in different ways using different weighting coefficients depending on the desired objective. The weighting factors can be different from voxel to voxel in an image [25].

Consider an array which includes n elements. At a given voxel the image signals from the n receiver channels can be arranged into a vector, $\mathbf{s}= (\boldsymbol{s}_1 \quad \cdots \quad \boldsymbol{s}_n)$ and $\boldsymbol{\Psi}$ is the matrix of noise covariance between channels. In order to benefit imaging with arrays, one must use appropriate methods to weight and combine the signal coming from each element in the array. Adding images is non-optimal as each voxel has varying signal but the same noise level [29]. There are different methods to combine the received signals coming from each channel of which two are briefly discussed here [28]. Data is post-processed on a pixel by pixel basis for each location in space [28], [29].

1.5.1.1. Maximum SNR image

In this method, the signal from each pixel, is weighted by the noise covariance (Ψ) and the coil's sensitivity (C) at that location.

$$SNR = \frac{\boldsymbol{C}^H \boldsymbol{\Psi}^{-1} \boldsymbol{S}}{\sqrt{\boldsymbol{C}^H \boldsymbol{\Psi} \boldsymbol{C}}} \tag{1.42}$$

Where superscript H is the conjugate transpose [30]. This approach needs the information about coil's sensitivity at each pixel.

1.5.1.2. Root sum of square (RSS) images

In this common method, each pixel of the image is the square root of the sum of the squares of the pixel values corresponding to each element in the array. Therefore, prior knowledge of the coil's field maps is not needed to combine images. This will result in nearly optimal SNR images in most cases [28]. SNR corresponding to this method is given by

$$SNR = \frac{\boldsymbol{S}^H \boldsymbol{S}}{\sqrt{\boldsymbol{S}^H \boldsymbol{\Psi} \boldsymbol{S}}}. \tag{1.43}$$

Here $\boldsymbol{S}^H$ is the conjugate transpose of $\boldsymbol{S}$ and $\boldsymbol{\Psi}$ is noise covariance matrix [31].

1.5.1.3. Parallel imaging strategies

Parallel imaging takes advantage of the fact that the spatial distribution of the elements' sensitivity allows discrimination of the signal from different parts of the region of interest, and is thus a form of spatial encoding.

There are two important quantities associated with SNR loss in parallel imaging. The geometry factor, or *g*-factor describes the loss of SNR and depends on the correlation between different sensitivity patterns in an array. The more the sensitivity patterns are correlated, the higher is the g-factor therefore it is harder to separate the aliased pixel. The other important parameter is the acceleration factor, *R*, which is the ratio of the amount of the *k*-space data required for fully sampled image over that of accelerated acquisition [32].

Three are three main parallel imaging strategies. The first one is sensitivity encoding or SENSE [33] in which *k*-space is under-sampled and image acquisition is accelerated however aliasing is generated in the image [32]. Other parallel imaging techniques such as SMASH (simultaneous acquisition of spatial harmonics) [34] [35] and GRAPPA (generalized auto calibrating partially parallel imaging) [36], [32] which are *k*-space based techniques are also briefly discussed.

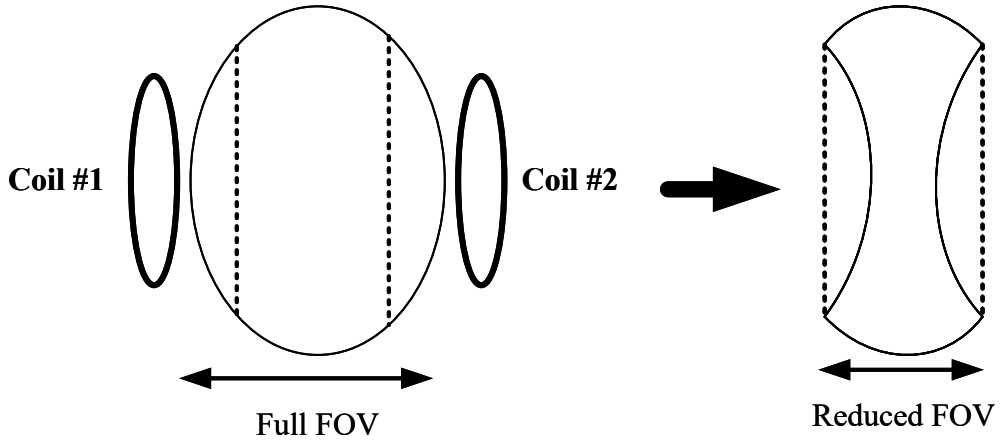

Figure 1.14. Parallel imaging (SENSE) of head using a two element array of coils each contributing to generate a reduced FOV image shown in right.

1.5.1.3.1. SENSE

SENSE works on the aliased image and it needs the accurate sensitivity profile of the coil. As the first step, the under-sampled *k*-space data is acquired leading to an aliased image. **Figure 1.14** shows how SENSE works for a two element array imaging head. Then using coil sensitivity profile for each element of the array and the aliased signal intensity, one would be able to extract the un-aliased signal intensity for each pixel [32].

$$F_n = I_A C_{An} + I_B C_{Bn} \tag{1.44}$$

Here F_n is the signal intensity of the aliased pixel for coil #n, I_A and I_B are the actual pixel values at points A and B which we are trying to find, and C_{An} and C_{Bn} are the coil #n sensitivities at locations A and B. Similar equations are written for each coil. Using matrix inversion the original pixel values (I_A and I_B) can be obtained [33].

In SENSE, SNR is reduced:

$$SNR_{PI} = \frac{SNR}{g\sqrt{R}} \tag{1.45}$$

where R is the reduction or acceleration factor and g is the geometry factor. g-factor takes into account the noise amplification therefore SNR loss when aliasing is reconstructed. It is basically a description of the ability of the coil array to encode magnetization distribution [37].

1.5.1.3.2. SMASH

In SMASH the sensitivity variation of the coil array in phase encode direction is used to approximate the spatial modulations that are obtained from phase encode gradients in unaccelerated imaging. The sinusoidal modulations of magnetization in the phase encode direction are associated with k-space lines that are normally sampled with phase encode gradients. Using linear combination of signals coming from different coils, sensitivity profiles are generated. The composite sensitivity profile is written as (1.46) [32]

$$C^{tot}(x,y) = \sum_k n_k C_k(x,y) \approx \exp\left(jm\Delta k_y y\right), \tag{1.46}$$

where m is an integer (representing the spatial harmonic number generated by the coil array), n_k are weighting factors and Δk_y is the minimum k-space interval in the y direction which is equal to $\Delta k_y = 2\pi/FOV$ [32]. Using the sensitivity profile, the combined data set in k-space is written as

$$\begin{aligned} S\left(k_x,k_y\right) &= \iint dxdyC^{comp}(x,y)\rho(x,y)\exp(-jk_x x - jk_y y) \\ &= \iint dxdy\rho(x,y)\exp\left(-jk_x x - j\left(k_y - m\Delta k_y\right)y\right), \end{aligned} \tag{1.47}$$

where $\rho(x,y)$ is spin density in the image plane. So, each combined dataset is shifted in k-space by $-m\Delta k_y$. Total combinations of the spatial harmonics will fill all the lines in k-space [34], [38].

1.5.1.3.3. GRAPPA

In GRAPPA, the missing k-space lines are regenerated before generating an image. Here data in neighboring points are combined to recover the missing parts of the k-space data. The weighting factors used to combine the above mentioned points are found using auto-calibration signal (ACS). ACS data is a lower resolution version of the accelerated image acquired most frequently

during the accelerated scan. Several source points are determined which both in undersampled and ACS data appear which yield weighting factors. The arrangement of these source points defines a kernel. Using multiple kernels GRAPPA weight set would be calculated using source and target points in ACS. The kernel is then used to fill the missing lines of the *k*-space. Once fully sampled, *k*-space is generated for each coil, Fourier transform is done for each coil and images are combined into a final image. In GRAPPA, SNR depends on *R* as well as its *g*-factor. However the *g*-factor associated with GRAPPA doesn't depends on the weighting factors [32], [36].

1.5.2. Transmit arrays

With control over phase and amplitude of each transmitting channel, one is able to perform RF "shimming" to control SAR and reduce $\mathbf{B}_1^+$ inhomogeneity. Moreover, distinct spatially selective RF pulses can be sent to each transmit channel with the benefit of reducing the RF power, or shortening RF pulse for selective spatial excitation [39].

1.5.2.1. RF shimming

One of the methods to mitigate the $\mathbf{B}_1$ field inhomogeneity is called RF shimming. In this method, different feeding patterns are designed each with a phase and magnitude to drive the RF coil array. RF shimming can be done in three forms including changing phase and magnitude of excitation one at a time or simultaneously [40].

1.5.2.2. Parallel transmit

Similar to parallel imaging described in the previous section, parallel transmission can be performed using transmitting coil arrays. The goal in parallel transmit is to excite *N* transmit coils each with a sensitivity profile, $S_i(x)$, simultaneously with undersampled excitation patterns, $P_i(x)$, to get the desired excitation pattern, $P_{des}(x)$ [39]. The coils' sensitivity profile would be determined using $\mathbf{B}_1$ mapping techniques described before.

$$P_{des}(x) = \sum_{i=1}^{N} S_i(x) P_i(x) \tag{1.48}$$

There are several methods to design RF pulses in parallel excitation which are briefly discussed here.

1.5.2.2.1. Spatial domain approach

In the case of parallel transmit using small tip approximation [41], transverse magnetization is the sum of magnetization produced by each coil considering each coil's sensitivity profile, $S_c(r)$ [42].

$$\boldsymbol{M}_{xy}(r) = j\gamma \boldsymbol{M}_0 \sum_{c=1}^{C} S_c(r) \int_0^T \boldsymbol{B}_{1c}(t) e^{j\boldsymbol{r}.\boldsymbol{k}(t)} dt \tag{1.49}$$

Here $\boldsymbol{M}_0$ represents the equilibrium magnetization and T is the pulse duration. The number of coils is C, each exciting with a unique RF pulse $\mathbf{B}_{1c}(t)$. This expression can be written in matrix form by discretizing space and time.

$$m = Ab \tag{1.50}$$

Here A is the matrix incorporating each coil's sensitivity profile modulated by Fourier kernel because of k-space trajectory, m is the target profile and b includes RF waveforms. Using least square optimization technique over the region of interest, b can be found using equation [43].

$$b = arg_b \, min\{\|Ab - m\|_w^2 + R(b)\} \tag{1.51}$$

Here w is the weighting factor and $R(b)$ is a regularization factor that controls the RF power [42], [43]. This approach is based on spatial domain.

1.5.2.2.2. Frequency domain approach

In contrast to the previous approach, transmit SENSE is formulated in k-space or frequency domain [39]. This approach uses transmit sensitivity patterns in the pulse design process. The Fourier transform of $\mathbf{M}(x)$ due to simultaneous excitation is given by

$$p(k) = \sum_{c=1}^{C} S_c(k) \otimes p_c(k) \tag{1.52}$$

Where S_c is the Fourier transform of the transmit sensitivity pattern for each coil convolved by p_c which is the Fourier transform of the excitation profile of each coil. After disretzation and matrix formation,we will have

$$p = S_{full} p_{full} \tag{1.53}$$

The RF pulse profile for each element is found using least square optimization with the regularization factor $R(P_{full})$.

$$\hat{p}_{full} = arg_{p_{full}} min \left\{ \left\| S_{full} p_{full} - p_{des} \right\|_w^2 + R(p_{full}) \right\} \tag{1.54}$$

Where P_{des} is the Fourier transform vector of the desired excitation pattern [44], [45].

1.5.2.2.3. Removing aliasing approach

This method uses the transmit sensitivity patterns however it is formulated as an optimization problem in spatial domain. This approach considers the aliasing pattern in spatial domain as a result of undersampling in *k*-space to solve for the excitation pattern for each coil. As this method is based on aliasing removal, aliases must be coherent and regular [46]. If undersampling is done in *y*-direction in a two dimensional Cartesian trajectory in *k*-space, the excitation pattern is written equation [46].

$$M(x,y) = \sum_{c=1}^{C} S_c(x,y) \sum_{m=-\infty}^{\infty} u_c(x, y - m\Delta) \tag{1.55}$$

Here u_c is the excited pattern for each coil using fully smapled *k*-space trajectory and Δ is desined as spacing for accelerated factor *R*.

$$\Delta = {}^{FOV}/_{R} \tag{1.56}$$

(1.55) can be written as

$$M(x,y) = \sum_{m=-\infty}^{\infty} m_{des}(x, y - m\Delta) \sum_{c=1}^{C} h_c(x, y - m\Delta) S_c(x,y) \tag{1.57}$$

The term $\sum_{c=1}^{C} h_c(x, y - m\Delta) S_c(x, y)$ is equal to 1 only if m=0. Therefore for each point in FOV matrix equation can be wrtitten as

$$\begin{bmatrix} S_1(x,y) & \cdots & S_C(x,y) \\ \vdots & \ddots & \vdots \\ S_1(x,y+m\Delta) & \cdots & S_C(x,y+m\Delta) \end{bmatrix} \begin{bmatrix} h_1(x,y) \\ \dots \\ h_C(x,y) \end{bmatrix} = \begin{bmatrix} 1 \\ 0 \\ \dots \end{bmatrix} \quad (1.58)$$

Again least square method can be used to yield exciattion pattern for each coil [46], [47].

1.5.2.2.4. Three dimensional excitation

Slice selective RF pulses are used to excite the spins only in a slice of the imaging region while leaving the rest of the spins aligned with $\mathbf{B}_0$. This will simplify the encoding stage as a two-dimensional slice is excited. Other than slice selectivity, RF pulses can be spatially tailored to compensate for $\mathbf{B}_1$ field inhomogeneities caused at high fields [48]. One type of 3D pulse that uses slice select gradient along z direction and phase encode along x and y is called fast-kz as kz is rapidly traversed with a number of slice select sub-pulses as shown in **Figure 1.15**. With this type of pulses thin slices can be excited [49]. As the trajectory is a straight line, these pulse segments are also called as "spokes"[48].

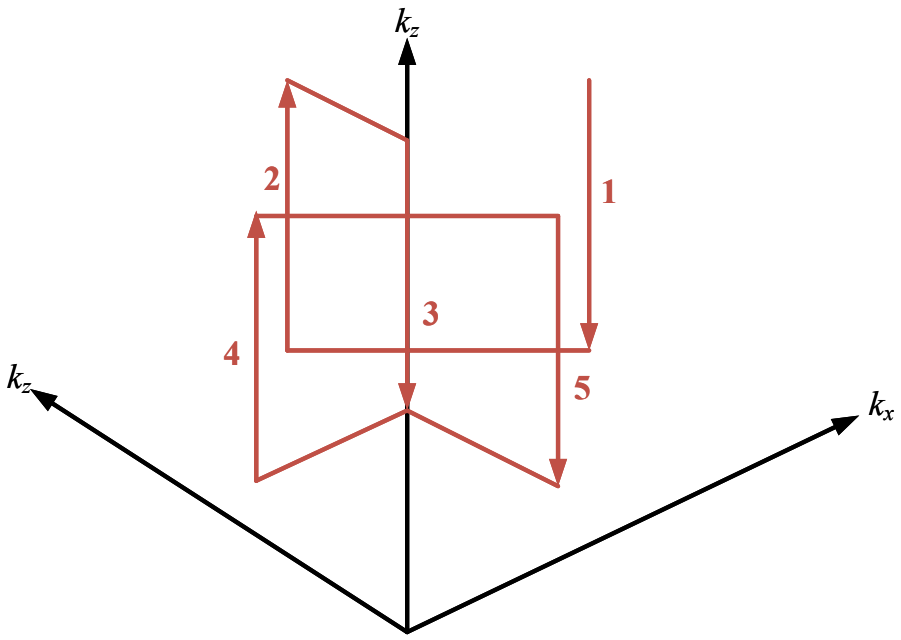

Figure 1.15. k-space trajectory of a fast k_z 3D RF pulse [48].

1.6. Motivation

This thesis mainly focuses on the RF coils used at high field strength, specifically 4.7 T. High field strength (>3T) provides higher SNR images however there are several challenges associated with this field strength. The first issue is the inhomogeneity of the RF magnetic field due to short wavelength. This results in dark or bright areas in the acquired images therefore degrading the diagnostic quality. Figure **1.16** shows the inhomogeneity in the acquired image of brain at 4.7T using a standard volume resonator. In the literature, transmit arrays with control over phase and amplitude of each element have been used to reduce the inhomogeneity by spatially tailoring the excitation profile of the generated $\mathbf{B}_1^+$ field [50].

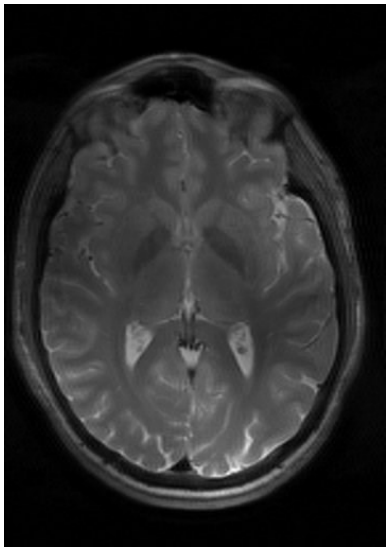

Figure 1.16 Inhomogeneity in B_1^+ field resulting in dark and bright areas at 4.7T[1].

Alternatively, placing dielectric pads in proximity of the imaging region is shown to be an effective method to increase the signal locally and also increase the magnetic field homogeneity [51]. The use of local high permittivity pads is becoming more common, but the effect of larger dielectric pads on transmit/receive performance of an array (e.g., coupling, efficiency and safety) has not been investigated in detail. Indeed, elements in arrays are tightly arranged, leading to significant coupling. By minimizing coupling between elements, signal and noise transfer is minimized and also distinct field maps needed for parallel imaging are achieved.

[1] Image courtesy of Kelly McPhee.

High field imaging of the body region is more challenging than in the brain due to the larger FOV relative to wavelength. Conventional RF coils such as loops fail to be efficient at high frequencies as they their performance degrades at higher depth, whereas antennas such as dipoles perform more efficiently [52]. In designing RF coils for body imaging additional challenges such as increased SAR, lower penetration depth and inhomogeneity in the magnetic fields must be considered.

1.7. Scope of This Thesis

Chapter 2 investigates the performance of an array for imaging the extremities or pediatric brain at 4.7 T (200 MHz) in which a dielectric liner surrounds the whole volume of interest. Using simulations and measurements we show that a compromise must be made between improvements in field homogeneity and transmit performance and that for several metrics an optimal permittivity exists which is below the values that are commonly used in the literature.

Additionally, mutual impedance between array elements plays a substantial role at high frequencies and is increased by the presence of dielectric pads. Therefore, **chapter 3** describes a decoupling strategy for an eight-channel transmit/receive array in the presence of a high permittivity dielectric liner. The elements are decoupled using capacitive bridges between adjacent elements. In spite of the higher mutual impedance due to the liner, both mutual resistance and reactance can be removed between adjacent elements, and coupling between non-adjacent elements is maintained below -15 dB. The effects of decoupling on the transmit performance of the coil array in presence of high permittivity liners are investigated in terms of coupling, magnetic field intensity, SAR and transmit efficiencies.

Chapter 4 introduces the TEM horn antenna as an efficient element for high field imaging. Horn antennas, frequently used in high gain, directive applications in radar and communication systems, show promising results for imaging body regions at high fields. In simulations a single horn antenna is compared with a more common dipole element at the same frequency, 200 MHz, for 4.7 T. Results show significant improvement in terms of transmit efficiency, penetration depth, SNR and SAR. Moreover, an array of horn antennas was constructed to image a torso size phantom.

Chapter 5 summarizes the thesis and outlines future work.

Appendix A describes the method of measurement of complex permittivity for the ceramic suspensions that were used in chapters 2 and 3. This method is used to measure complex permittivity of powders (water insoluble), solutions and suspensions using a parallel-plate capacitor cell. An impedance analyzer measures the cell's impedance through an appropriate test fixture. The cell's impedance is fitted to an equivalent circuit using a MATLAB script and the permittivity of the material is extracted after calibration with known materials. The permittivity of the solid material is obtained from that of the powder suspension using known mixing rules.

Chapter 2

Optimal-permittivity Liners for a 4.7T Transceive Array[2]

2.1. Introduction

High static magnetic field MRI promises high signal-to-noise ratio (SNR) but is limited by radio frequency (RF) magnetic field ($\mathbf{B}_1$) inhomogeneity due to short wavelength. These inhomogeneities in $\mathbf{B}_1$ field degrade image quality and lead to bright and dark areas in the image [53]. To mitigate these effects, array excitation with control over the phase and amplitude of each element has been developed [54]. Flexible bags filled with dielectric material placed strategically around the region of interest (ROI) have also been shown to enhance $\mathbf{B}_1$ field homogeneity and increase efficiency locally [55].

Dielectric pads have been increasingly used as a tool to focus magnetic field locally and hence increase SNR in an ROI [56], [57]. Early dielectric pads were designed to have approximately the same dielectric constant as nearby tissues (e.g., gelatin-honey gels) to prevent electromagnetic field reflections at the dielectric boundary [58].

More recently, high dielectric constant (HDC) pads with relative permittivity $\varepsilon_r > 100$ have become popular [55], [56], [59], [60]. Reference [60] shows that significant increases (20% and greater) in SNR and reduction in input power are achieved by HDC pads placed locally. Specific absorption rate (SAR) has also been investigated [60], [61], [62], [63]. In some cases [60], [63], by introducing local HDC pads, SAR decreases as a result of reduction in input power to generate the same amount of $\mathbf{B}_1$ field.

The HDC material is made by mixing powdered ceramics such as barium or calcium titanate ($BaTiO_3$ and $CaTiO_3$) with deuterium oxide (D_2O) or deionized water, resulting in a suspension or slurry that is then sealed in plastic bags [60], [64], [59]. The resulting permittivity depends on the volume ratio of the constituents and the dielectric constants of the bulk materials. Such

[2] This chapter has been submitted to Physics in Medicine and Biology.

suspensions present challenges such as the risk of contamination if the pad were to leak toxic materials to the patient [57]. Moreover the suspension can easily settle or deform which can change the dielectric constant and thickness of the pad [65], while the resulting large regions of liquid water give undesired visible signals. Finally, high-permittivity ceramics and D_2O are expensive materials which add dramatically to the cost of the pads.

While most authors use local pads to focus the magnetic field, in this chapter we investigate the effect of dielectric materials placed surrounding, and in contact with, the imaging volume. A similar arrangement was reported by [66]; there, however, the dielectric is located between the RF shield and coil conductors, which are separated from the imaging volume by an air gap. We determine the permittivity that optimizes operation of an array for imaging the extremities or pediatric brain at 4.7 T, and the transmit and receive performance of the array are evaluated based on parameters such as coil efficiency, $\mathbf{B}_1$ field, SAR and coupling between elements.

The first section of this chapter outlines the theory on why dielectric liners increase signal intensity as well as their effects at high fields. The methods section describes the design procedure of the array and optimized liner and includes simulation results. Moreover, the array is fabricated and bench measurement and scanning results are included in this section.

2.2. Theory

In phasor notation, Ampere's law with Maxwell's correction in a conductive medium is given by [24]

$$\nabla \times \boldsymbol{H} = \boldsymbol{J}_D + \boldsymbol{J}_C = j\omega\varepsilon\boldsymbol{E} + \sigma\boldsymbol{E} \tag{2.1}$$

Where $\boldsymbol{H}$ is the magnetic field (A/m), $\boldsymbol{E}$ is the electric field (V/m), ω is the angular frequency, $\boldsymbol{J}_D$ is the displacement current density and $\boldsymbol{J}_C$ is conduction current density (A/m^2). The dielectric constant, or permittivity (ε, typically expressed relative to that of vacuum, ε_0 = 8.85×10^{-12} F/m), and conductivity (σ) define the electric properties of a medium [24]. Equation (2.1) shows that for a given electric field, the displacement current, and thus the magnetic field it induces, are proportional to permittivity.

The ratio of conduction current to displacement current shows that the displacement current becomes increasingly important at higher frequencies [56].

$$tan\delta = \frac{\boldsymbol{J}_C}{\boldsymbol{J}_D} = \frac{\sigma}{\omega\varepsilon_r\varepsilon_0}. \tag{2.2}$$

At 4.7T, the Larmor frequency is 200 MHz, and for a biological medium with $\varepsilon_r = 78$ and conductivity of 0.8 S/m, this ratio is near unity. Placing dielectric materials in proximity of the phantom further enhances the displacement currents locally due to the high dielectric constant of these materials and their low conductivities [56]. The enhanced magnetic field in the regions adjacent to the dielectric results in a local enhancement of SNR.

The geometry of the coil array and the liner investigated in this work is shown in **Figure 2.1**. The imaging volume (phantom) is the inner cylinder, and is surrounded by an annular region of low-loss dielectric. The array's conductors are located on a 5-mm-thick acrylic (PMAA) former surrounding the liner. Consequently, four regions of dielectric media are present beginning with the outermost air region. Second is the PMAA former which is very thin, and thus negligible, compared to wavelength (thickness< λ/10), followed by the low-loss dielectric annulus and lastly the lossy imaging region (phantom).

When an electromagnetic field impinges on the boundary between two dielectric materials, it will experience some reflection due to the difference in the intrinsic impedance, $\eta = \sqrt{\frac{\mu}{\varepsilon}}$, of the two media [24]. Therefore, the electromagnetic fields encounter primarily two dielectric boundaries where they will experience some reflection and transmission due to mismatches in the impedances of the media. The dielectric constant of the annulus determines not only the ratio of the displacement current to the conduction current, but also the reflection experienced by the fields and thus the penetration into the imaging region (phantom).

Because transmission and reflection happen in the near-field region, the reflection at the boundaries does not follow the simple equations that apply in the far field. However, the mismatch between the impedances of the two media will cause field reflections.

Coupling due to mutual impedances between array elements is also an important quantity that affects performance. Mutual impedance, $Z_{12} = R_{12} + jX_{12}$, is responsible for signal and noise

transfer between coupled elements. Using reaction theory, mutual impedance can be expressed as a function of the electromagnetic fields generated when coils are excited [67], [68]. By considering the equation for mutual impedance, (2.3), it can be theoretically verified that increasing the dielectric constant increases the mutual impedance directly.

$$
\begin{aligned}
Z_{ij} &= \frac{-1}{I_i I_j}\left\{\iiint_{phantom+pad} \boldsymbol{E}^j(r).\boldsymbol{J}_p^i(r)dv + \iiint_{coil} \boldsymbol{E}^j(r).\boldsymbol{J}_c^i(r)dv\right\} \\
&= \frac{-1}{I_i I_j}\left\{\iiint_{phantom} (\sigma_p + j\omega\varepsilon)\, \boldsymbol{E}^j(r).\boldsymbol{E}^i(r)dv \right. \\
&\left. + \iiint_{pad} j\omega\varepsilon\, \boldsymbol{E}^j(r).\boldsymbol{E}^i(r)dv + \iiint_{coil} \boldsymbol{E}^j(r).\boldsymbol{J}_c^i(r)dv\right\}
\end{aligned}
\tag{2.3}
$$

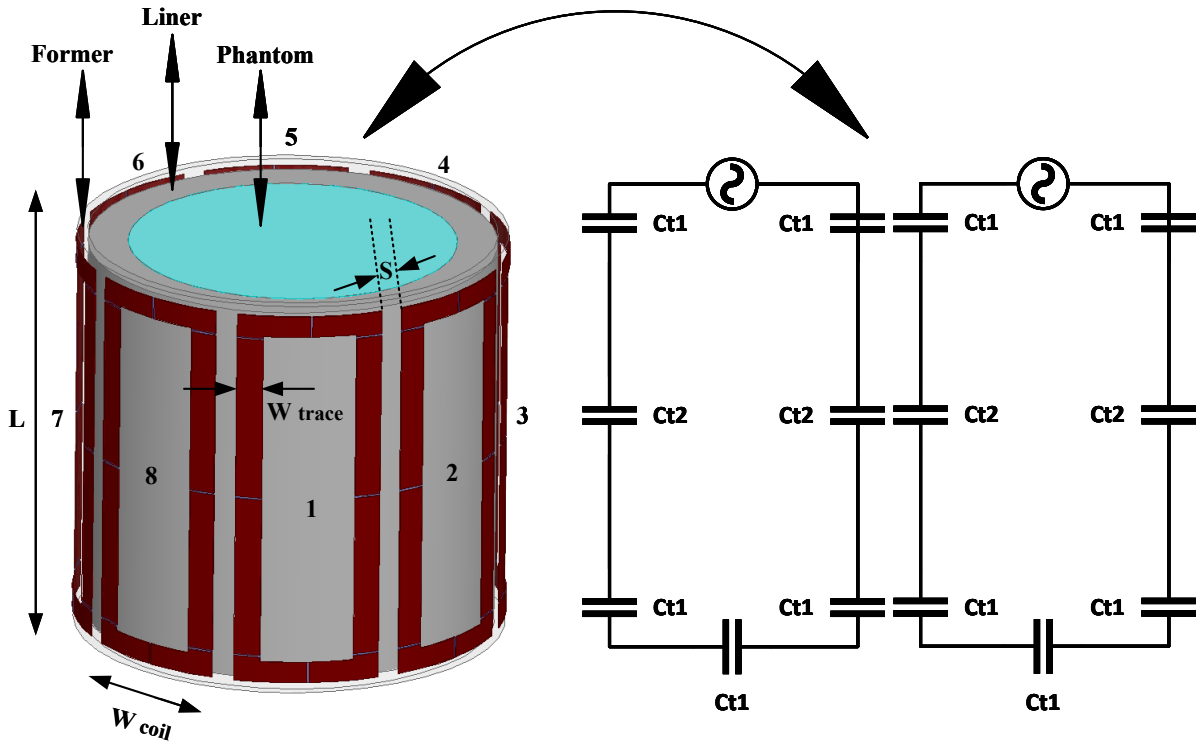

Figure 2.1. Designed head coil array.

Here $\boldsymbol{E}^j(r)$ is the electric field generated by the current, $\boldsymbol{I}_j$, on coil j. The term $\boldsymbol{J}^i_c(r)$ refers to the current density on coil i and term $\boldsymbol{J}^i_p(r)$ is the current (conduction and displacement) induced in the phantom and HDC pads by the fields of coil i.

With the introduction of a high permittivity material instead of the air region between coil and phantom there is an increase in mutual impedance. The increase is even more significant for mutual resistance which is often negligible compared to the imaginary component when low dielectric constant pads (ε_r<<100) or air fills the gap between coil and phantom. When HDC pads are used both components of the mutual impedance are significant, and the overall increase creates challenges in coil array decoupling because both terms of the mutual impedance must be removed to avoid signal, power and noise transfer between channels.

The final parameter that is important in investigating the dielectric pad performance and safety is the resonant frequency of the liner. The dielectric liner as a cylinder will behave like a dielectric resonator which has a fundamental resonance frequency as well as additional modes at higher frequencies. The resonant frequency of the dielectric liner should be safely away from the resonant frequency of the coil array (200 MHz) to prevent a dangerous enhancement of fields and consequently SAR.

In summary, it is important to understand the effect of displacement currents as well as reflections on coil performance and safety in order to use the appropriate dielectric material. In the following section, different dielectric materials are used and their effects on the transmit performance of the coil are investigated.

2.3. Methods

2.3.1 Design

The current structure as shown in **Figure 2.1** is designed to image pediatric head or extremities. A lossy phantom with relative dielectric constant $\varepsilon_r = 76$ and conductivity of $\sigma = 0.8\, S/m$ is used to mimic the dielectric properties of brain. The phantom has the outer diameter of 150 mm and its height is 180 mm. A liner with a range of permittivities and thickness of 2 cm surrounds the phantom as shown in **Figure 2.1**. In order to cover the FOV, the coil array consist of eight loops conformed to a PMMA cylindrical former.

Each element in the array is a rectangular loop and capacitors are designed to make the elements resonate at 200.4 MHz which is the Larmor frequency for ^{1}H at 4.7T. These capacitors are distributed along the coil to guarantee a uniform current distribution on the coil. Designed dimensions of the structure are organized in **Table 2.1**.

In this section, we compare liners having a wide range of permittivities including the case where no liner is present (air). HDC pads with permitivities greater than 100 have been popular recently. Therefore, in this work the highest dielectric constant material is chosen to be ε_r=150. The second material is chosen to have the permittivity close to that of the phantom hence de-ionized water is used (ε_r=78).

Table 2.1. Design parameters for the coil array.

W_{trace} (mm)	W_{coil} (mm)	L (mm)	S (mm)	Ct_1 (pF)	Ct_2 (pF)
10	69	180	10	13	15

Finally, we have designed an optimized permittivity liner based on minimizing the electromagnetic reflections at dielectric boundaries. As can be seen in **Figure 2.2**, there are two dielectric boundaries for an electromagnetic field, medium/liner and liner/phantom respectively. Electromagnetic field generated by the RF coil will experience reflections at each of these boundaries based on their impedances. The intrinsic impedance of a medium having relative permittivity ε_r (and permeability μ_0) is given by [24].

$$Z = \frac{Z_0}{\sqrt{\varepsilon_r}}\ , \varepsilon_r = (\frac{Z_0}{Z})^2\ , \tag{2.4}$$

where Z_0 is the intrinsic impedance of free space (377 Ω). The impedances that electromagnetic fields experience in PMMA and phantom is 189 Ω and 43.2 Ω respectively. In order to minimize the reflections at the dielectric boundaries, the liner is designed as a layer to match the impedance of the medium to that of the phantom. This material's impedance is equal to the geometric mean of the impedances of these two layers resulting in 90.3 Ω. The resulting permittivity of the matching layer would be approximately 17.5.

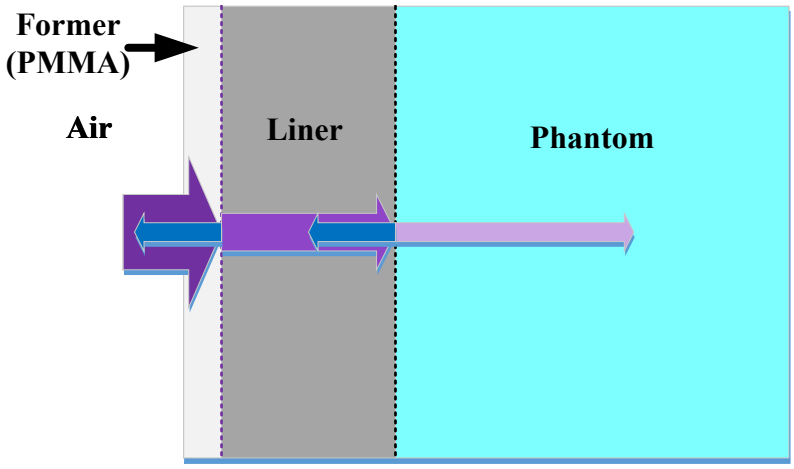

Figure 2.2. Different dielectric layers and boundaries.

2.3.2 Simulation

To investigate array performance, full-wave simulations of the complete structure were performed for each liner material using High Frequency Structure Simulator (HFSS V.15, Ansys, USA). The domain was bounded by a perfect cylindrical conductor with radiation boundaries at both ends to mimic the magnet bore, as shown in **Figure 2.3**. Each element of the array is excited by a lumped port with 1 W of incident power, resulting in fields and scattering (*S*) parameters that can be exported for further processing. Specifically, the fields can be combined in any linear combination such as quadrature excitation (equal magnitude, with phase distributed progressively around the circle) or single-channel excitation to compare to experimental data. Simulations using 1 A current sources on each element were also performed (including all capacitors) to eliminate the effects of matching.

The permittivity of the liner was varied between the four values mentioned in the **Design** section plus $\varepsilon_r = 35$ to complete an approximate geometric progression. The resonant frequency of the fundamental dielectric resonance mode of each liner was found by performing an eigenmode simulation for each isolated liner within radiating boundaries.

2.3.2.1 Dielectric Resonance

The liner is an annular cylinder of dielectric material and thus can behave as a dielectric resonator. A dielectric resonance will degrade the performance of the coil array and also

introduce safety issues similarly to the effects of a traditional resonator, such as a small surface coil, placed within a volume coil. Therefore, the resonant frequency of the fundamental dielectric resonance mode of each liner was found by performing an eigenmode simulation for each isolated liner within radiating boundaries.

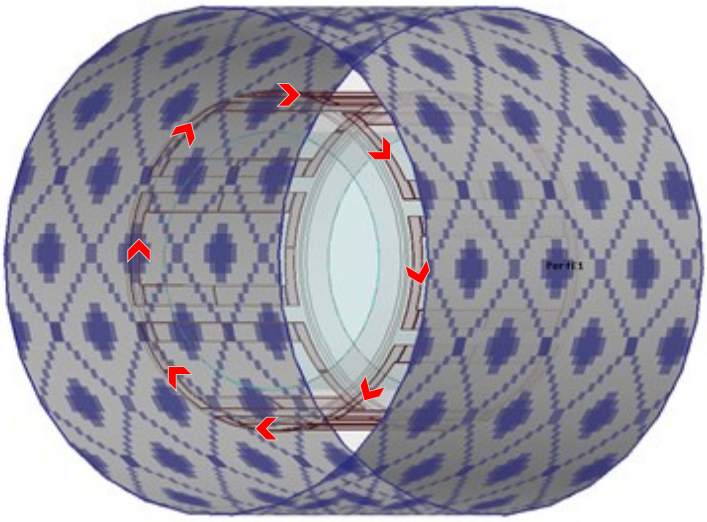

Figure 2.3. Simulation of the structure in HFSS.

2.3.2.2 Generalized S parameters

The wide range of permittivities used for the liner can modify matching conditions, and thus the corresponding coupling, considerably. To eliminate these differences in coupling due to matching, the S matrices are modified by introducing matching circuits adjusted so that the matching in each case is the same. Firstly, the S matrix is pre- and post-multiplied by a diagonal matrix of phase offsets (i.e., a shift in reference planes) which accounts for the phase component of each matching circuit. Then the formalism of generalized S parameters is used to calculate a new S matrix having minimal values of $|S_{ii}|$ for an appropriate choice of new reference impedances (which is equivalent to matching by means of ideal transformers) [69]. The phase offsets and reference impedances are found by numerical optimization.

2.3.2.3 Results

While insertion of the dielectric liner can degrade coil matching by introducing a reflection boundary between the coil and the phantom, if the permittivity is designed to match these two layers, S_{11} can actually be reduced which means more power can enter the phantom.

A fair comparison of coupling requires removing these differences in S_{11} by introducing matching circuits (see **Generalized S parameters** above). As can be seen in **Figure 2.4**, the impedance-matching alumina liner (b) results in minimal coupling overall.

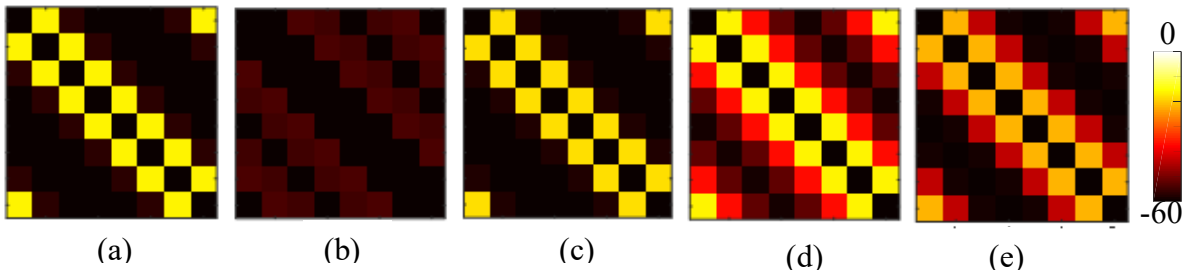

Figure 2.4. Comparison of the scattering (S) matrix (8-channel) [-60dB 0] (dB) at 200 MHz after matching for different dielectric liners (ε_r=1 (a), ε_r=17.5 (b), ε_r = 35 (c), ε_r=78 (d), and ε_r=150 (e), respectively) in the presence of an ideal matching network at each port (S_{ii}=0).

An important reason for using high permittivity liners is to increase RF magnetic field homogeneity. The $\mathbf{B}_1^+$ field homogeneity plots in the central transverse plane (**Figure 2.5**) show that by increasing the permittivity of the liner, magnetic field inhomogeneity improves in the transverse plane due to the effects of local displacement currents. There is only a minor difference between liners with ε_r=78 and ε_r=150, which supports the conclusion that high permittivities are not needed. Furthermore, looking at sagittal slices (**Figure 2.6** and **Figure 2.7**) we observe that, especially when high dielectric liners are used, longitudinal homogeneity is significantly degraded.

The inhomogeneity is defined as the standard deviation of the $\mathbf{B}_1^+$ field relative to its mean (i.e., the coefficient of variation, CoV), measured over the entire phantom volume, as shown in **Table 2.2**. The table also shows the transmit efficiency and field parameters when each element is excited with 1A current (quadrature excitation). Note that the high permittivity liners reduce the peak and average $\mathbf{B}_1^+$ field as a result of reflection at the boundary, but also create a phase

delay in the longitudinal direction [66] which results in a corresponding asymmetry. **Figure 2.7** shows the SAR pattern plotted over the central transverse slice and a sagittal slice of the phantom, where the longitudinal asymmetry is clearly visible, with one or more SAR hot spots appearing at the driven end of the array.

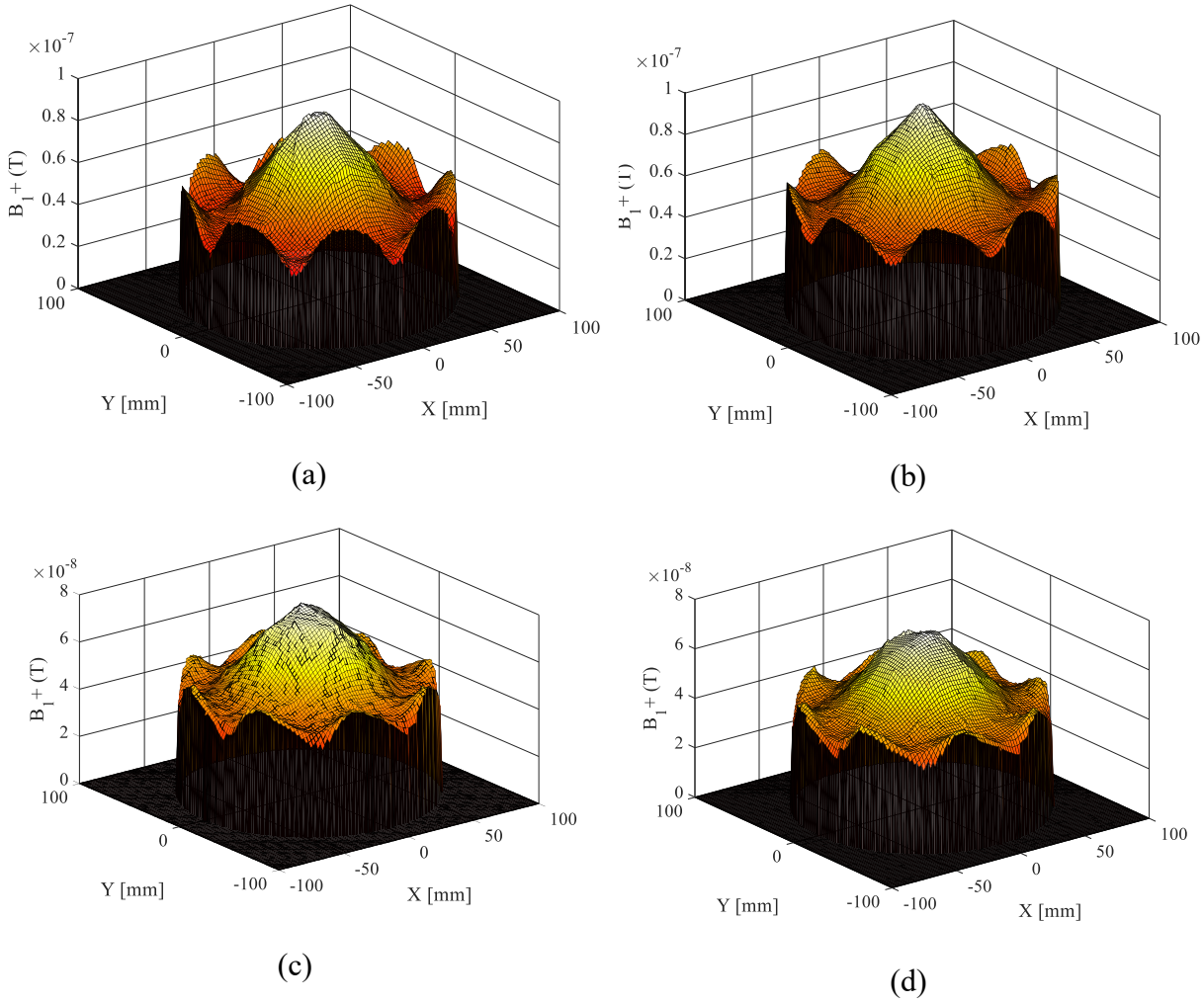

Figure 2.5. B_1^+ field over a transverse slice in the middle of the phantom with different liner permittivities (a) ε_r=1 (air), (b) ε_r=17.5, (c) ε_r=78, (d) ε_r=150.

Excitation and safety excitation efficiency are defined as $E_v = \boldsymbol{B}_1^+/\sqrt{P_v}$ and $S_v = \boldsymbol{B}_1^+/\sqrt{\max(SAR_{10g})}$, respectively [70], where P_v is the power deposited in the volume of interest (VOI), and SAR_{10g} is the 10-gram average SAR. High permittivity liners degrade both transmit efficiencies by at least 15% compared to the unlined case because of lower $\boldsymbol{B}_1^+$ fields produced

by approximately the same power or SAR. However, changes in efficiency using the matching liner are insignificant. The ratio of maximum SAR to mean SAR is an important safety parameter when comparing different cases. As can be seen in **Table 2.2** this ratio starts to increase by using HDC liners.

Table 2.2. Transmit performance parameters of the coil array in presence of the different dielectric liners at 200 MHz (HFSS simulation, 1A quadrature excitation).

	ε_r=1	ε_r =17.5	ε_r =35	ε_r =78	ε_r =150
Resonant frequency of liner (MHz)	-	549	436	292	216
B_1^+ standard deviation/mean (volume)	26.3%	34.4%	35.1%	38.4%	42.7%
B_1^+ standard deviation/mean (slice)	23.9%	19.7%	18.7%	18.4%	17.2%
$B_{1,avg}^+/\sqrt{P_V}$ **(μT/W)**	0.52	0.50	0.47	0.46	0.42
$B_{1,avg}^+/\sqrt{max(SAR_{10g})}$ **(μT/(W/Kg))**	0.68	0.65	0.55	0.49	0.43
Max (SAR)/mean(SAR)	2.10	2.18	2.6	3.05	3.58

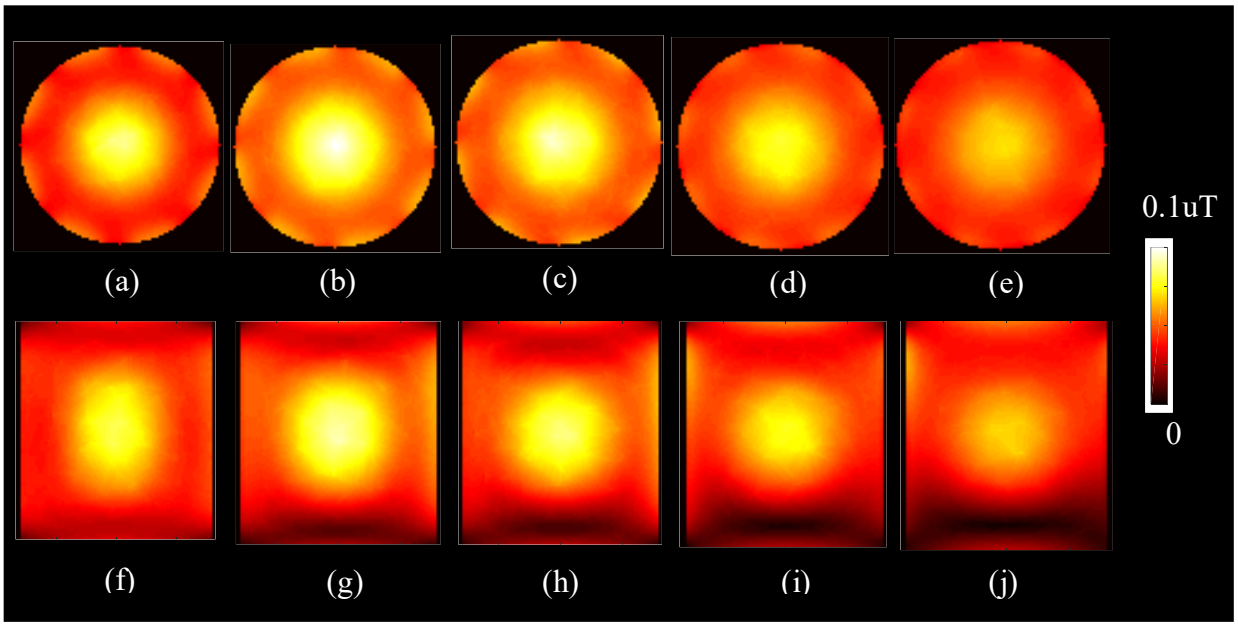

Figure 2.6. B_1^+ in a transverse slice in middle of the phantom and a sagittal slice with different liner permittivities: ε_r=1 (a, f), ε_r=17.5 (b, g), ε_r=35 (c, h), ε_r=78 (d, i), and ε_r=150 (e, j). Note the longitudinal asymmetry resulting from high-permittivity liners.

Table 2.2 also lists the resonant frequency of each liner as a dielectric resonator. Each liner looks like a cylinder of dielectric material hence would behave as a resonator. If the liner resonates, it will degrade the performance of the coil array and also cause safety issues. Therefore, it is important to look for the resonant frequency of each liner. As expected, the higher the permittivity, the lower is the resonant frequency of the dielectric resonator, which in the case of ε_r=150 is dangerously close to 200 MHz while with lower permittivities it is far from the coil's resonant frequency and thus safer to use. Note that for an array built for the adult head or tuned to 7 T, the dielectric resonant frequency of a high-permittivity liner is well within the dangerous range.

Single-element field maps (1 W port excitation) are shown in **Figure 2.13** (top row). As observed for the quadrature fields (**Table 2.2**), high-permittivity liners degrade the penetration of fields deep inside the VOI, while nearer to the transmitting element the effect on the field intensities is minimal.

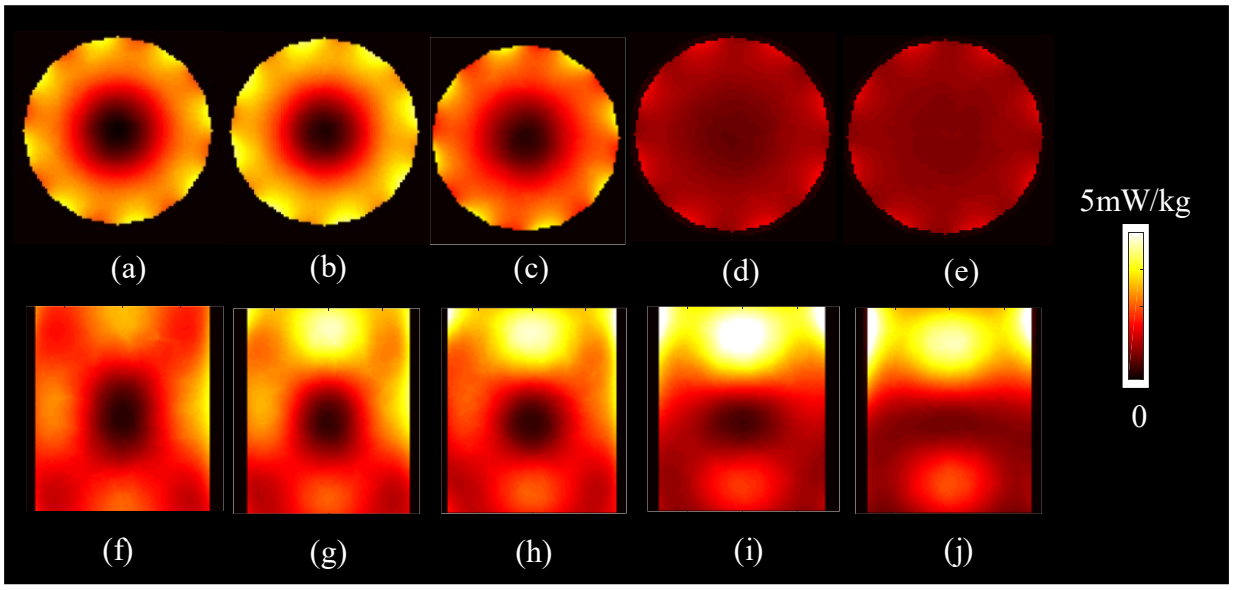

Figure 2.7. Local SAR in a transverse slice in middle of the phantom and a sagittal slice with different liner permittivities: ε_r=1 (a, f), ε_r=17.5 (b, g), ε_r=35 (c, h), ε_r=78 (d, i), and ε_r=150 (e, j). Note the longitudinal asymmetry resulting from high-permittivity liners.

2.3.2.4 Effect of air-gap

The effect of air-gap between liner and phantom on its performance is investigated by adding an air-gap with the same thickness of the liner to the structure when matching layer is used. Simulations are performed and results show that matching and coupling are not changed between these two cases. Fields and efficiencies are compared in **Table 2.3**. As can be seen the transmit efficiency and safety efficiency are insensitive to adding air-gap between phantom and liner.

Table 2.3. Summary of results comparing fields and efficiencies for the case where no air-gap is present versus adding air-gap between phantom and liner.

	With air-gap	**Without air-gap**
B_1^+ standard deviation/mean (volume)	28.28%	34.4%
B_1^+ standard deviation/mean (slice)	23.28%	19.7%
SAR standard deviation/mean (volume)	33.74%	50%
$\boldsymbol{B_{1,avg}^+/\sqrt{P_V}}$ **(μT/W)**	0.48	0.5
$\boldsymbol{B_{1,avg}^+/\sqrt{max(SAR_{10g})}}$ **(μT/(W/Kg))**	0.66	0.65
Max (SAR)/mean(SAR)	2.21	2.18

2.3.3 Fabrication

2.3.3.1 Liner

The highest dielectric constant material, ε_r=150, is made using a barium titanate ($BaTiO_3$) powder suspension made by mixing the ceramic powder (Alfa Aesar, MA, USA) with water with volume ratio of 0.3 ($^{V_{BaTiO3}}/_{V_{Water}} = {}^{3}/_{7}$) as shown in **Figure 2.8** (a). The second material is de-ionized water which has a permittivity approximately equal to that of the phantom (ε_r=78) (**Figure 2.8** (b)).

The resulting relative permittivity of 17.5 was achieved using a suspension of alumina (Al_2O_3, Manus Abrasive Systems Inc.) and water with volume ratio of 0.5 ($V_{Alumina} = V_{Water}$). This mixture (**Figure 2.8** (c)) is very stable and biologically safe (in case it leaks). All materials are inserted into heat-sealable food storage bags (layered polyethylene and polyamide film) measuring approximately 18×6×2 cm, a number of which can be readily packed to fill the annular space between the phantom and coil holder.

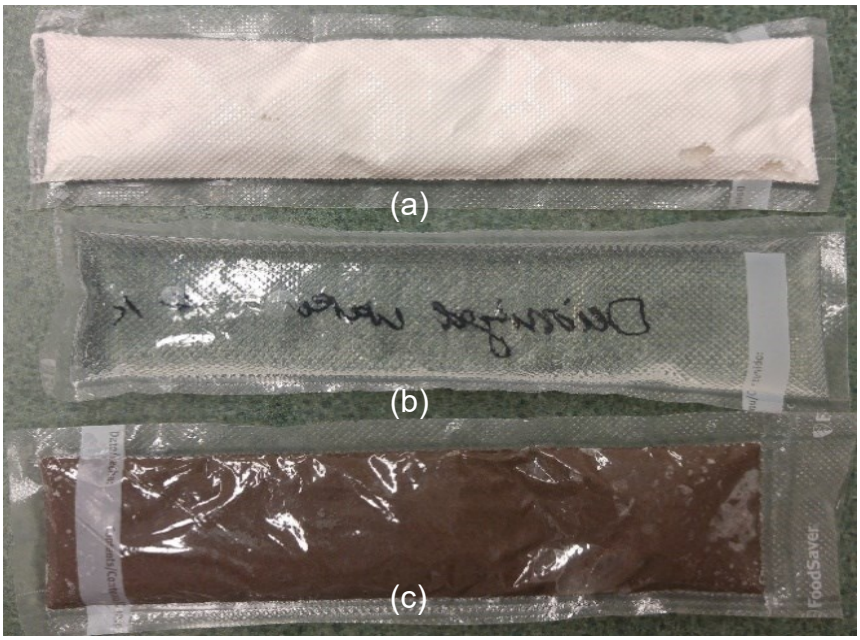

Figure 2.8. Fabricated dielectric pads: (a) high dielectric constant pad (ε_r=150), (b) water pad, (c) matching pad (ε_r=17.5).

2.3.3.2 Array

The array consists of eight rectangular loops (dimensions in **Table 2.1**) made of copper tape conductors conformed to a 200-mm-diameter acrylic (PMMA) cylinder to accommodate a small head or the extremities. Capacitances required to make the elements resonate at 200 MHz are distributed over 8 gaps in each coil to ensure uniform current distributions. Each element includes a tuning capacitor at the side opposite the feed, which consists of a lattice balun (integrated balun and matching circuit). A coaxial cable 150 cm in length is connected to each feed circuit and all 8 cables are connected to a single grounding point consisting of an aluminum plate populated with BNC bulkhead connectors.

A lossy cylindrical phantom 150 mm in diameter and 180 mm in length is filled with a solution (3.6 g/l NaCl, 1.96 g/l $CuSO_4 \cdot 5H_2O$) with relative permittivity ε_r=78 and conductivity σ=0.8 S/m. The fabricated coil with dielectric liner surrounding the phantom is shown in **Figure 2.9**.

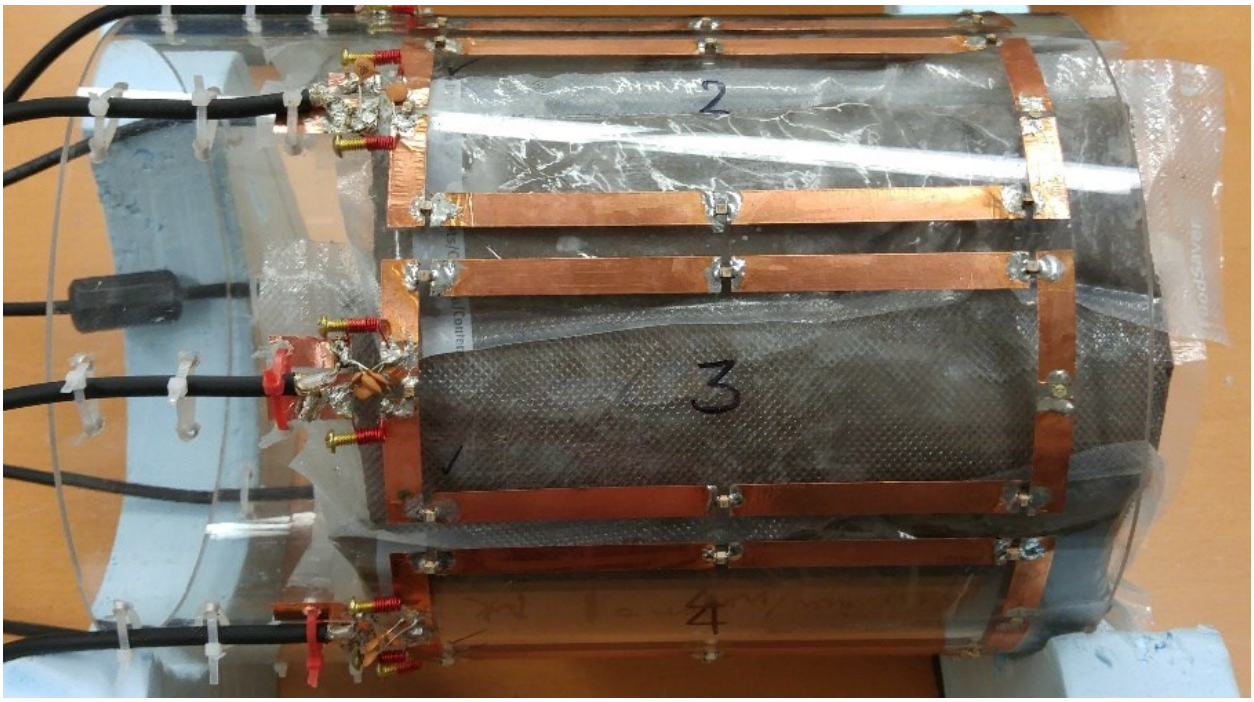

Figure 2.9. Fabricated array with dielectric liner and phantom.

2.3.4 Bench measurement

Bench measurement set up is shown in **Figure 2.10**. Scattering parameters of the array are measured using an Agilent 4395A vector network analyzer. The 8 cables are kept as straight and parallel as possible using foam spacers and connected to the grounding plate as described above. The unused channels are terminated with 50 Ω loads.

Figure 2.11 shows the measured (a) and simulated (b) return loss (S_{11}) for each liner over the frequency range between 170 and 230 MHz. Besides some frequency splitting due to coupling the optimal liner improves matching as predicted by the simulations.

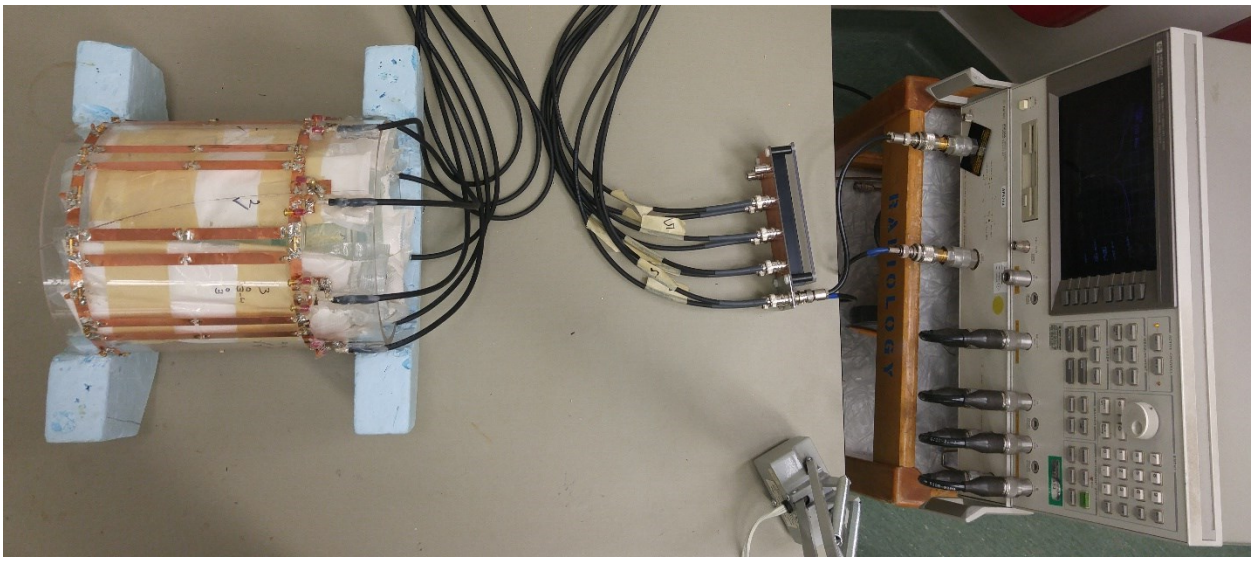

Figure 2.10. Bench measurement set-up.

2.3.5 Scan

The simulation results were verified by acquiring images on a 4.7 T whole-body system with a 4-channel Unity Inova console (Varian, Palo Alto, CA). Single channel flip angle maps were acquired with one channel transmitting and receiving, while three other channels were receiving the signal (**Figure 2.12**). The unused four channels were terminated with 50 Ω loads. The $\mathbf{B}_1^+$ field distribution with the four liners was measured with the gradient-echo double-angle technique [22] using a 5 ms Gaussian excitation pulse and nominal flip angles of 45° and 90°. In this method the ratio of the intensity of the signal at 90° over double the ratio of the signal at 45° are calculated and then converted to flip angle map ($\alpha(x) = arccos\frac{I_2(x)}{2\,I_1(x)}$) [22]. The acquisition parameters for these multi-slice scans are: echo time TE=7 ms, pulse repetition time TR=1000 ms, 9 slices, FOV of 192 × 192 × 180 mm and resolution of 1 × 1 × 8 mm. For each liner, the transmit power was adjusted to achieve the same nominal flip angle in an ROI near the transmitting coil. The transmitter gain settings were recorded and the corresponding sensitivities were compared relative to that in absence of a liner (air).

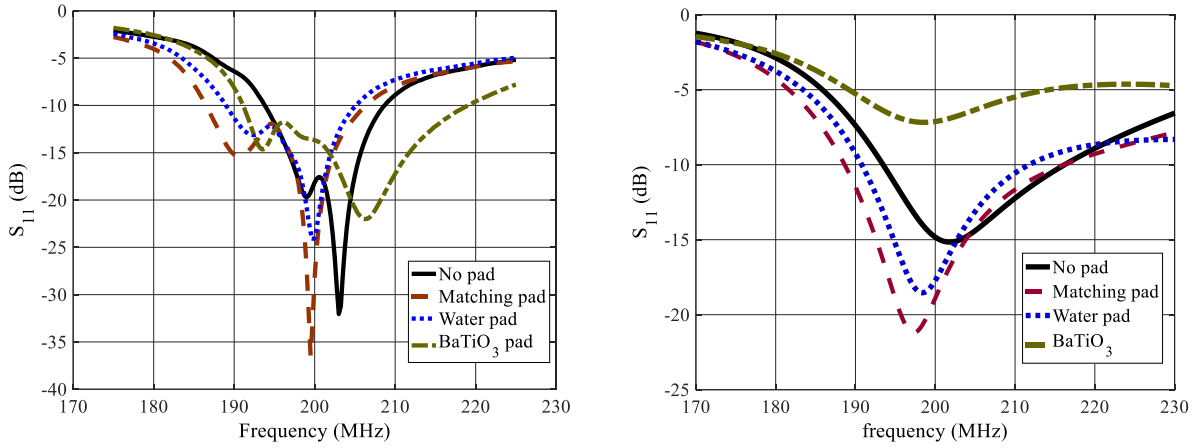

Figure 2.11. S_{11} (a) measured on the bench, and (b) simulation for each case.

The flip angle maps acquired when channel one is transmitting (**Figure 2.13**, bottom row) show that the matched permittivity liner results in the smallest coupling to neighboring elements. Comparison of simulation and measurement show broad agreement, with differences likely arising from the omission of some practical details from the simulation to avoid introducing excessive computational burden. Specifically, the simulation ignores coupling due to cables and ground connections as well as the effects of matching circuits.

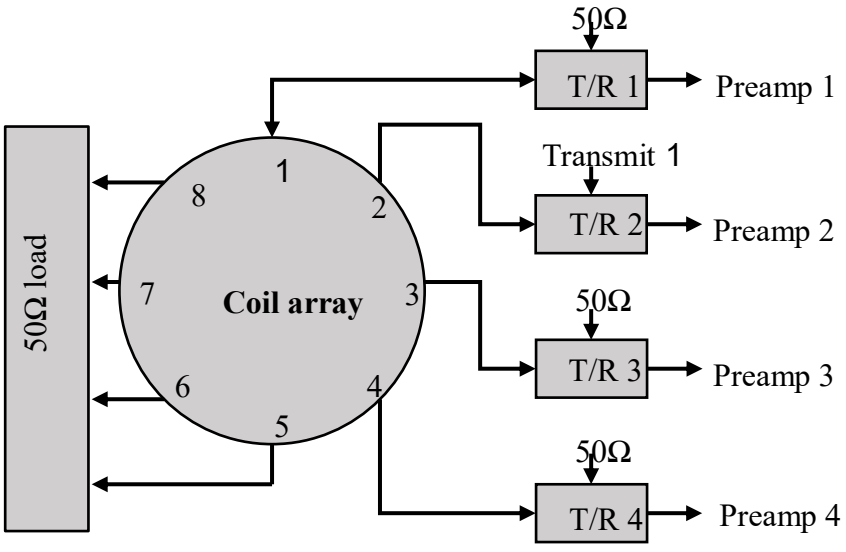

Figure 2.12. Coil array set-up for imaging

The relative transmitter gains obtained during flip angle calibration is shown **Table 2.4**. We note that sensitivity is progressively degraded with liner permittivities above ε_r =17.5 (also seen in **Table 2.2**).

Table 2.4. The required transmit gain to achieve a given flip angle.

	ε_r=1	ε_r =17.5	ε_r =78	ε_r =150
Gain required for the same flip angle	29.46 dB	30.46 dB	31.46 dB	33.46 dB

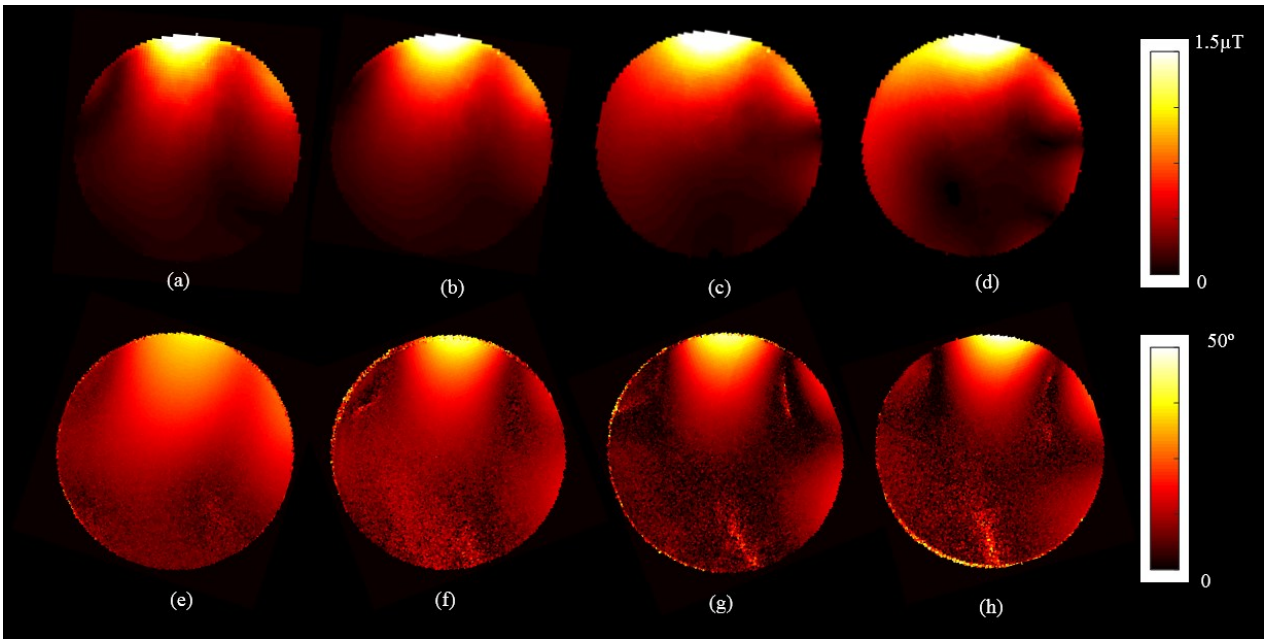

Figure 2.13. Comparison of simulated fields (top row) from a single element and fields measured using the double-angle method (bottom row). Liner permittivities: ε_r = 1 (a, e), ε_r = 17.5 (b, f), ε_r = 78 (c, g) and ε_r = 150 (d, h).

2.4. Discussion

Dielectric pads have been used to increase the magnetic field locally and also to increase the homogeneity of magnetic field when used as liners. The use of high permittivity pads (ε_r > 100) has been increasing in the literature. This work investigates the effects of the permittivity of an annular dielectric liner between an array and phantom in terms of electromagnetic fields and sensitivities. To do so, a range of permittivities are chosen for the liners ranging from 35 to 150

(HDC layer). These permittivities are chosen based on the current liners in the literature. It was found that high permittivities ($\varepsilon_r > 100$) used in similar applications in the literature give rise to liners with resonant frequencies that are dangerously close to the Larmor frequency. Such liners also introduce undesired phase shifts, inhomogeneities, and SAR concentrations in the longitudinal direction. Moreover, HDC liners increase the mutual impedance (both real and imaginary parts) significantly. Hence coupling using these liners must be investigated.

In this chapter the permittivity of the liner is designed to minimize the electromagnetic field reflections at dielectric boundaries, i.e., by choosing an intermediate intrinsic impedance equal to the geometric mean of that of the former and phantom. The matched liner with permittivity of 17.5 is compared with the high-permittivity liners in terms of transmit performance, homogeneity, coupling and also the resonance frequency of the annular liner.

The results show that the homogeneity of the magnetic field in the transverse plane is improved using HDC liners, but it is significantly degraded in the longitudinal direction. Furthermore, the use of HDC liner degrades the transmit performance of the array compared to the case where the matched liner is used.

The effect of matched liner on the transmit performance of the coil is minimal while the homogeneity of magnetic field is enhanced. The optimal permittivity liner minimizes coupling between elements (in the presence of matching circuits) while keeping the liner's dielectric resonance frequency at a safe distance of at least one octave from the Larmor frequency.

In practical applications there will be some air-gap between the phantom and the liner. This scenario is investigated and it is found that the existence of a thin air-gap will have minimal effect on the array performance.

2.5. Conclusion

Dielectric liners are used to increase the homogeneity of the magnetic field. In this chapter, it was found that in choosing a liner's permittivity a compromise should be made between desired improvements in magnetic field homogeneity in transverse plane and unwanted degradation in transmit efficiency. Unlike local pads, which are used to increase the signal locally, high permittivities will degrade the performance of the array when used as liners.

Chapter 3

Control of Mutual Coupling in High-Field MRI Transmit Array in Presence of High Permittivity Liners[3]

3.1. Introduction

One of the most important challenges to implementing transmit arrays is mutual coupling. The proximity of the elements in an array determines the mutual impedance between them through which signal and noise can transfer. Additionally, when an array is loaded with the lossy human body, elements will have common current paths through the sample which result in a mutual resistance and noise correlation [71], [72]. Mutual impedance between elements is increased when high dielectric constant pads are used [73] and thus one of the goals of this chapter is to explore whether the enhanced interaction can be suppressed with practical methods.

Coupling is more difficult to manage at higher frequencies and strongly affects the field maps of individual elements. Having distinct field maps for each element is a requirement for parallel transmit techniques such as transmit SENSE [45]. Therefore, it is reasonable to require high isolation (>30 dB) between adjacent elements to avoid significant overlap in the sensitivity patterns. Coupling also affects the transmit efficiency of the array [74], because power coupled between ports returns down the transmit path and is dissipated to protect the power amplifiers. The minimum isolation required between all pairs of elements to achieve a given efficiency depends on the specific excitation method and settings (e.g., RF shimming settings, transmit SENSE pulse shapes) [74]. Nevertheless, because the array elements are tuned resonators, in practice it is desirable to achieve a minimum of 15–20 dB isolation to avoid detuning effects.

[3] This chapter is published as: A. Kordzadeh; N. De Zanche, "Control of Mutual Coupling in High-Field MRI Transmit Arrays in the Presence of High-Permittivity Liners," in IEEE Transactions on Microwave Theory and Techniques , vol.PP, no.99, pp.1-7
doi: 10.1109/TMTT.2017.2668406

3.1.1. Review of literature

Different techniques have been used to decouple the elements in a phased array coil [71], [72], [75], [76], [77], [78], [79] where most of them aim to remove mutual reactance as the most significant term in the mutual impedance. The simplest method to remove mutual inductance is to overlap adjacent loops in an array [72]. This method is very sensitive on the location of elements specially for three or more elements in the array [67]. Although this method effectively reduces coupling levels between adjacent elements, it is not optimal for parallel spatial encoding where the elements' sensitivity patterns should have minimal overlap and be distinct from each other [80].

Therefore in receive-only arrays, low-input impedance (reflective) preamplifiers are used to further reduce inductive coupling between non adjacent elements by blocking currents on the array elements [72]. However, this technique is not practical in transmit mode due to the lack of powerful high-output-impedance amplifiers [81].

More recently magnetic walls, implemented using metamaterials, have been used to isolate adjacent elements by suppressing the common fields between elements. This technique yields approximately 22 dB isolation between neighboring channels at 7 T, however reduces transmit efficiency of the array [82], [83].

Numerous methods employing capacitors and inductors between elements have also been devised to remove mutual inductance. This technique usually works for adjacent neighbors [84], [78] however some configurations have been devised to reduce mutual coupling for non-immediate neighbors as in [77]. Capacitive networks are more popular decoupling circuits due to higher quality factors than inductive circuits, resulting in higher SNR [77].

Until recently, the resistive term of the mutual impedance was simply ignored or believed to be impossible to remove [85]. It is shown that mutual resistance is significant in presence of the phantom/subject. Recently-developed methods to eliminate the mutual resistance in arrays are investigated in [71] and [76]. Authors in [71] use a resonant inductive network between coupled elements to minimize both mutual resistance and reactance while [76] employ a capacitive network for decoupling the elements in a receive array.

While results in [76] imply that removing mutual resistance will not compromise SNR it is expected that eliminating mutual resistance in transmit arrays will be beneficial where high-output-impedance power amplifier decoupling cannot be used [76].

3.1.2. Scope of this chapter

This chapter describes an eight-channel transmit/receive array of loops for 4.7 T. A high dielectric constant (HDC) liner is inserted between the coil array and the phantom to improve magnetic field homogeneity inside the region of interest [86]. As a result, mutual coupling is significantly enhanced between elements. Hence mutual impedance (resistive and reactive) between adjacent elements is eliminated by using capacitor bridges and the effect of decoupling on transmit parameters such as $\mathbf{B}_1^+$ field pattern and SAR are investigated. For comparison, each term of the mutual impedance is removed individually as well as concomitantly, and results are compared to the coupled case in terms of transmit and safety efficiency [86]. Moreover, the array is fabricated and tested on bench. It is then used to image a head phantom in the scanner and results are compared to simulation to verify the concepts. The first section of this chapter, investigates the theory behind coupling and mutual impedance in presence of dielectric liner and capacitive decoupling. The next section is methods which includes the design and simulation of the structure as well as the results. Fabrication and measurement results are included in this section as well.

3.2. Theory

3.2.1. Mutual coupling

Two resonant elements, when placed side by side will share electric and magnetic fields. In general coupling coefficient, k, is defined as the ratio of coupled energy to the stored energy given by **(3.1)** [87].

$$k = \frac{\iiint \varepsilon \boldsymbol{E}_1 . \boldsymbol{E}_2 \, dv}{\sqrt{\iiint \varepsilon |\boldsymbol{E}_1|^2 \, dv \times \iiint \varepsilon |\boldsymbol{E}_2|^2 \, dv}} + \frac{\iiint \mu \boldsymbol{H}_1 . \boldsymbol{H}_2 \, dv}{\sqrt{\iiint \mu |\boldsymbol{H}_1|^2 \, dv \times \iiint \mu |\boldsymbol{H}_2|^2 \, dv}} \tag{3.1}$$

Where $\boldsymbol{E}$ and $\boldsymbol{H}$ are the electric and magnetic fields generated by each resonator and ε and μ are the permittivity and permeability of the media respectively. Electric coupling (first term in **(3.1)**)

is generated as a result of interaction between electric fields while magnetic coupling (second term in **(3.1)**) is generated as results of magnetic fields interactions. Coupling coefficient can be either positive or negative implying that coupling reduces or enhances the energy stored in the resonators [87].

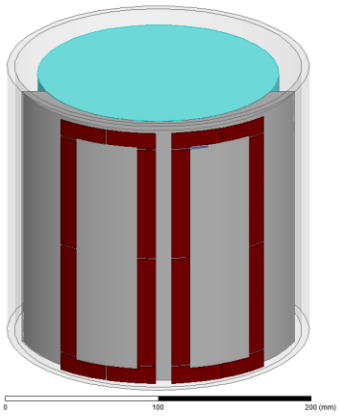

Figure 3.1. Two loops in presence of dielectric liner and phantom.

Consider two loops placed in proximity of a dielectric liner as well as the phantom as shown in **Figure 3.1**. The elements in this configuration would share both electric and magnetic fields hence the elements will experience mixed coupling. As a result of coupling, resonant frequency is split to f_e and f_m as shown by (3.2**)** and (3.3) [87].

$$f_e = \frac{1}{2\pi\sqrt{(L - L'_m)(C - C'_m)}} \tag{3.2}$$

$$f_m = \frac{1}{2\pi\sqrt{(L + L'_m)(C + C'_m)}} \tag{3.3}$$

Where C and L are self-capacitance and inductance of each loop and C'_m and L'_m are mutual capacitance and inductance, respectively. Mixed coupling is a superposition of electric and magnetic coupling, hence they can either enhance or cancel each other [87].

3.2.2. Mutual impedance in presence of dielectric liners

Mutual impedance, Z_{12}, is a complex quantity with a real part, R_{12}, and the imaginary part, X_{12}, through which signal and noise transfer between coupled elements. To explain the effect of

dielectric liners on the mutual impedance, we must examine Ampere's law with Maxwell's correction in a conductive medium (3.4),

$$\nabla \times \boldsymbol{H} = \boldsymbol{J}_D + \boldsymbol{J}_C = j\omega\varepsilon\boldsymbol{E} + \sigma\boldsymbol{E} \tag{3.4}$$

Where $\boldsymbol{H}$ is the magnetic field (A/m), $\boldsymbol{E}$ is the electric field (V/m), ω is the angular frequency, $\boldsymbol{J}_D$ is the displacement current density and $\boldsymbol{J}_C$ is conduction current density (A/m^2). Displacement current density depends on the frequency as well as permittivity. Using an HDC liner with high permittivity (>100) will create a significant displacement current density which acts as a secondary source to generate additional magnetic fields [56]. The higher the permittivity of the liner, the stronger the electric/magnetic field generated in the region adjacent to it.

Mutual impedance can be calculated using reaction theory [68] from the electromagnetic fields produced by exciting each element. The interaction of two fields i and j, $\langle i, j \rangle$, excited by current sources is defined as [68].

$$< i,j >= \int \boldsymbol{E}^i . I^j d\boldsymbol{l} = I^j \int \boldsymbol{E}^i . d\boldsymbol{l} = -V^i I^j \tag{3.5}$$

Where $\boldsymbol{E}^j$ is the electric field generated by the current I^jon coil j, and V^i is the voltage at the ports of coil *i*. The mutual impedance between elements *i* and *j* is then: [68], [67]

$$Z_{ij} = -\frac{< j,i >}{I_i I_j} \tag{3.6}$$

$$Z_{ij} = \frac{-1}{I_i I_j}\left\{\iiint_{phantom} \boldsymbol{E}^j(r).\boldsymbol{J}_p^i(r)dv + \iiint_{liner} \boldsymbol{E}^j(r).\boldsymbol{J}_p^i(r)dv + \iiint_{coil} \boldsymbol{E}^j(r).\boldsymbol{J}_c^i(r)dv\right\} \tag{3.7}$$

The term $\boldsymbol{J}^i{}_c(r)$ refers to the current density on coil i and $\boldsymbol{J}^i{}_p(r)$ is the current density generated in the phantom and HDC liner. In fact $\boldsymbol{J}_p^i$ is the current density in the phantom which is induced by the fields generated by coil i [67]. The displacement current term due to the presence of the HDC liner cannot be ignored and the mutual impedance will be expanded to

$$Z_{ij} = \frac{-1}{I_i I_j}\left\{\iiint_{phantom} \sigma_p \boldsymbol{E}^j(r).\boldsymbol{E}^i(r)dv + \iiint_{liner} j\omega\varepsilon \boldsymbol{E}^j(r).\boldsymbol{E}^i(r)dv + \iiint_{coil} \boldsymbol{E}^j(r).\boldsymbol{J}_c^i(r)dv\right\} \tag{3.8}$$

Here ε is the permittivity of the phantom or liner, and σ_p is the phantom's conductivity.

Consider two rectangular loops conformed to a cylindrical phantom and corresponding high permittivity liner as shown in **Figure 3.1**. Using full wave simulation software (HFSS V.15, Ansys Corp., Canonsburg, PA), mutual impedance between two adjacent loops on the cylinder is plotted for the case without and in presence of the dielectric liner in **Figure 3.2**. As can be seen at 200 MHz both terms of the mutual impedance have significantly increased with the HDC liner present which is in consistent with the above equations for mutual impedance.

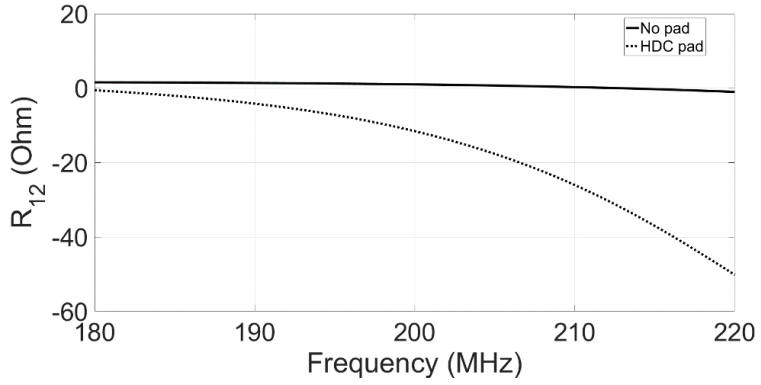

(a)

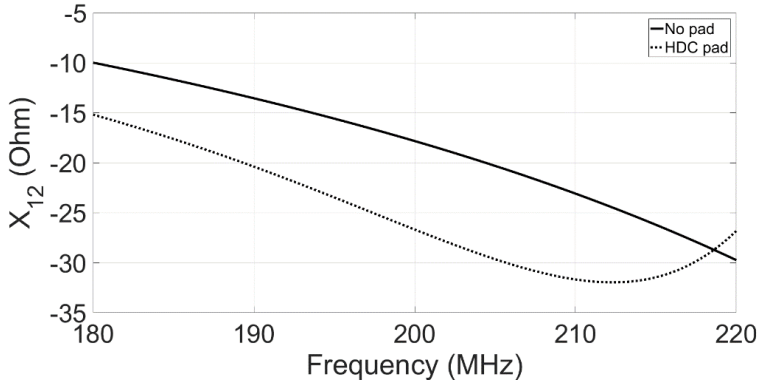

(b)

Figure 3.2. (a) Mutual resistance, (b) mutual reactance between two loops in presence of high permittivity liner and phantom.

3.2.3. Capacitive decoupling

To remove mutual impedance between adjacent elements, capacitive bridges are connected between the elements, thus introducing a third current loop [76]. The circuit model of two loops with capacitive decoupling is shown in **Figure 3.3**. The current in the third loop is controlled with capacitors C_{t2} and C_d, and their spacing, d. Circuit mesh equations are as follows:

$$\begin{bmatrix} j\omega L + \frac{5}{j\omega C_{t1}} + \frac{2}{j\omega C_{t2}} + R_1 & \frac{-1}{j\omega C_{t2}} & j\omega M + R_{12} \\ \frac{-1}{j\omega C_{t2}} & \frac{2}{j\omega C_d} + \frac{2}{j\omega C_{t2}} + R_3 & \frac{-1}{j\omega C_{t2}} \\ j\omega M + R_{12} & \frac{-1}{j\omega C_{t2}} & j\omega L + \frac{5}{j\omega C_{t1}} + \frac{2}{j\omega C_{t2}} + R_1 \end{bmatrix} \times \begin{bmatrix} i1 \\ i3 \\ i2 \end{bmatrix} = \begin{bmatrix} v1 \\ 0 \\ v2 \end{bmatrix} \quad (3.9)$$

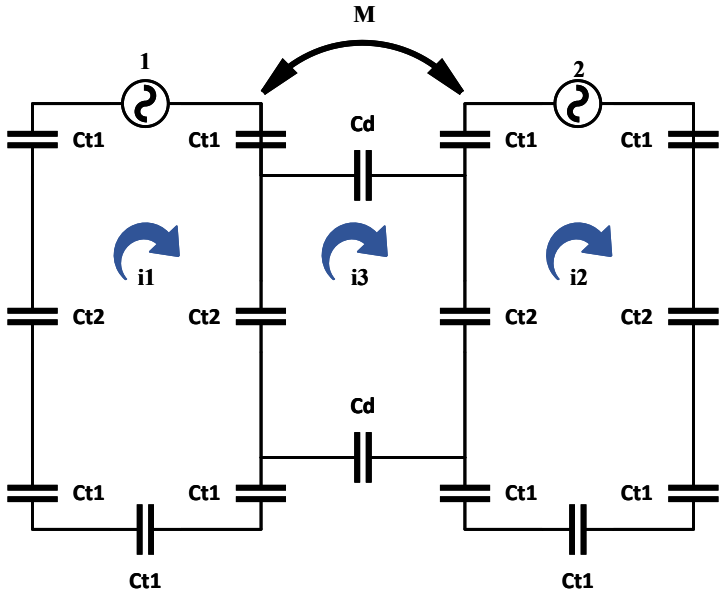

Figure 3.3. Capacitive decoupling for two element array.

Here M is the mutual inductance and R_1 and R_3 refer to the self-resistances of the main loops and decoupling loop, respectively. The mutual resistance and reactance between the two ports simplify to:

$$\text{Real}\,(Z_{12}) = R_{12} + \frac{R_3\omega^2 C_{t2}^2}{R_3^2\omega^4 C_{t2}^4 + 4\omega^2(C_{t2} + {C_{t2}^2}/{C_d})^2} \tag{3.10}$$

$$\text{Imaginary}\,(Z_{12}) = \omega M + \frac{2\omega(C_{t2} + {C_{t2}^2}/{C_d})}{R_3^2\omega^4 C_{t2}^4 + 4\omega^2(C_{t2}^2 + {C_{t2}^2}/{C_d})^2} \tag{3.11}$$

Both real and imaginary parts of mutual impedance depend on the values for the capacitors, C_{t2} and C_d as well as the location of the decoupling capacitor. To set both real and imaginary terms to zero simultaneously, one should find appropriate values for these parameters.

3.3. Methods

3.3. Design and simulation

The current structure is designed to image pediatric head or extremities. A lossy phantom with relative dielectric constant $\varepsilon_r = 76$ and conductivity of $\sigma = 0.8\,S/m$ is used to mimic the dielectric properties of brain. The phantom has the outer diameter of 150 mm and its height is 180 mm. An HDC liner with permittivity $\varepsilon_r = 150$ and thickness of 2 cm surrounds the phantom to maximize the homogeneity of the magnetic field in the phantom. To cover the FOV, the coil array consists of eight loops conformed to a PMMA cylindrical former. The structure is shown in **Figure 3.4**.

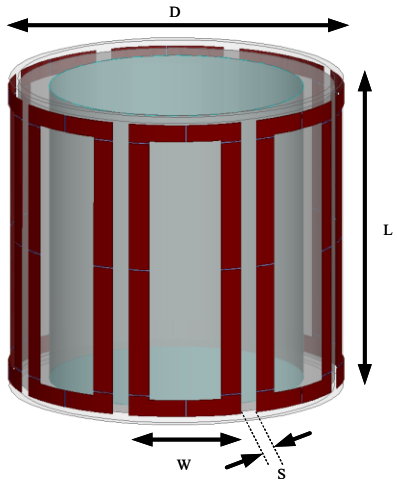

Figure 3.4. Designed 8 channel array in presence of liner and phantom.

Each element in the array is a rectangular loop and capacitors are designed to make the elements resonate at 200.4 MHz which is the Larmor frequency for ^{1}H at 4.7T. These capacitors are distributed along the coil to guarantee a uniform current distribution on the coil. Designed dimensions of the structure are organized in **Table 3.1**.

Table 3.1. Designed dimensions of the structure.

D	L	W	S
200mm	180mm	69mm	10mm

The arrangement of tuning capacitors (C_{t1} and C_{t2}) as well as decoupling capacitors for each element is shown in **Figure 3.5**.

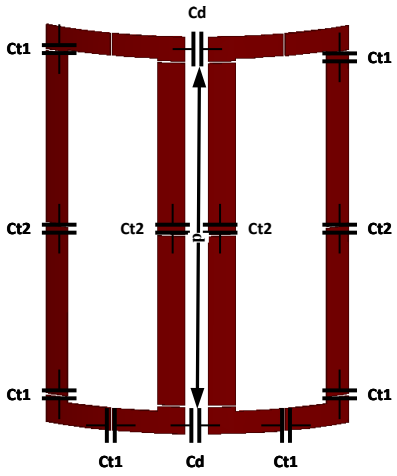

Figure 3.5. Capacitor arrangement for each element.

As described in the theory section, to remove the mutual impedance, appropriate values for C_{t2} and C_d must be found along with the separation, d, which directly influences R_3. A few parameter sweeps are done in HFSS around an initial estimate to find the desired values. Four cases are considered for comparison: no decoupling (coupled), zero mutual resistance (R_{12}=0), zero mutual reactance (X_{12}=0) and zero mutual impedance (Z_{12}=0). Design parameters are listed in **Table 3.2**.

Table 3.2. Designed values for tuning and decoupling capacitors as well as their locations.

	C_{t1} (pF)	C_{t2} (pF)	C_d (pF)	d (mm)
Coupled	15	15	-	-
R_{12}=0	14	10	470	25
X_{12}=0	10	10	460	30
Z_{12}=0	18	10	12	80

Full wave simulation of the whole structure in HFSS V.15 (Ansys) is done and the appropriate data (**H** field and SAR) are extracted to MATLAB for post processing.

The $\mathbf{B}_1^+$ field is plotted along the diameter of the phantom on a central transverse plane in **Figure 3.6**, showing that the liner reduced the difference between fields at the center versus the peripheral regions of the phantom.

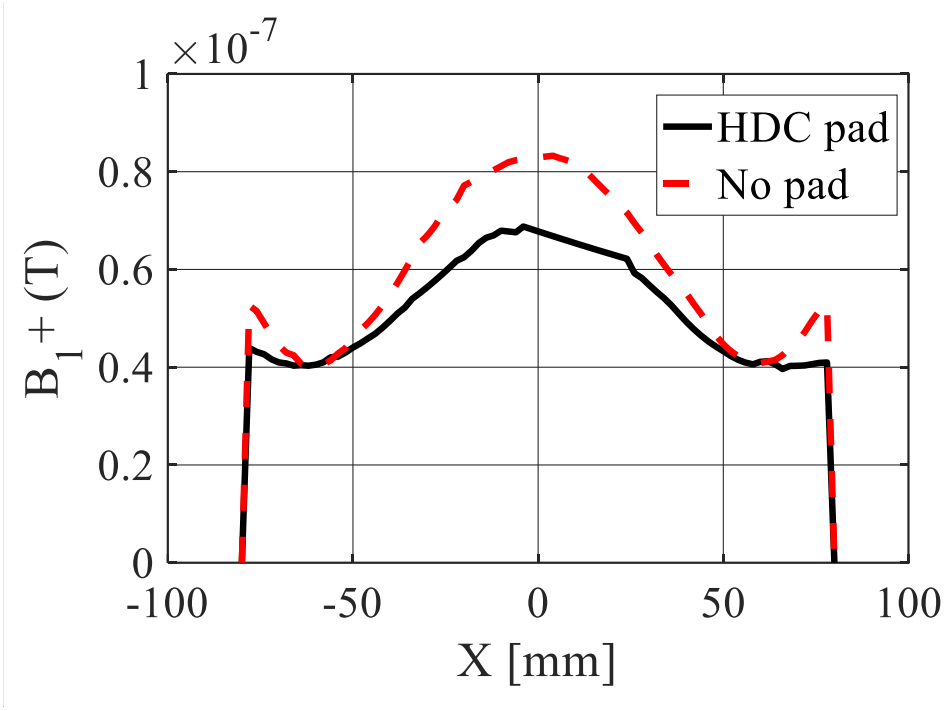

Figure 3.6. $\mathbf{B}_1^+$ field versus radius plotted in transverse plane in the phantom for coupled coil in presence and without HDC liner.

However, the drawback of using the HDC liner is the increase in mutual impedance, especially between non-adjacent elements. **Figure 3.7** shows the full scattering matrices for the unlined array as well as for each decoupling case of the lined array, all normalized by matching so that

elements on the diagonals are zeros. Removing both terms of the mutual impedance achieves isolation that is better than that obtained when mutual resistance or reactance are removed individually.

The simulation results such as average $\mathbf{B}_1^+$ field as well as SAR and transmit efficiencies are post processed and are shown in **Table 3.3**. As can be seen from **Table 3.3**, Removing both terms of mutual impedance reduces nearest-neighbor coupling to -32 dB and other terms to -18 dB or better, thus meeting the requirements set forth in the Introduction (30 and 15 dB, respectively). The decoupling level achieved for each case is shown in **Table 3.3**. By removing only one term of the mutual impedance, nearest-neighbor isolation is limited to 27 dB. In quadrature excitation, the average $\mathbf{B}_1^+$ field magnitude increases with full decoupling along with the $\mathbf{B}_1^+$ field at the center of the phantom. The maximum SAR and average SAR also increase due to the currents in the additional loops created by the insertion of capacitors between the main loops. We note that decoupling has very limited influence on transmit efficiencies, with a slight reduction in safety efficiency in the fully decoupled case due to increased SAR.

Table 3.3. Summary of simulation results.

	Coupled	**R_{12}=0**	**X_{12}=0**	**Z_{12}=0**
Nearest neighbor coupling (dB)	-9.4	-24	-27	-32
Max non-neighbor coupling (dB)	-19	-14	-18	-18
Averaged B_1^+ (nT)	34	34	34.9	39.8
Center B_1^+ (nT)	68.3	64.8	66.5	70.4
Maximum SAR (mW/Kg)	7.3	11	11.9	13.1
Average SAR (mW/Kg)	1.9	2.8	3	3
Deposited power (mW)	7	10.2	10.7	10.8
B_1^+(Avg.)/√Pv (μT/√W)	0.406	0.336	0.337	0.383
B_1^+(Avg.)/√(SAR(Max)) (μT/√(W/kg))	0.398	0.324	0.320	0.347

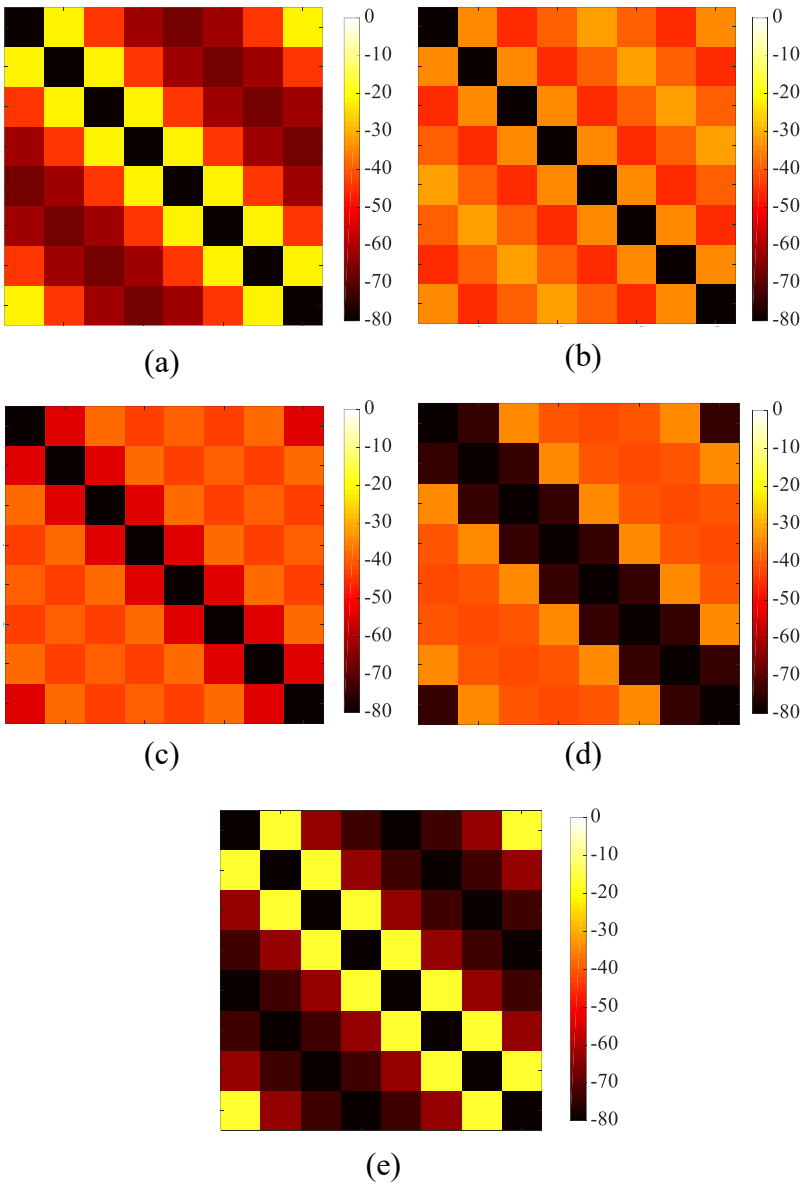

Figure 3.7. *S* matrix magnitude (dB) with liner present for (a) coupled, (b) R_{12}=0, (c) X_{12}=0, (d) Z_{12}=0, and (e) coupled without liner.

Using simulation data for electric and magnetic fields, $\mathbf{B}_1^+$ field and SAR patterns are plotted in a transverse slice through the center of the phantom (**Figure 3.8**). While the magnetic field patterns remain very similar, SAR increases especially in the peripheral regions of the phantom as a result of currents through the decoupling capacitors.

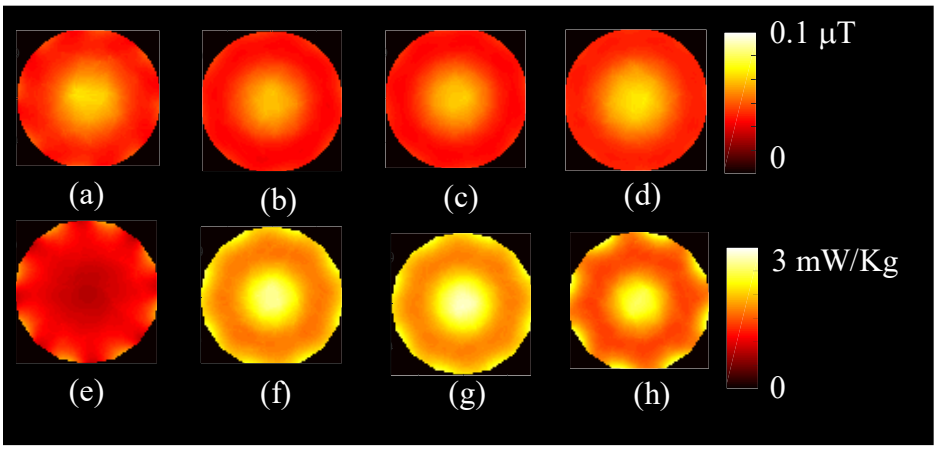

Figure 3.8. Simulated $\mathbf{B}_1^+$ field pattern for (a) coupled, (b) R_{12}=0, (c) X_{12}=0, (d) Z_{12}=0. SAR field pattern for (e) coupled, (f) R_{12}=0, (g) X_{12}=0, (h) Z_{12}=0, each channel is excited with 1 A current excitation.

3.4. Fabrication

The array is fabricated using adhesive copper tape attached to the cylindrical PMMA former (**Figure 3.9** (a)). Each element is fine-tuned and matched to 50Ω using a 12 pF trimmer capacitor and a lattice matching balun, respectively. Coupling between adjacent elements is also adjusted using trimmer capacitors located as shown in **Figure 3.9** (b).

The cylindrical phantom contains a solution (3.6 g/ℓ NaCl, 1.96 g/ℓ $CuSO_4.5H_2O$) with the same permittivity and conductivity as in the simulation. High permittivity pads to surround the phantom are made using $BaTiO_3$ suspension in deionized water with volume ratio of 3/7 (V_{BaTiO3}/V_{water}) to achieve a permittivity of 150 [73]. Keysight 85070E Dielectric Probe was used to measure the permittivity of the suspension. The suspension was subsequently packaged in ~5-cm-wide heat-sealable bags (layered polyethylene and polyamide film) to prevent spills and to facilitate arrangement around the phantom.

3.5. Bench measurements

The experiment set-up is shown in **Figure 3.10**. The structure is supported by foam holders and cables are grounded using a common bulk head plate. Scattering parameters of the array are measured near 200 MHz using an Agilent 4395A VNA in presence of dielectric liner and the phantom as shown in **Figure 3.11**. As can be seen in **Figure 3.11** (a), S_{11} is kept below -20 dB

for both cases. On the other hand, S_{12} shown in **Figure 3.11** (b), has been reduced to almost -32 dB in the decoupled case which is consistent with the simulation results.

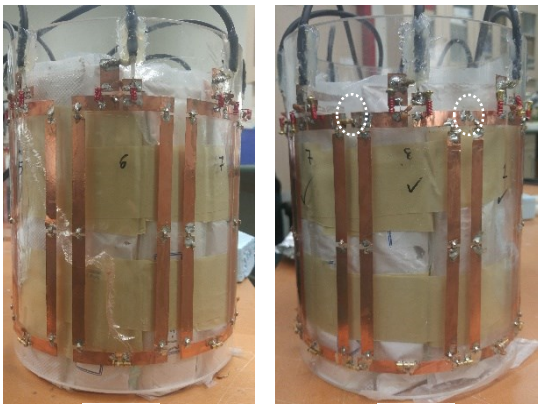

(a) (b)

Figure 3.9. Fabricated arrays (a) coupled (b) decoupled. Decoupling bridges are highlighted by ellipses.

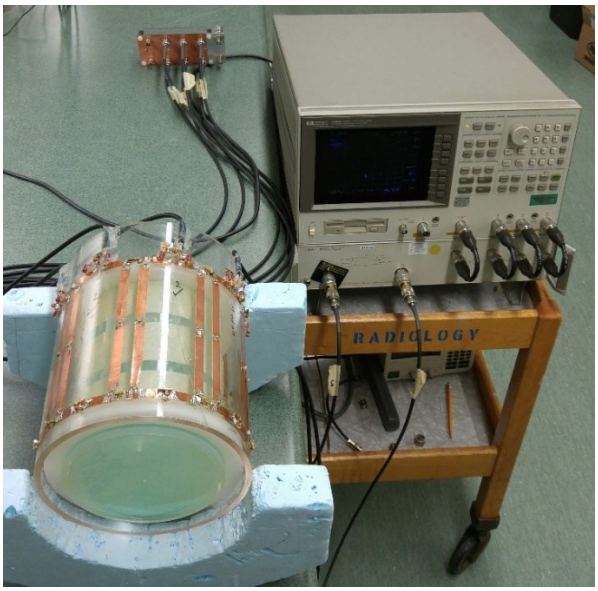

Figure 3.10. Experiment set-up including coil array, VNA and phantom.

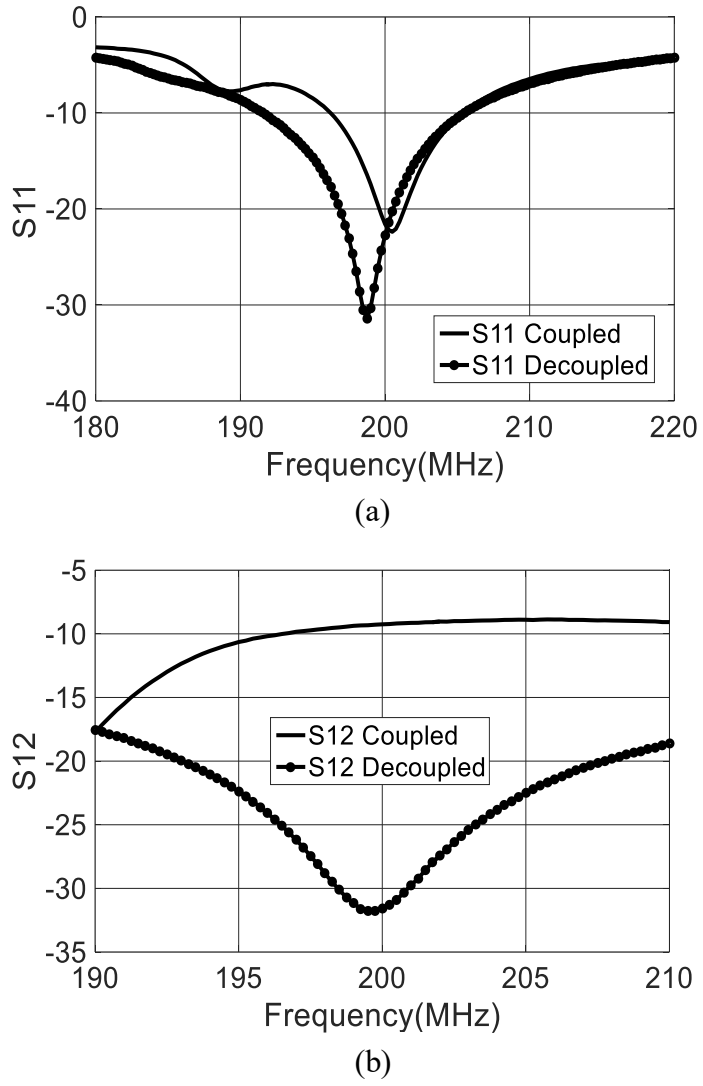

Figure 3.11. Measured (a) $|S_{11}|$ and (b) $|S_{12}|$ (in dB) comparison for coupled and decoupled case with the HDC liner.

3.6. Scan

To verify the simulations, $\mathbf{B}_1^+$ field is measured in the two experimental configurations (coupled and fully decoupled) using the double-angle technique [22] where two gradient-echo image acquisitions with nominal flip angles (FA) of 45° and 90° are acquired and the resulting FA map is obtained from the ratio of the image magnitudes. The acquisition parameters are T_E=7 ms, T_R=1000 ms, 192 × 192 × 180 mm FOV and 1 × 1 × 8 mm resolution.

All images were acquired on a 4.7 T whole-body MRI system (Unity Inova; Varian, Palo Alto, California). Because of the availability of a single transmit channel and four receivers in the current scanner, each scan required two acquisitions transmitting with one element and receiving with four channels at a time. The connections for each setup are shown in Figure **3.12** in blue and red, respectively.

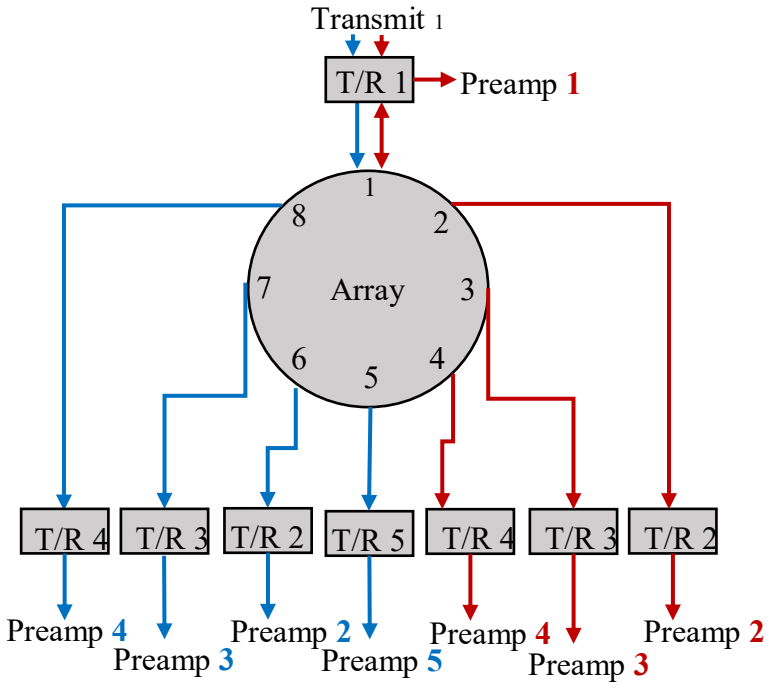

Figure 3.12. Coil array set-up for imaging (red and blue connections represent the set-up used for each subset of measurements).

Moreover, acquired flip angle (scaled $\mathbf{B}_1^+$) maps (**Figure 3.13** (e) and (f)) are compared to those of the simulation in **Figure 3.13** (a) and (b), confirming an improved distinction in the transmit field patterns and suppression of signal from neighboring elements.

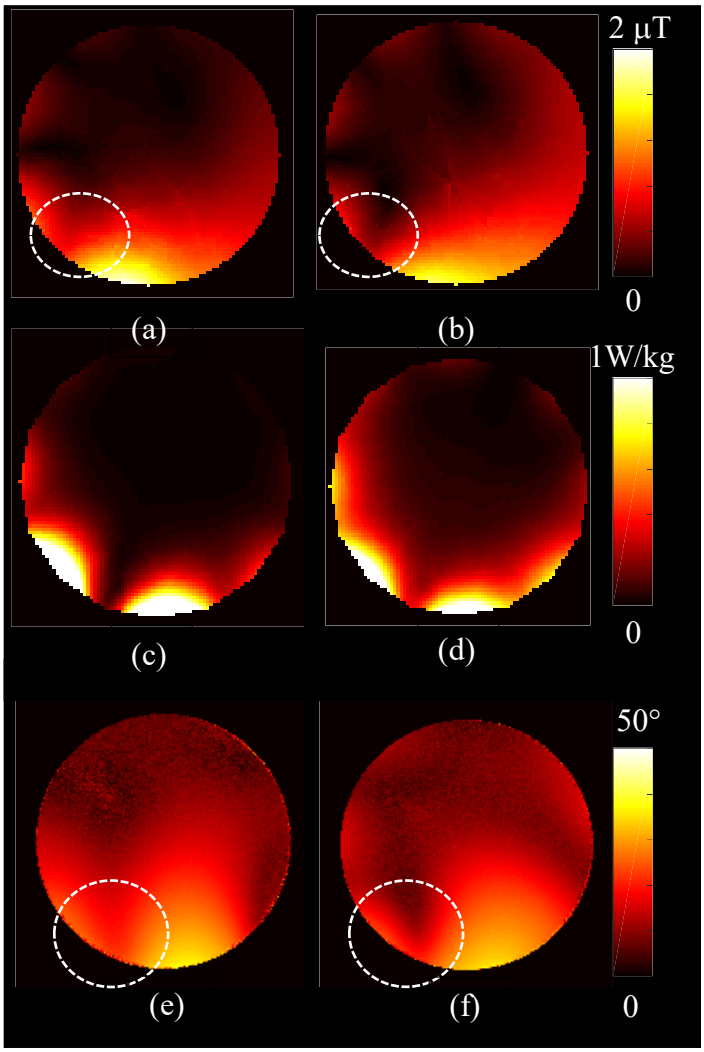

Figure 3.13. Simulated $\mathbf{B}_1^+$ field (0-2μT) for (a) coupled, (b) decoupled and SAR (0-1W/kg) for (c) coupled and (d) decoupled coil when one channel is excited, and measured flip angle (0-50º) or B_1^+ maps for (e) coupled, (f) decoupled coil.

3.4. Discussion

This chapter investigates the mutual coupling between elements in an array in presence of HDC liners and phantom using reaction theory. Both real and imaginary parts of mutual impedance is shown to significantly increase as displacement current density is enhanced by the HDC liner.

Mutual impedance is considered to be mainly comprised of mutual reactance however at higher frequencies and in proximity of high permittivivties, mutual resistance grows significantly. Here

mutual resistance and reactance are nearly eliminated simultaneously by using capacitive bridges.

Full wave simulations and post processing are performed to compare the transmit performance of the array with decoupling. Decoupling levels up to -32 dB are achieved by removing both terms of mutual impedance at the same time.

The array performance is also investigated and compared when each term of mutual impedance is removed at a time. The transmit efficiency of the array is unchanged by decoupling the elements. However, the safety efficiency is slightly degraded. This is a result of introducing new capacitors (decoupling capacitors) hence increasing the local electric fields between elements.

The array is then fabricated and measured on the bench. Capacitive bridges are used between elements and are trimmed to achieve decoupling between each pair of elements in the array. Bench measurements verify the simulation results. The array is also used to image a phantom and it is shown that distinct field maps for each element can be produced with high isolations.

3.5. Conclusion

In this chapter, we investigate the effects of high-permittivity liners and various levels of decoupling on the transmit characteristics of an eight-channel array for imaging the extremities or pediatric brain at 4.7 T. The liner improves field homogeneity but also increases mutual impedance between elements. This coupling can be reduced to acceptable levels without degrading the transmit performance or field uniformity of the array by removing both resistive and reactive terms of the mutual impedance using capacitive bridges. For each element, a distinct field map can therefore be produced as required for parallel transmit techniques (e.g., Transmit SENSE). These methods of array design can be extended readily to larger dimensions or greater numbers of elements.

Chapter 4
The TEM Horn: A New Array Element for High-field MRI[4]

4.1. Introduction

High field magnetic resonance imaging (>3 T) has proven significant advantages over standard field strengths for a number of reasons including higher signal to noise ratio (SNR) which facilitates acquiring images with enhanced spatial and temporal resolutions [88]. Other than the promising results for brain imaging, cardiac imaging [89], prostate imaging [90] and renal imaging [91] have benefited from high field strengths. Given the continuing trend of increasing the field strength, the radio frequency (RF) coils which are responsible for transmitting and receiving $\mathbf{B}_1$ fields should be developed accordingly in order to address the challenges associated with high field imaging. With increasing the field strength, the Larmor frequency increases and as a result the RF wavelength decreases. This is even more significant in presence of biological tissue as it has a high permittivity, ε_r, which reduces the wavelength accordingly ($\lambda = {}^{\lambda_0}/_{\varepsilon_r}$). Consequently, the wavelength becomes comparable or smaller than the size of the body, and the RF fields experience destructive/constructive interference resulting in dark/bright areas in the image, respectively. This issue is the main bottleneck for body imaging at high fields [88], [18], [10]. The other challenge at high frequencies is the reduction in penetration depth (δ) of the RF fields. As the human body is a conductive medium (with conductivity σ), RF fields decay as they penetrate the body (RF penetration section). Hence the penetration depth is limited at high fields and imaging deep targets like the prostate and kidneys is challenging [10].

Joule heating in tissue, described by the specific absorption rate (SAR), is also frequency dependent, hence at high field strength higher values of SAR are expected and localized hot spots resulting from constructive interferences of the electric fields are very possible [18].

[4] A preliminary report of this work will be presented at the 25th annual meeting of the International Society for Magnetic Resonance in Medicine, program number 4415, Honolulu, HI, 2017.

The RF coil elements used at high frequencies have been significantly studied in the literature. Conventional RF coils such as loops fail to be efficient at high frequencies. Loops perform better at the surface but their performance degrades at higher depth [52]. Transverse electromagnetic (TEM) resonators, which are generally any transmission line that can support transverse electromagnetic field, have frequently been used in several works for head imaging [92], [93] and body imaging [94], [95] at high fields. Comparing TEM elements and dipole antenna for imaging at 10.5 T in [96] shows that dipole elements generate more homogeneous fields compared to TEM element.

The dipole antenna was introduced in high [97] and ultra-high field imaging [96] due to its advantages over conventional elements such as microstrip transmission lines, loops, and TEM resonators. Dipole antenna has been shown to provide advantages such as higher homogeneity of the fields and also deeper penetration at high fields versus loops [52]. Although loops perform efficiently for targets closer to the surface, dipoles perform better for deep targets. This is even more significant while working at high and ultrahigh fields due to the smaller RF wavelength. In order to have maximum fields at the center, the dipole antenna should have a length of $\lambda/2$. Dipole antenna is an omni-directional antenna meaning that it will generate electromagnetic fields on its both sides hence it is not a directive element. Dipoles are therefore mounted on high permittivity substrates which magnify the fields on the high permittivity side and also shorten the length of the antenna as wavelength is reduced. Usually a very thick substrate is used to increase the intensity of the fields toward the patient [52]. Different modifications have been applied to dipole antenna in order to further shorten its length such as the fractionated dipole where segments are separated with capacitors/inductors [98].

The bow-tie antenna is also a modified dipole antenna with higher bandwidth and slightly shorter length. This antenna is mostly equivalent to the dipole in terms of performance. It is also designed as an RF applicator for hyperthermia which is at much higher frequencies (up to 600 MHz) due to the its deep penetration depth and ability to control the location of SAR hotspots [99]. The elements are immersed in deuterium oxide (D_2O) as a high permittivity substrate ($\approx$7 cm thick) to have smaller length and also to increase directivity [100]-[99].

This paper introduces a TEM horn antenna as an efficient element for high field imaging. The horn antenna, frequently used in high gain, directive applications in radar and communication systems [101], introduces promising results for imaging the body region at high fields. In the first section of this chapter the designed TEM horn antenna is outlined. For sake of comparison; a single horn antenna is compared with a dipole element at the same frequency, i.e. 200 MHz, for 4.7 T. Full wave simulations are performed and results show significant improvements in terms of transmit efficiency, penetration depth, SNR and SAR. Moreover, a two and three element array of horn antennas are simulated to investigate the array's performance for imaging a body-size phantom. The array is then fabricated and measured on the bench to verify the simulation results, and used in the scanner to image a body size phantom.

4.2. Methods

4.2.1. Design

The horn antenna is classified as an aperture antenna and the TEM (transverse electromagnetic) horn is a modification of this class of antennas to propagate TEM fields as it consists of two separate conductors [101]. By definition, the far field region boundaries depends on the wavelength and on the largest dimension of an antenna, *D*. [102].

$$r_{far\ field} > \frac{2D^2}{\lambda} \tag{4.1}$$

Therefore, in MRI we are working in the near field of an antenna and in this region the electromagnetic fields are bound to the antenna and changes in the load will affect its performance. Moving to higher frequencies will bring the far field of an antenna closer to it hence it is important to use appropriate structures that perform optimally at high fields.

The TEM horn is basically a shorted parallel plate transmission line with characteristic impedance of Z_c, which is then matched by a pyramidal structure to the impedance of the phantom, $Z_{phantom}$. In free space the length of the shorted parallel plate line is quite large at MHz frequencies ranges due to the relationship of the location of the feed to wavelength. Therefore, in this work we filled the interior region of the structure with deuterium (D_2O) in order to reduce the size of the antenna. **Figure 4.1** shows the structure of the designed antenna and the dimension are listed in **Table 4.1**.

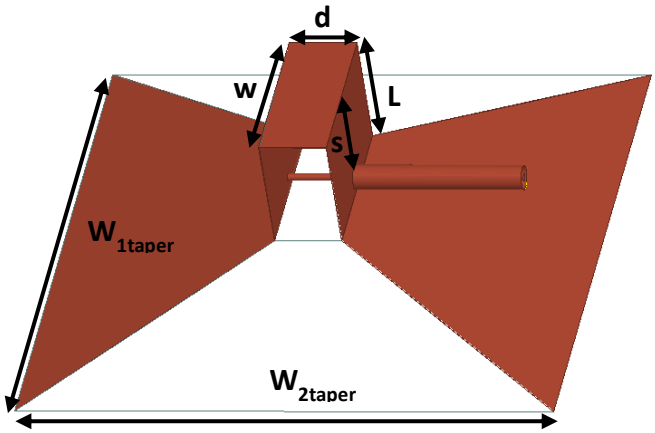

Figure 4.1: Designed TEM horn antenna.

Table 4.1. Dimensions of the designed TEM horn.

d	*w*	*s*	*L*	W_{1taper}	W_{2taper}
20 mm	50 mm	30 mm	34 mm	160 mm	160 mm

The antenna is fed using a coaxial cable placed approximately a quarter wavelength from the back plane (short) of the parallel plate line to have in phase reflected waves at the feed point. The coax shield is connected to the first plate and the center pin goes through the inside of parallel plate line and is connected to the opposite side. The tapered height of the antenna is usually on the order of a wavelength in order to be able to generate a broadband transition [103]. Linear tapering is used and the dimensions are adjusted to obtain a minimal reflection at the aperture. A 2 cm thick spacer filled with distilled water is used to separate the antenna from the phantom to avoid direct contact. For human use the spacer could be made to conform to the body's contour by using a flexible container.

4.2.2. Simulation and Results

4.2.2.1. Single-element Horn Antenna

To investigate the performance of the antenna, it is simulated using HFSS (High frequency structure simulator) in presence of a phantom that mimics the properties of the human torso ($\varepsilon_r = 34, \sigma = 0.8\, S/m$) [97], [104] as shown in **Figure 4.2**. The simulated S_{11} of the designed structure is shown in **Figure 4.3**, showing a perfect match at 200 MHz.

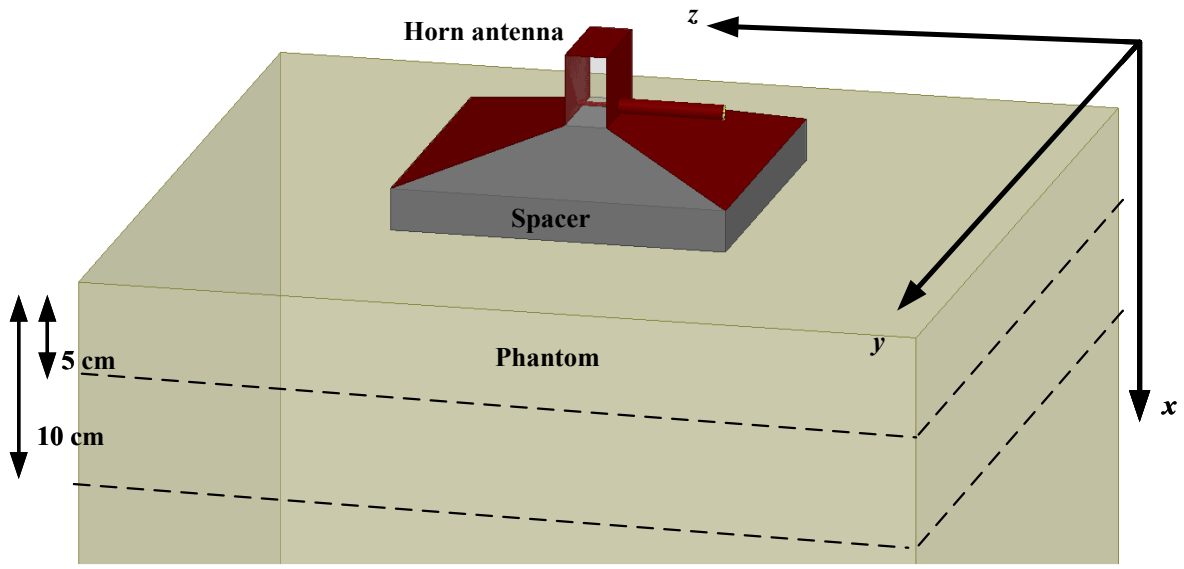

Figure 4.2. Simulation set-up.

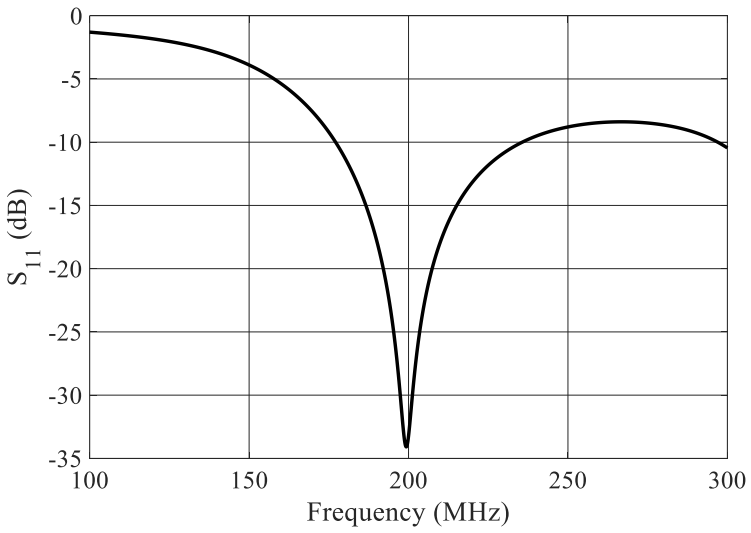

Figure 4.3. S_{11} of the designed TEM horn antenna.

The designed antenna is fed using lumped port (1 W power) at coaxial cable end. To find $\mathbf{B}_1^+$, SAR fields and other transmit and receive parameters, electric and magnetic fields are exported from HFSS to MATLAB for post processing. **Figure 4.2** shows axis description and the way that the phantom is placed inside the magnet. $\mathbf{B}_1^+$ field is plotted in coronal planes (*y*-*z* plane) for two different depth in the phantom (5 cm and 10 cm) as well as central transverse (*x*-*y* plane) and sagittal slices (*x*-*z* plane) in **Figure 4.4**. The $\mathbf{B}_1^+$ field is sufficiently high for imaging 5 cm and

10 cm depth targets. Sagittal and transverse fields show strong directive pattern for the transmit fields in *x* direction. Average SAR is also plotted in three different slices as shown in **Figure 4.5**.

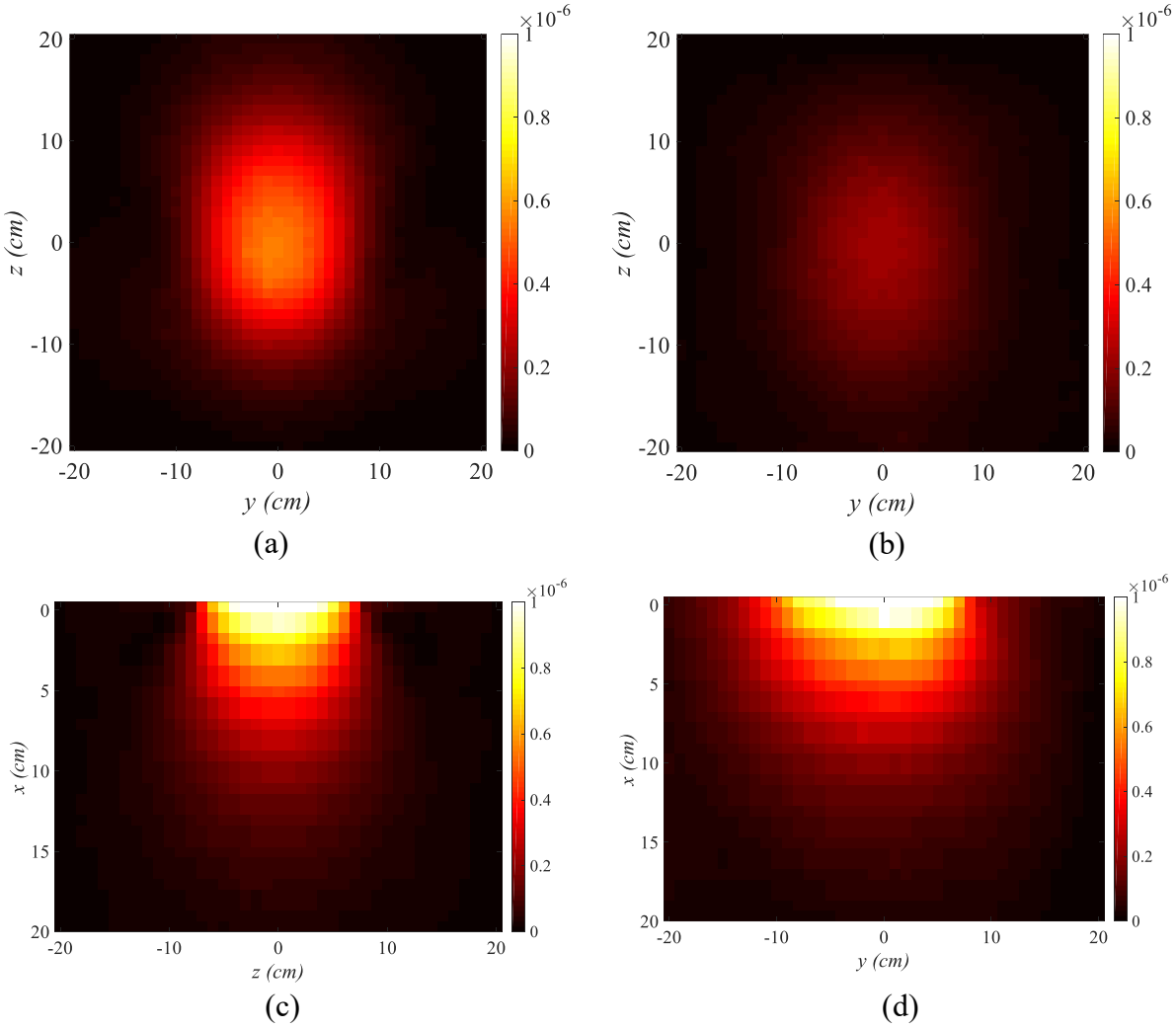

Figure 4.4. Horn antenna $\mathbf{B}_1^+$ plot on (a) coronal at depth of 5 cm, (b) coronal slice at depth of 10 cm, central slice (c) sagittal and (d) transverse slice [0 1 μT].

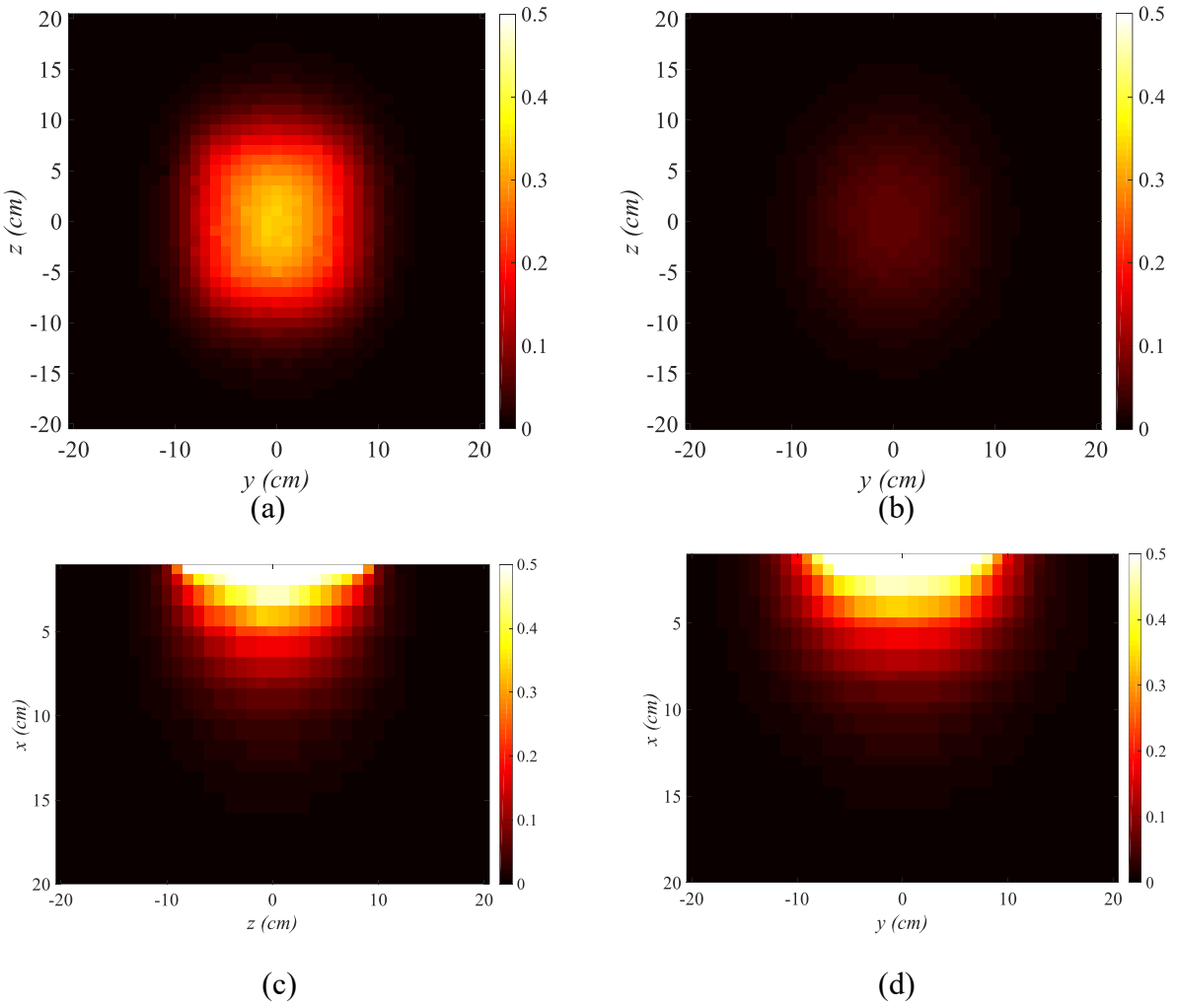

Figure 4.5. SAR plot on (a) coronal slice at depth of 5 cm, (b) coronal slice at depth of 10 cm, central slice (c) sagittal and (d) transverse slice [0 0.5W/kg].

4.2.2.2. Comparison to dipole and bowtie antenna

In [52], dipole antennas and conventional loops are specifically compared and the superior performance of dipole for deep targets is outlined. The bowtie antenna is a modification of the dipole antenna that provides higher bandwidth, which makes it less sensitive to slight changes in the frequencies as a result of movement, e.g., in cardiac imaging.

Here a half wavelength dipole (**Figure 4.6** (a)) and bow tie antenna (**Figure 4.6** (b)) are designed and simulated at 200 MHz using a 2 cm thickness spacer to separate the radiating element from the patient. The spacer is the ceramic material called D36 (Morgan

Electroceramics, Windsor, UK) used in [97]. Designed dimensions are listed in **Table 4.2**. Full wave simulations are done to investigate the performance of dipole antenna and compare it to the designed horn antenna.

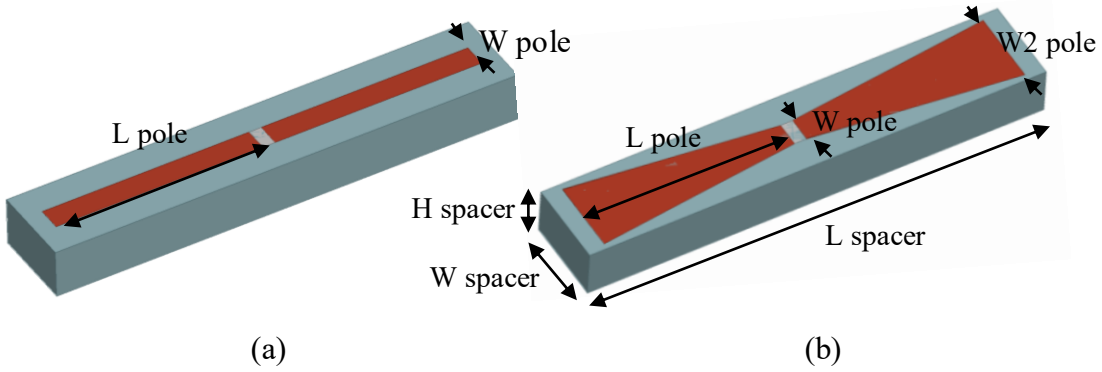

Figure 4.6. Designed dipole antenna (a) and bow tie antenna (b).

Table 4.2. Design parameters of the dipole and bowtie antennas.

L pole	W pole	W2 pole	L spacer	W spacer	H spacer
85 mm	10 mm	30 mm	190 mm	35 mm	20 mm

Lumped port excitations (1 W) are applied to the designed antennas and $\mathbf{B}_1^+$ field and SAR patterns are exported for post processing. The field patterns of a bow tie and a dipole are nearly identical, hence only fields for dipole are presented here. $\mathbf{B}_1^+$ field as well as SAR for above mentioned dipole is plotted in **Figure 4.7** and **Figure 4.8** respectively. It can be seen that $\mathbf{B}_1^+$ field is more symmetrical specifically in the coronal and transverse planes for horn antenna compared to dipole antenna. This is also the same case for SAR.

3D plots for the $\mathbf{B}_1^+$ field are shown in **Figure 4.9** which compare horn and dipole at 5 cm depth in coronal plane. This figure shows that horn generates the $\mathbf{B}_1^+$ fields in a wider area compared to pencil shaped pattern of the dipole. At a much higher depth (10 cm) where deep body targets are required to be imaged, the level of $\mathbf{B}_1^+$ field for these two types of antenna is compared (**Figure 4.10**). As can be seen the $\mathbf{B}_1^+$ field is stronger for the horn and it covers a wider area at that depth compared to dipole.

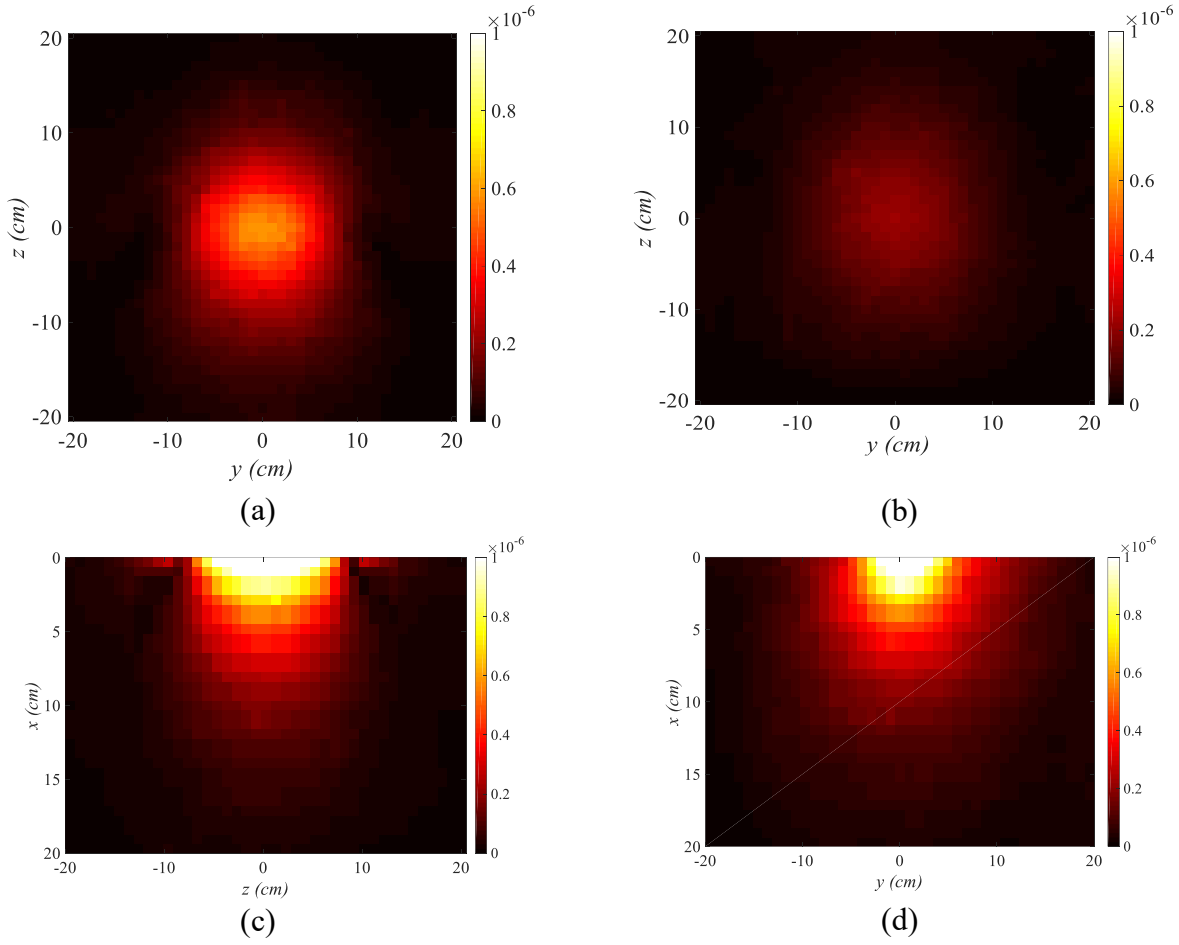

Figure 4.7. Dipole antenna $\mathbf{B}_1^+$ field plotted on (a) coronal slice at depth of 5 cm, (b) coronal slice at depth of 10 cm, central slice (c) sagittal and (d) transverse slice [0 1μT].

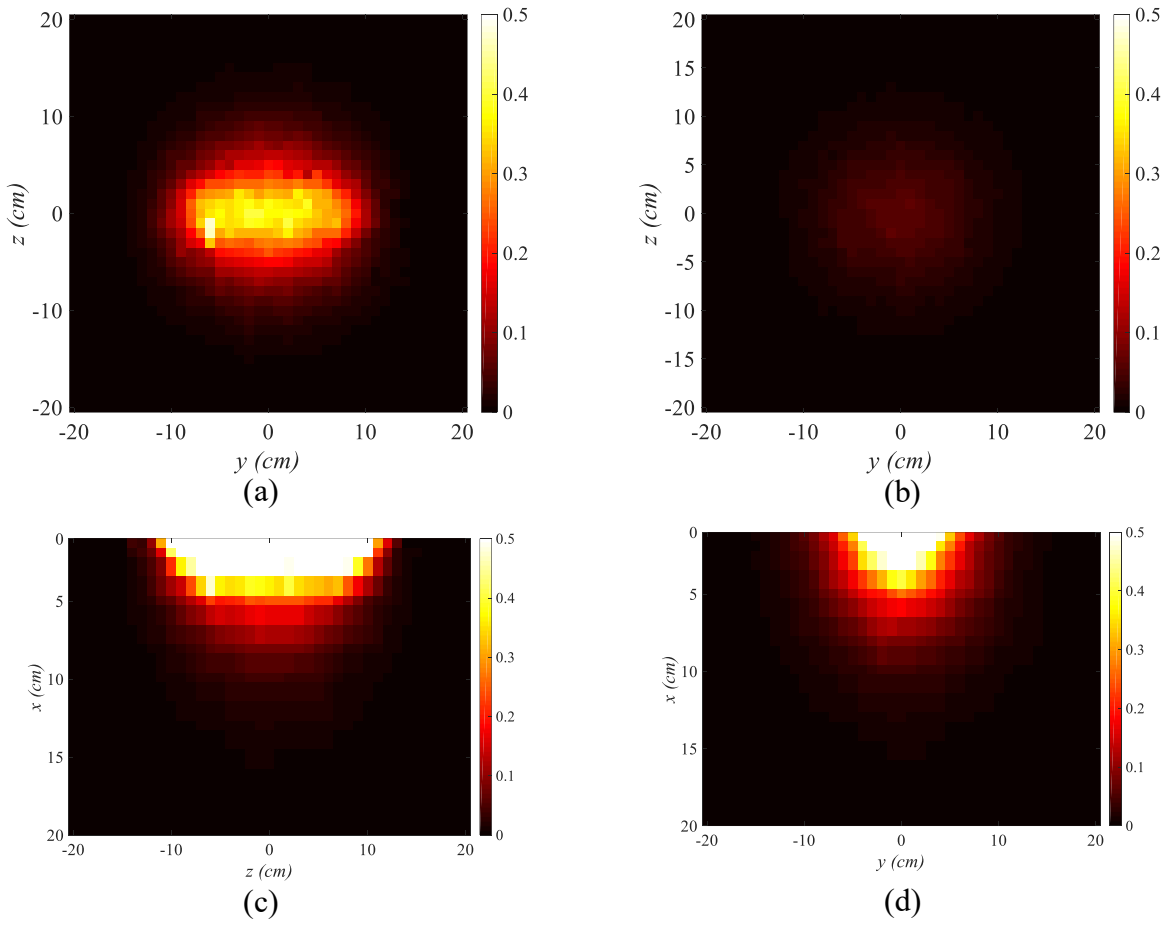

Figure 4.8. Dipole antenna SAR plotted on (a) coronal slice at depth of 5 cm, (b) coronal slice at depth of 10 cm, central slice (c) sagittal and (d) transverse slice [0–0.5 W/kg].

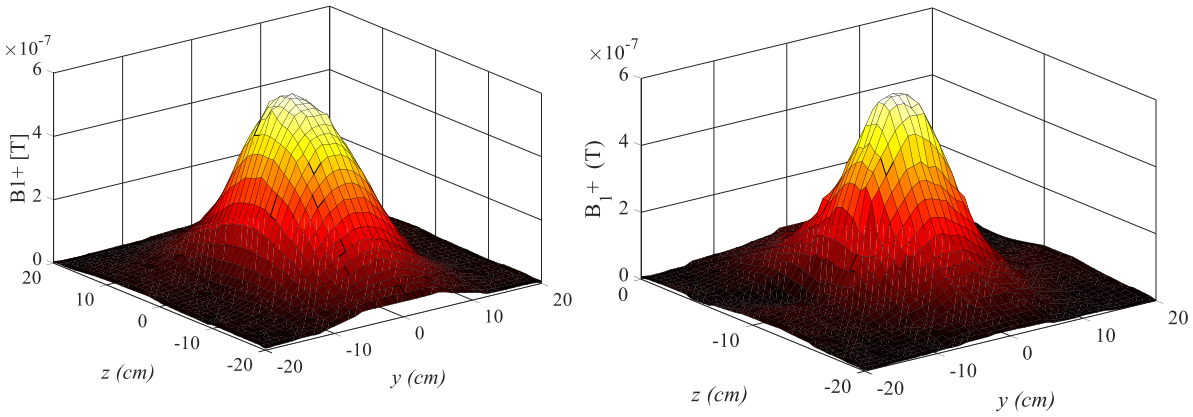

Figure 4.9. $\mathbf{B}_1^+$ plots on *y*-*z* plane for horn (left) and dipole (right).

If we compare a range of depths for these two antennas as shown in **Figure 4.11**, we conclude that although the fields are the same at the surface of the phantom for both these elements, it is higher for deeper areas which shows the advantage of the horn antenna compared to the dipole.

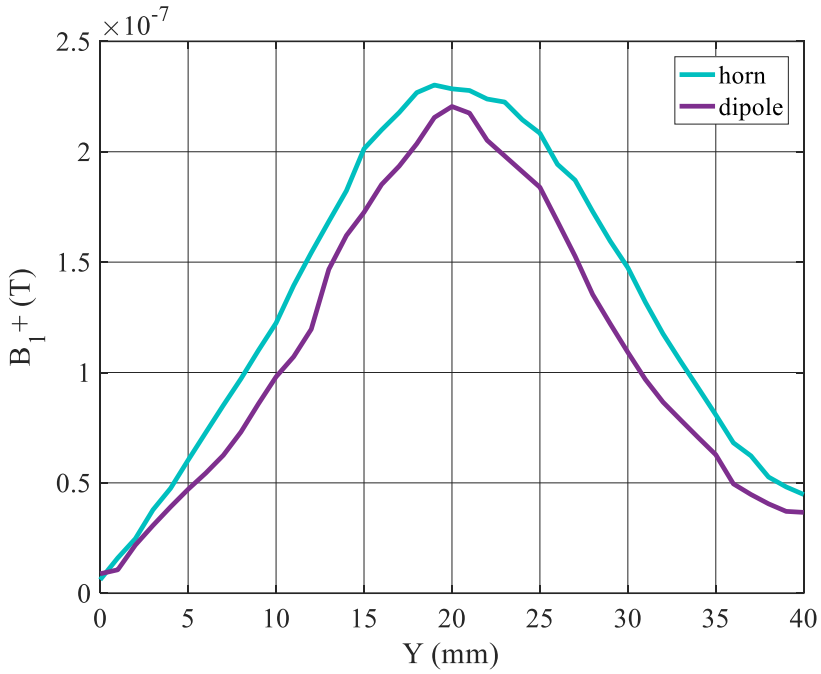

Figure 4.10. $\mathbf{B}_1^+$ field compared for horn antenna versus dipole in coronal slice at 10 cm depth.

For quantitative comparison, $\mathbf{B}_1^+$, SAR and transmit efficiencies are compared for horn, dipole and bowtie antenna in **Table 4.3**. As mentioned before, the bowtie operates similarly to dipole so there are no significant differences in their performance. Horn antenna produces more $\mathbf{B}_1^+$ field on average compared to dipole in the phantom. In terms of the ability to generate stronger fields versus the phantom depth, the horn is superior to the other two elements as it produces higher magnetic field averaged for different depths. On the other hand, average SAR generated by horn antenna is the same as dipole and bowtie antennas, and maximum SAR produced by horn is almost one third of the maximum SAR generated by dipole.

Transmit efficiencies as defined in Introduction [70] are excitation efficiency, $\mathbf{B}_1^+ / \sqrt{P_V}$, and safety efficiency, $\mathbf{B}_1^+ / \sqrt{\max(SAR)}$. Comparing the excitation efficiency of dipole/bowtie with

horn antenna shows that horn antenna performs about 10% better while safety efficiency shows a significant improvement (almost 100%) for horn antenna compared to dipole and bowtie.

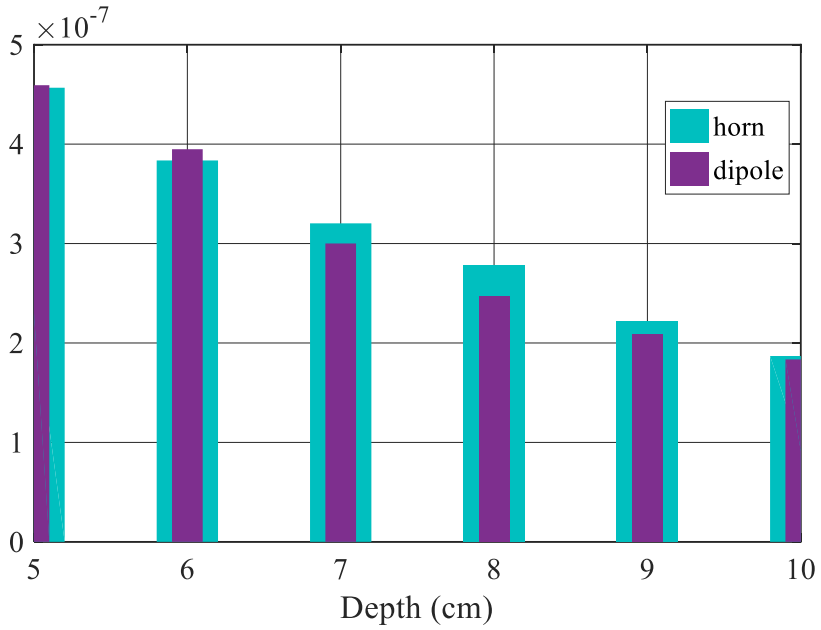

Figure 4.11. $\mathbf{B_1^+}$ field compared for horn and dipole antenna for different depths.

Table 4.3. Quantitative comparison between fields and efficiencies of dipole, bow-tie and horn antenna.

	Dipole	**Bow-tie**	**Horn**
B_1^+ average (μT)	0.042	0.043	0.049
B_1^+ average in 5 cm depth (μT) ($2cm^3$)	0.087	0.089	0.103
B_1^+ average in 10cm depth (μT) ($2cm^3$)	0.051	0.052	0.060
SAR averaged over phantom (W/kg)	0.015	0.015	0.015
SAR maximum (W/kg)	3.09	3.12	1.07
Deposited power (P_V) W	0.71	0.74	0.75
$\boldsymbol{B_1^+ / \sqrt{P_V}}$ **(μT/W/kg)**	5.0e-2	5.0e-2	5.6e-2
$\boldsymbol{B_1^+ / \sqrt{max(SAR)}}$ **(μT/W/kg)**	2.4e-2	2.4e-2	4.7e-2

4.2.3. Array performance

4.2.3.1. Two element horn array

To investigate the performance of a horn antenna when used in array, a two-element array of horn antennas was simulated and compared to a two-element array of dipoles by finding the mutual coupling between elements. The elements are placed 2cm from each other and each of them are excited with 1 W port excitation. **Figure 4.12** shows the two array configurations.

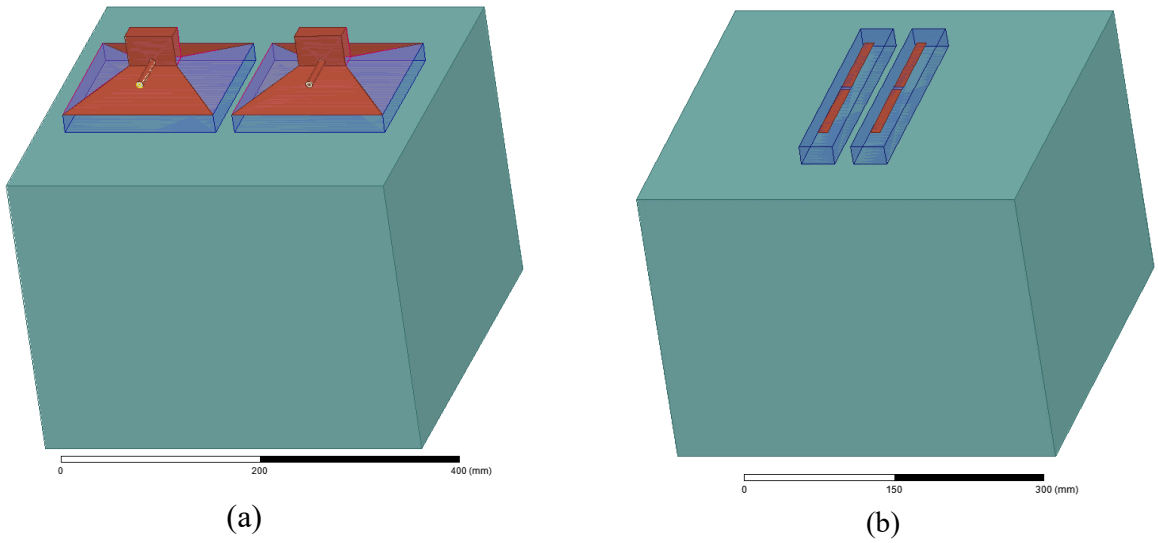

(a) (b)

Figure 4.12. Two elements array of (a) horn and (b) dipole.

Simulation results for mutual coupling (S_{12}) between elements are shown in **Figure 4.13**. As can be seen the mutual coupling between two element horn antenna (-25 dB) is significantly lower than that for dipole antennas (-9 dB). It is due to the fact that fields are confined to the aperture in a horn antenna hence less field is shared between neighboring elements due to fringe fields on the aperture edges. Whereas for a dipole, there are strong fields on the top of the dipole which will be shared with the adjacent element. This is a very attractive feature of horn antennas when used as array elements.

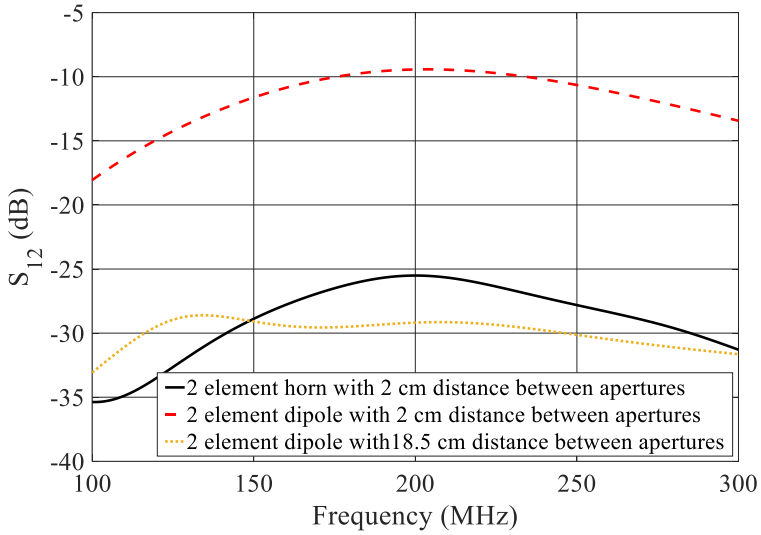

Figure 4.13. S_{12} of a two-element array of horn antennas compared to a two-element array of dipole antennas spaced according to Fig. 4.12b and so their centres are spaced the same as the horns in Fig. 4.12a.

4.2.3.2. Three element array

To investigate the ability of horn antenna to image deep targets, a three-element array of horn antennas is used around a body-size phantom (**Figure 4.14**). Each element is located on one side of the phantom, and is excited with 1 W input power. The excitation phase of elements 1–3 is 90̊, 180̊ and 0̊, respectively, to have constructive interference in the center of the phantom. Simulation results show that all three elements are matched to 200 MHZ (**Figure 4.15** (a)) and coupling level between all three elements is below -18 dB (**Figure 4.15** (b)).

$\mathbf{B}_1^+$ field generated inside the phantom is shown for the three element array in **Figure 4.16**. As can be seen, the $\mathbf{B}_1^+$ field strength at a depth of 10 cm is sufficient for imaging deep targets.

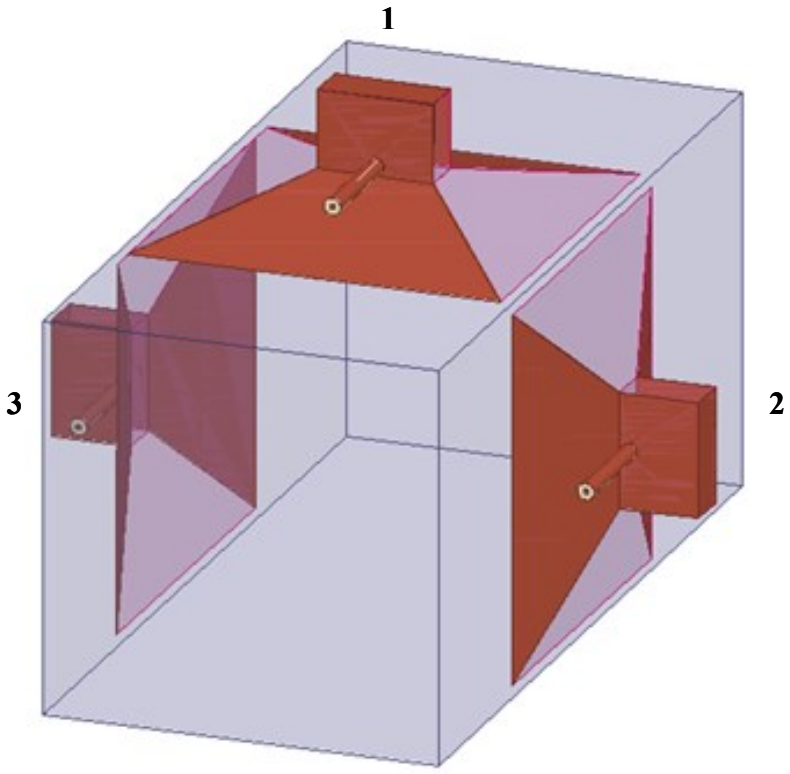

Figure 4.14. Three-element array of horn antennas.

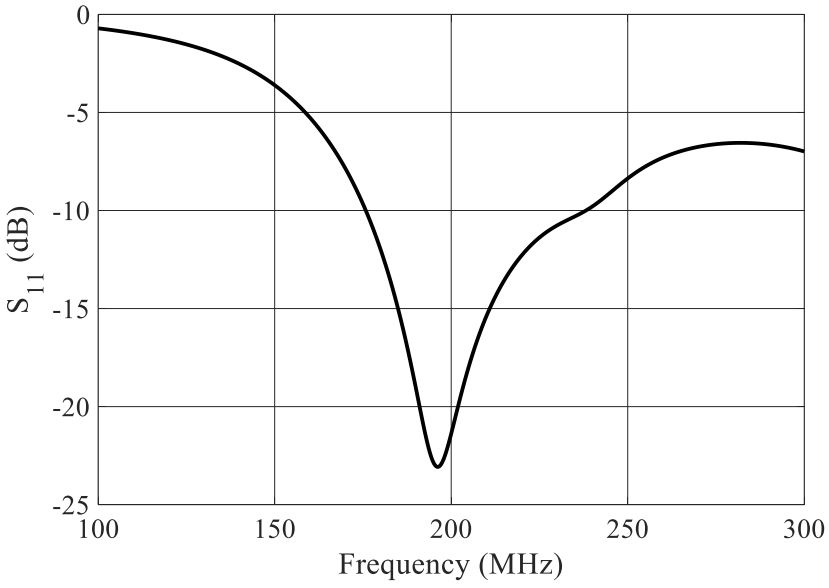

(a)

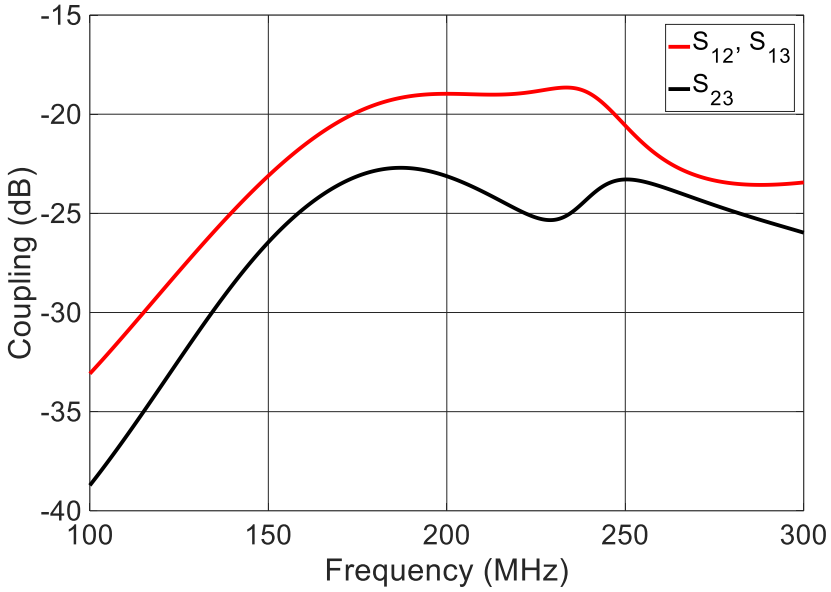

(b)

Figure 4.15. (a) S_{11} and (b) coupling level for the three element array.

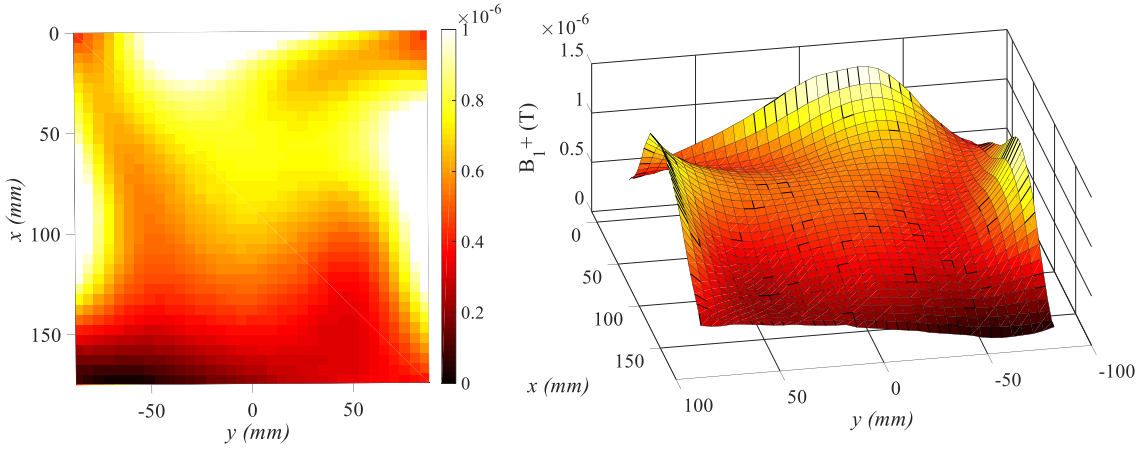

(a) (b)

Figure 4.16. $\mathbf{B}_1^+$ field in the transverse plane (a) 2-D and (b) 3-D for three elements excited with phases (90°-0°-180°).

4.3. Experiment

4.3.1. Fabrication

Horn antennas were built using hollow pyramidal structures filled with D_2O. To make such a complex structure, it is 3D printed with clear ABS plastic (Allied PhotoPolymers PhotoPolymers KZ-1862-ICE) with permittivity of $\varepsilon_r = 2$ and 2 mm thickness (Dancam Design). A cap is devised to fill the structure and an SMA connector is mounted onto the structure to provide the feed port. Adhesive copper sheets are used for the parallel plate waveguide, pyramid horn and back plane. A 2 cm depth spacer (PMMA also filled with deionized water) is used to separate the element from the phantom or patient. The phantom is a 17 ×17 ×35 cm^3 polyethylene container filled with a solution to mimic the average electrical properties of the body ($\varepsilon_r = 34, \sigma = 0.8\, S/m$) [97], [104]. The phantom is filled with a solution of isopropyl alcohol (2-Propanol, SIGMA-ALDRICH) with deionized water with the ratio of 0.5 ($^{V_{alcohol}}/_{V_{water}}$), 3.6 g/l NaCl and 1.95 g/l $CuSo_4.5H_2O$. The complex permittivity of the solution was measured using a Keysight 85070E Dielectric Probe. The fabricated element, placed on the spacer and phantom is shown in **Figure 4.17**.

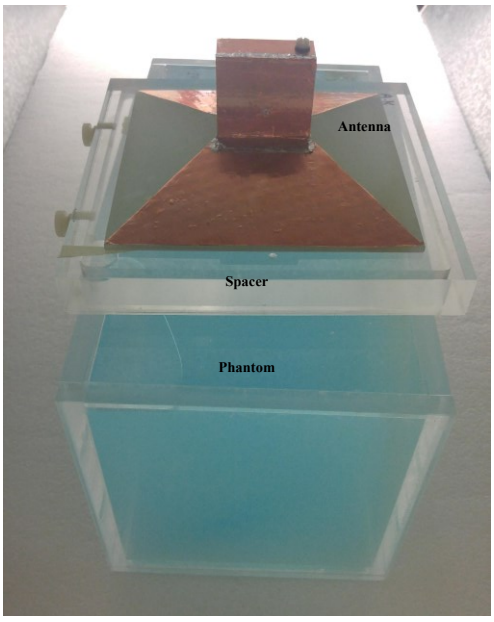

Figure 4.17. Fabricated horn antenna and phantom.

4.3.2. Bench Measurements

The scattering parameters of the horn antenna were measured using Agilent 4395A VNA. The S_{11} of the antenna in presence of the phantom is shown in **Figure 4.18**, where the antenna is well matched at 200 MHz. This frequency can be adjusted upwards by inserting plastic spacers a few mm in thickness between the horn and water-filled spacer.

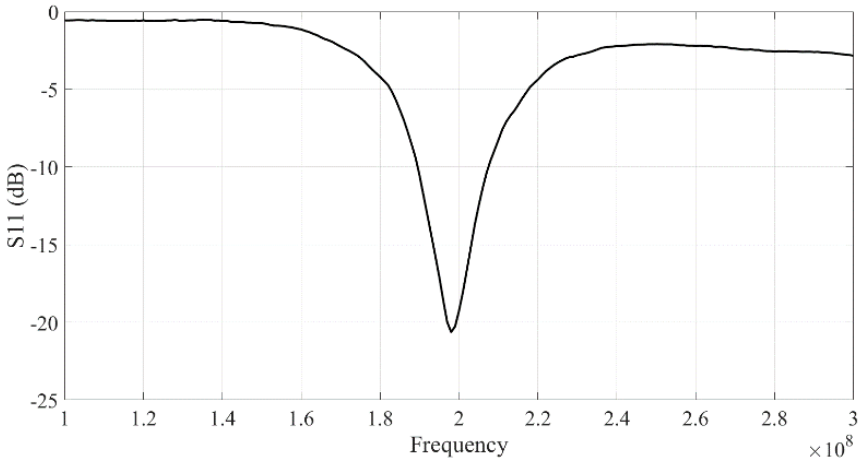

Figure 4.18. Measured S_{11} of the antenna in presence of phantom.

As the next step a two and three element array of horns as shown in **Figure 4.19** (a) and (b) respectively is tested on the bench and coupling is measured using VNA (Figure 20) to verify the simulation results. As can be seen in **Figure 4.20** (a), coupling between two side by side elements is below -20 dB which is consistent with the simulation results presented in **Figure 4.15**. On the other hand, coupling between elements in a three element arrangement is below -24 dB.

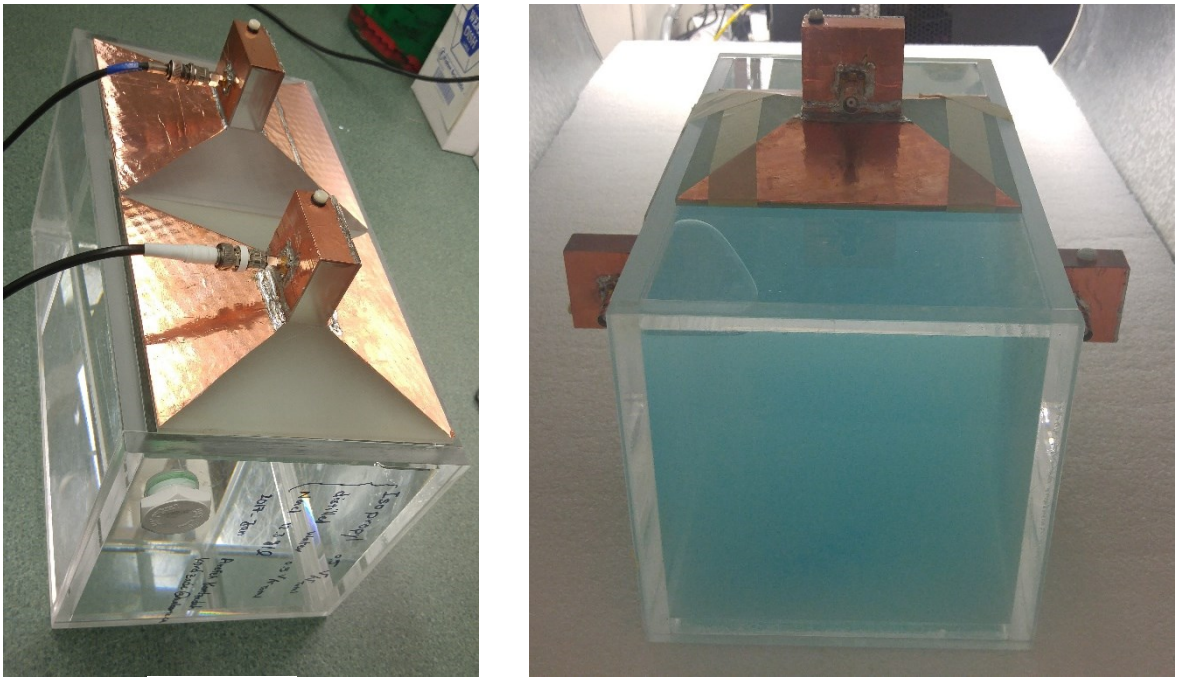

(a) (b)

Figure 4.19. Bench measuremenet for (a) two element array and (b) three element array of horn antennas.

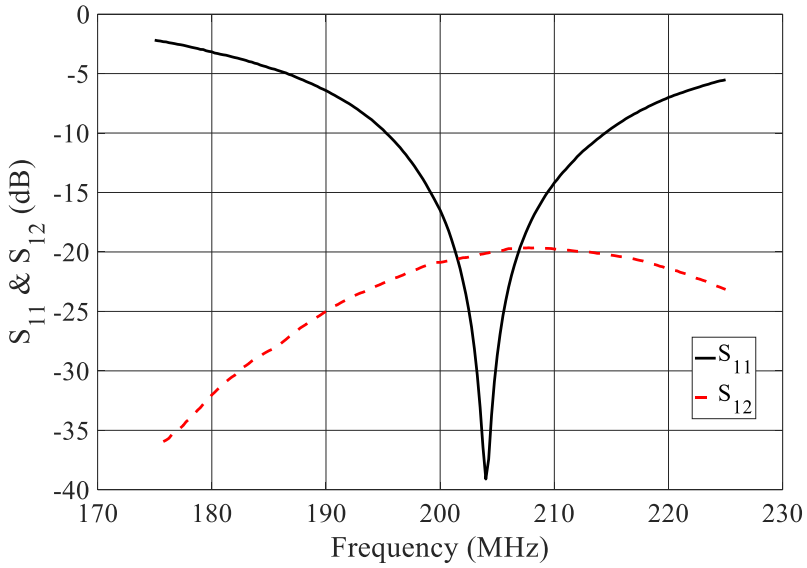

(a)

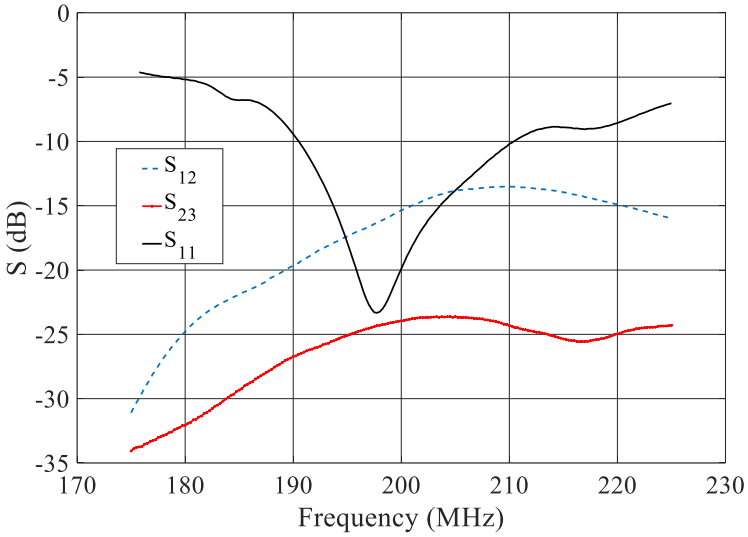

(b)

Figure 4.20. Measured coupling for (a) two element (b) three element horn array.

4.3.3. Scanner Measurements

To investigate the performance of horn antenna as a transmit/receive element, images are acquired on a 4.7 T whole-body MRI system (Unity Inova; Varian, Palo Alto, California) located at University of Alberta's Peter S. Allen NMR Centre. Flip angle (FA) maps are acquired using double angle method (DAM) [**B1 mapping** section] acquired at 60° and 120° and the resulting FA map is obtained from the ratio of the image magnitudes. The acquisition parameters are T_E=7 ms, T_R=1000 ms, 256×256 mm FOV and 1.3×1.3×8 mm resolution. **Figure 4.21** shows the acquired flip angle maps compared to the simulation results for single element $\mathbf{B}_1^+$ field in different orientations. Flip angle maps match simulated $\mathbf{B}_1^+$ field pattern in different orientations. The acquired images in three orientations are shown in **Figure 4.22**.

Multiple transmit is not possible on the current scanner, therefore the three element array is arranged as shown in **Figure 4.19** (b) with the top element used in transmit/receive mode, while the other two elements are receiving only. Flip angle maps are shown in **Figure 4.23**.

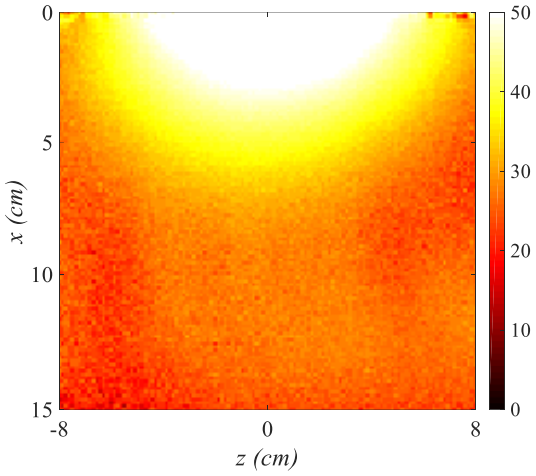

(a)

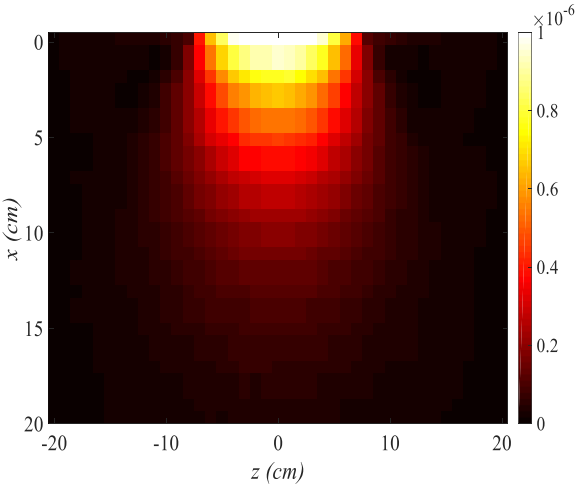

(d)

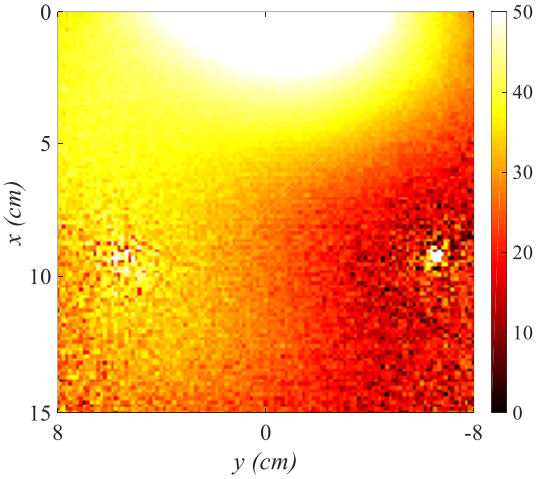

(b)

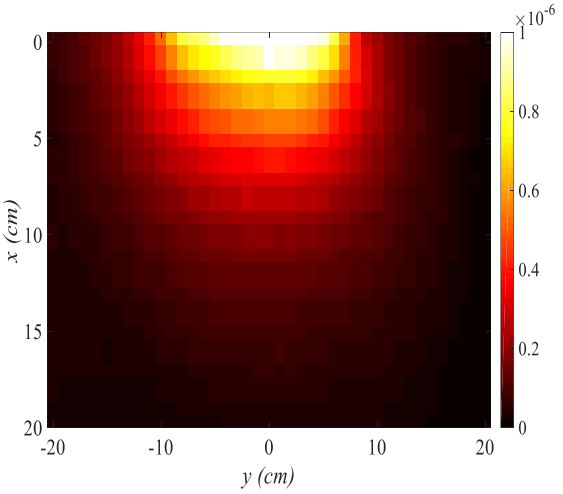

(f)

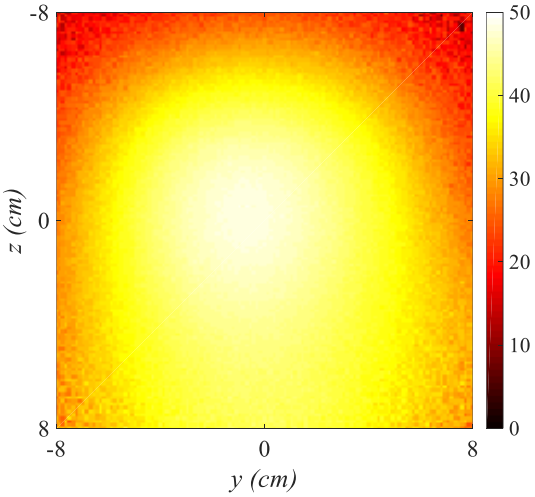

(c)

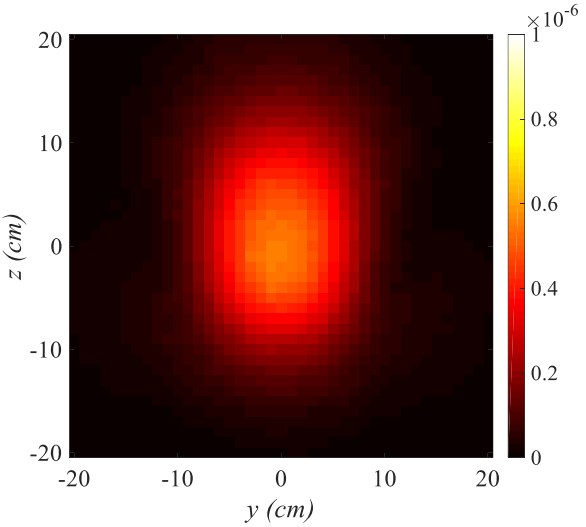

(e)

Figure 4.21. Flip angle maps [0 50°] on (a) *x-z*, (b) *x-y* and (c) *z-y* planes and simulated $\mathbf{B}_1^+$ for single element on (d) *x-z*, (e) *x-y* and (f) *z-y* planes.

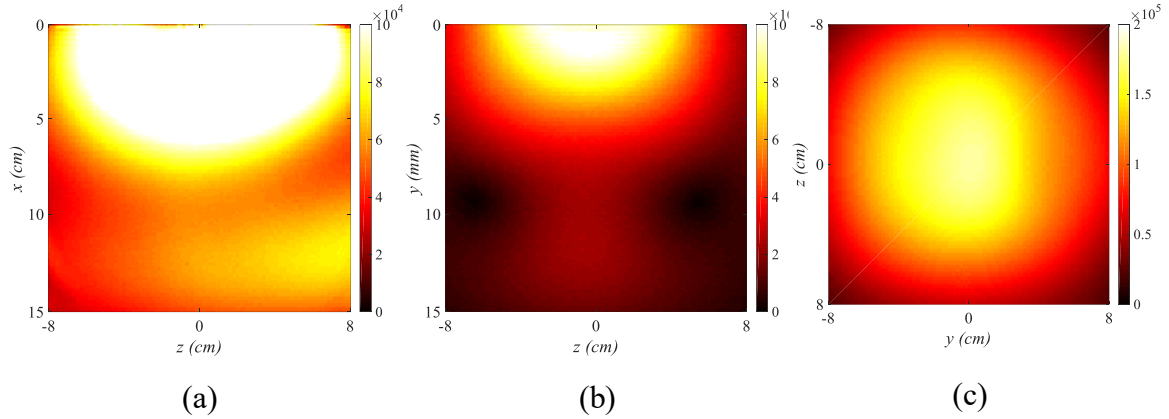

Figure 4.22. Images acquired using single element horn on (a) *x-z*, (b) *x-y* and (c) *z-y*.

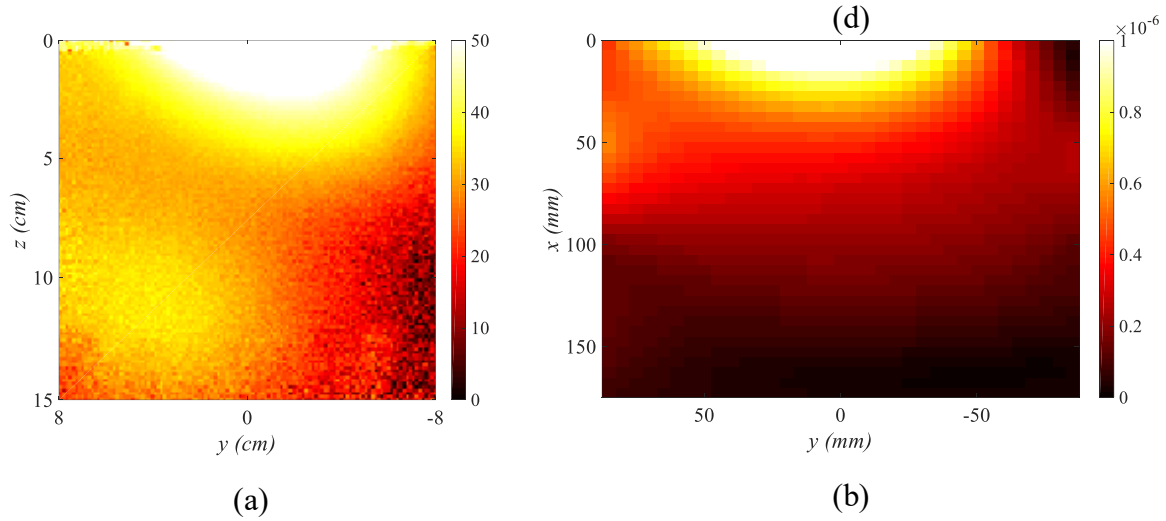

Figure 4.23. (a) Flip angle maps [0 50°] on *x-y* and (b) and simulated $\mathbf{B}_1^+$ for a three element array when one element is excited on *x-y* plane.

4.4. Discussion

In this chapter, a new element is introduced for imaging deep targets in the body at high field. The designed TEM horn antenna has promising properties due to its directive field pattern. Due to its complex structure, this element is 3D printed as a hollow container to hold D_2O which is

used to miniaturize the antenna dimensions. A body size phantom is designed to mimic the electrical properties of the torso.

To investigate the performance of TEM horn, a dipole and a bow-tie antenna are simulated and are compared in terms of transmit performance. Firstly, it is shown that dipole and bow-tie antenna performance is similar, as expected. Secondly, TEM horn is shown to generate slightly higher magnetic field for the same excitation especially at higher depth (5 cm, 10 cm). It is also shown that the dipole generates almost three times the maximum SAR as generated by the TEM horn. Comparing the elements in terms of transmit efficiencies show almost similar transmit efficiency is achieved by both elements however TEM horn generates significantly higher (twice) safety efficiency compared to dipole antenna. This proves the superior performance of TEM horn compared to dipole antenna.

In order to image body targets, TEM horn antenna will be used as an array. We have designed a three element array to image deep body targets. Results show that there is low coupling between elements in the array (<-18dB). Moreover, field patterns show significant magnetic field generated for the ROI.

The TEM Horn antennas were fabricated using 3D printing techniques and measurements were obtained on the bench. In the scanner, an array of horn antennas was used to image a body size phantom with dielectric properties close to those of the body, confirming the simulations.

4.5. Conclusion

In this chapter, TEM horn antenna is designed to image deep targets in the body area at high fields. The element has shown superior performance compared to the dipole antenna which is the preferred element to image body targets at high frequencies in literature. The high transmit efficiencies as well as directive field pattern of TEM horn antenna makes it a good candidate to image deep targets such as prostate or kidneys.

Chapter 5

Conclusion and Future Work

5.1. Conclusion

This thesis aims to overcome some of the challenges of the design and performance of radio frequency coils specifically used at 4.7 T.

Chapter 2 investigates dielectric liners that are used between the phantom and the RF coil for the purpose of increasing $\mathbf{B}_1$ field homogeneity. The effect of inserting liners with different permittivities is investigated and results show that very high permittivity liners will introduce resonant frequencies that are dangerously close to the Larmor frequency. Such liners also introduce undesired phase shifts, inhomogeneities, and SAR concentrations in the longitudinal direction. Therefore an optimal permittivity is found by minimizing reflections at the interfaces of the various dielectric media. The liner also minimizes coupling between elements while keeping the liner's dielectric resonance frequency at a safe distance of at least one octave from the Larmor frequency. It was found that a compromise should be made between desired improvements in magnetic field homogeneity in the transverse plane and unwanted degradation in transmit efficiency.

Chapter 3 addresses the issue of coupling that is enhanced as a result of inserting high permittivity liners. Both real and imaginary parts of the mutual impedance increase significantly as a result of displacement currents in the HDC liner. By using capacitive bridges, mutual resistance and reactance are practically eliminated between adjacent elements. Removing both resistive and reactive terms of the mutual impedance is therefore achievable without degradation in the transmit performance of the array. Decoupling levels up to -32 dB are achieved which is much better than many arrays reported in the literature.

Finally, chapter 4 introduces a new element for imaging body regions. The element is a TEM horn antenna which is filled with D_2O for minimizing its dimensions. The designed TEM horn antenna has shown promising results for imaging deep targets due to its directive field pattern. Simulation results demonstrate improved efficiency of the horn antenna compared to the dipole

antenna especially for deep targets. The safety efficiency of the TEM horn element is almost twice that of a dipole and also it generates higher magnetic field at higher depths. An array of horn antennas is used to image a body size phantom to verify simulations. Coupling between elements of the array is low (<-18 dB) and the resulting field maps agree with the simulations.

5.2. Future Directions

The present hardware on the 4.7T system is unable to perform multi-transmit imaging such as parallel transmit with independent control over each channel where elements are decoupled and the field maps are distinct from each other.. When the upgrade to the current system is complete, eight channel transmit/receive will be used to investigate the transmit performance of the arrays described in this thesis when all channels are excited simultaneously. The transmit performance of the arrays will be evaluated by performing $\mathbf{B}_1$ shimming, moving SAR hot spots, and other techniques including measurement of sensitivity patterns and g-factors.

Following ethics approval, the 4.7T TEM horn array should also be verified in vivo on volunteers to image deep targets in the body such as the prostate or kidneys. It is anticipated that the TEM horn will become an advantageous element also in the construction of arrays of mixed types of elements (e.g., in combination with loops or other structures).The effects of dielectric liners on arrays of elements of different types and arrangements should be further studied to fully understand the impact of the liner on array performance and safety. This includes investigating the effects on a variety of anatomical regions and at frequencies above and below 200 MHz.

The TEM horn antenna can be adapted to higher frequencies (300 MHz and 400 MHz) to be used in ultra-high-field imaging. The TEM horn should perform efficiently due to the short wavelength and smaller dimensions achieved at high fields, making it a good candidate for imaging at these field strengths. In addition to imaging, the TEM horn array can also be used in hyperthermia due to its directive pattern, lower SAR at the surface than dipoles and compact dimensions.

References

[1] F. Bloch, "Nuclear induction," *Phys. Rev.*, vol. 70, no. 7–8, pp. 460–474, 1946.

[2] E. Purcell, H. Torrey, and R. Pound, "Resonance Absorption by Nuclear Magnetic Moments in a Solid," *Phys. Rev.*, vol. 69, no. 1–2, pp. 37–38, 1946.

[3] P. C. Lauterbur, "Image Formation by Induced Local Interactions: Examples Employing Nuclear Magnetic Resonance," *Nature*, vol. 242, no. 5394, pp. 190–191, Mar. 1973.

[4] P. Mansfield and P. K. Grannell, "NMR 'diffraction' in solids?," *J. Phys. C Solid State Phys.*, vol. 6, no. 22, pp. L422–L426, Nov. 1973.

[5] S. Ogawa, T. M. Lee, A. S. Nayak, and P. Glynn, "Oxygenation-sensitive contrast in magnetic resonance image of rodent brain at high magnetic fields," *Magn. Reson. Med.*, vol. 14, no. 1, pp. 68–78, 1990.

[6] J. W. Belliveau, B. R. Rosen, H. L. Kantor, R. R. Rzedzian, D. N. Kennedy, R. C. McKinstry, J. M. Vevea, M. S. Cohen, I. L. Pykett, and T. J. Brady, "Functional cerebral imaging by susceptibility-contrast NMR," *Magn. Reson. Med.*, vol. 14, no. 3, pp. 538–546, 1990.

[7] D. I. Hoult, "The principle of reciprocity in signal strength calculations—A mathematical guide," *Concepts Magn. Reson.*, vol. 12, no. 4, pp. 173–187, 2000.

[8] P. C. L. Zhi-Pei Liang, *Principles of Magnetic Resonance Imaging: A Signal Processing Perspective*. Wiley-IEEE Press.

[9] A. Dula, E. Welch, and J. Creasy, "Challenges and opportunities of ultra-high field MRI," *IFMBE Proc.*, vol. 27, pp. 1–5, 2010.

[10] L. B. Pierre-Marie Robitaille, *Ultra High Field Magnetic Resonance Imaging*, vol. 26. Springer US, 2006, 2006.

[11] Massimo Filippi, *fMRI Techniques and Protocols*, vol. 41. Totowa, NJ: Humana Press, 2009.

[12] D. Rovnyak, J. C. Hoch, A. S. Stern, and G. Wagner, "Resolution and sensitivity of high field nuclear magnetic resonance spectroscopy," *J. Biomol. NMR*, vol. 30, no. 1, pp. 1–10, Sep. 2004.

[13] T. Neuberger, V. Gulani, and A. Webb, "Sodium renal imaging in mice at high magnetic fields," *Magn. Reson. Med.*, vol. 58, no. 5, pp. 1067–1071, 2007.

[14] O. Speck, M. Weigel, and K. Scheffler, *High-Field MR Imaging*. Berlin, Heidelberg: Springer Berlin Heidelberg, 2012.

[15] P. Jezzard, S. Duewell, and R. S. Balaban, “MRrelaxation times in human brain: measurement at 4 T,” *Radiology*, 1996.

[16] B. R. Jezzard P, Duewell S, “MRrelaxation times in human brain: measurement at 4 T,” *Radiology*, 1996.

[17] C.-N. Chen and D. I. Hoult, *Biomedical Magnetic Resonance Technology*, 2nd ed. CRC Press, 1989.

[18] J. Thomas Vaughan, John R. Griffiths. *RF Coils for MRI*. Chichester, UK: John Wiley & Sons, Ltd, 2012.

[19] “International Standard; IEC 60601-2-33,” 2002.

[20] D. Qian, A.-M. El-Sharkawy, P. Bottomley, and W. Edelstein, “An RF dosimeter for independent SAR measurement in MRI scanners.,” *Med. Phys.*, vol. 40, no. 12, p. 122303, 2013.

[21] M. Kozlov and R. Turner, “Analysis of Transmit Performance Optimization Strategies for Multi Channel MRI Array,” *Power*, pp. 1622–1626, 2011.

[22] R. Stollberger and P. Wach, “Imaging of the active B1 field in vivo,” *Magn. Reson. Med.*, vol. 38, no. 2, p. 336, 1997.

[23] C. A. Balanis, *Advanced Engineering Electromagnetics, 2nd Edition*. 2012.

[24] D. M. Pozar, *Microwave Engineering*, Third Edit. John Wiley & Sons, Inc., 2005.

[25] S. M. Wright and L. L. Wald, “Theory and application of array coils in MR spectroscopy,” *NMR Biomed.*, vol. 10, no. 8, pp. 394–410, 1997.

[26] C. Gabriel, S. Gabriel, and E. Corthout, “The dielectric properties of biological tissues: I. Literature survey.,” *Phys. Med. Biol.*, vol. 41, no. 11, pp. 2231–49, 1996.

[27] J. S. Hyde, A. Jesmanowicz, W. Froncisz, J. Bruce Kneeland, T. M. Grist, and N. F. Campagna, “Parallel image acquisition from noninteracting local coils,” *J. Magn. Reson.*, vol. 70, no. 3, pp. 512–517, 1986.

[28] P. B. Roemer, W. A. Edelstein, C. E. Hayes, S. P. Souza, O. M. Mueller “The NMR phased array.,” vol. 16, no. 2, pp. 192–225, 1989.

[29] D. J. Larkman and R. G. Nunes, “Parallel magnetic resonance imaging,” *Phys Med Biol*, vol. 52, no. 7, pp. R15–55, 2007.

[30] and B. G. F. N. De Zanche, A. Maunder, T. Charlton, K. Wachowicz, “A Unified Framework for SNR Comparisons of Four Array Image Combination Methods,” in *ISMRM*, 2011.

[31] S. B. King, S. M. Varosi, and G. R. Duensing, “Optimum SNR data compression in hardware using an Eigencoil array,” *Magn. Reson. Med.*, vol. 63, no. 5, pp. 1346–1356, 2010.

[32] A. Deshmane, V. Gulani, M. A. Griswold, and N. Seiberlich, “Parallel MR imaging,” *J. Magn. Reson. Imaging*, vol. 36, no. 1, pp. 55–72, 2012.

[33] K. P. Pruessmann, M. Weiger, M. B. Scheidegger, and P. Boesiger, “._SENSE sensitivity encoding for fast MRI.pdf,” *Magn. Reson. Med. Off. J. Soc. Magn. Reson. Med. / Soc. Magn. Reson. Med.*, vol. 42, no. 5, pp. 952–962, 1999.

[34] D. K. Sodickson and W. J. Manning, “Simultaneous acquisition of spatial harmonics (SMASH): fast imaging with radiofrequency coil arrays.,” *Magn. Reson. Med.*, vol. 38, no. 4, pp. 591–603, Oct. 1997.

[35] S. M. Wright, M. P. Mcdougall, and K. Kurpad, “Coil Array for Parallel MRI:introduction and overview,” in *Second International Workshop on Parallel MRI, Latsis symposium*, 2004.

[36] M. A. Griswold, P. M. Jakob, R. M. Heidemann, M. Nittka, V. Jellus, J. Wang, B. Kiefer, and A. Haase, “Generalized Autocalibrating Partially Parallel Acquisitions (GRAPPA),” *Magn. Reson. Med.*, vol. 47, no. 6, pp. 1202–1210, 2002.

[37] H. Omer and R. Dickinson, “A Graphical Generalized Implementation of SENSE Reconstruction Using Matlab,” *Concepts Magn. Reson. Part A*, vol. 36A(3), pp. 178–186, 2010.

[38] D. K. Sodickson, “Spatial encoding using multiple RF coils: SMASH imaging and parallel MRI,” *Methods Biomed. Magn. Reson. Imaging Spectrosc.*, vol. 1, no. 4, pp. 239–250, 2000.

[39] U. Katscher and P. Bornert, “Parallel RF transmission in MRI,” *NMR Biomed.*, vol. 19, no. 3, pp. 393–400, 2006.

[40] T. S. Ibrahim, R. Lee, B. A. Baertlein, A. M. Abduljalil, H. Zhu, and P. M. L. Robitaille, “Effect of RF coil excitation on field inhomogeneity at ultra high fields: A field optimized TEM resonatior,” *Magn. Reson. Imaging*, vol. 19, no. 10, pp. 1339–1347, 2001.

[41] J. M. Pauly, D. G. Nishimura, and A. MacOvski, “Introduction to: A k-space analysis of small-tip-angle excitation,” *J. Magn. Reson.*, vol. 213, no. 2, pp. 558–559, 2011.

[42] W. Grissom, C. Y. Yip, Z. Zhang, V. A. Stenger, J. A. Fessler, and D. C. Noll, “Spatial domain method for the design of RF pulses in multicoil parallel excitation,” *Magn. Reson. Med.*, vol. 56, no. 3, pp. 620–629, 2006.

[43] K. Setsompop, “Design Algorithms for Parallel Transmission in Magnetic Resonance

Imaging.," 2008.

[44] D. C. Noll, W. A. Grissom, and C. Yip, "RF Pulse Design for Parallel Excitation," in *ISMRM*, vol. 0, no. 7.

[45] U. Katscher, P. Bornert, C. Leussler, and J. S. van den Brink, "Transmit SENSE," *Magn. Reson. Med.*, vol. 49, no. 1, pp. 144–150, 2003.

[46] W. A. Grissom, "RF Pulse Design for Parallel Excitation," 2008.

[47] Y. Zhu, "Parallel Excitation with an Array of Transmit Coils," *Magn. Reson. Med.*, vol. 51, no. 4, pp. 775–784, 2004.

[48] L. L. Zelinski, Adam C, Wald, K. Setsompop, and E. Goyal, Vivek K, Adalsteinsson, "Sparsity-Enforced Slice-Selective MRI RF Excitation Pulse Design," *IEEE Trans. Med. Imaging*, vol. 27, no. 9, pp. 1213–1229, 2008.

[49] S. Saekho, C. Y. Yip, D. C. Noll, F. E. Boada, and V. A. Stenger, "Fast-kz three-dimensional tailored radiofrequency pulse for reduced B1 inhomogeneity," *Magn. Reson. Med.*, vol. 55, no. 4, pp. 719–724, 2006.

[50] B. K. Li, F. Liu, and S. Crozier, "Focused, eight-element transceive phased array coil for parallel magnetic resonance imaging of the chest - Theoretical considerations," *Magn. Reson. Med.*, vol. 53, no. 6, pp. 1251–1257, 2005.

[51] A.G. WEBB, "Dielectric Materials in Magnetic Resonance," *Harv. Bus. Rev.*, vol. 88, no. 12, pp. 148–184, 2010.

[52] A. J. E. Raaijmakers, P. R. Luijten, and C. A. T. van den Berg, "Dipole antennas for ultrahigh-field body imaging: a comparison with loop coils," *NMR Biomed.*, vol. 29, no. 9, pp. 1122–1130, Sep. 2016.

[53] L. J. B. Pierre-Marie Robitaille, *Ultra high field magnetic resonance imaging*. NY, USA: Springer Science, 2007.

[54] P. Yazdanbakhsh and K. Solbach, "Active Phased Array Techniques for High-Field MRI," in *3rd European Conference on Antennas and Propagation, Berlin*, 2009, pp. 1367–1371.

[55] K. Haines, N. B. Smith, and A. G. Webb, "New high dielectric constant materials for tailoring the B1+ distribution at high magnetic fields.," *J. Magn. Reson.*, vol. 203, no. 2, pp. 323–7, Apr. 2010.

[56] A. G. Webb, "Dielectric Materials in Magnetic Resonance," *Concepts inMagnetic Reson. Part A*, vol. 38A(4), pp. 148–184, 2011.

[57] W. Luo, M. T. Lanagan, C. T. Sica, Y. Ryu, S. Oh, M. Ketterman, Q. X. Yang, and C. M.

Collins, “Permittivity and performance of dielectric pads with sintered ceramic beads in MRI: early experiments and simulations at 3 T.,” *Magn. Reson. Med.*, vol. 70, no. 1, pp. 269–75, Jul. 2013.

[58] H. Ikehira, T. Sunaga, T. Obata, S. Furukawa, M. Tamura, E. Yoshitome, and S. Tanada, “Development of a dielectric equivalent gel for better impedance matching for human skin,” in *Proc. Intl. Soc. Mag. Reson. Med. 11*, 2003, vol. 11, p. 2435.

[59] W. M. Brink and A. G. Webb, “High permittivity pads reduce specific absorption rate, improve B 1 homogeneity, and increase contrast-to-noise ratio for functional cardiac MRI at 3 T,” *Magn. Reson. Med.*, vol. 71, no. 4, pp. 1632–1640, 2014.

[60] Q. X. Yang, S. Rupprecht, W. Luo, C. Sica, Z. Herse, J. Wang, Z. Cao, J. Vesek, M. T. Lanagan, G. Carluccio, Y.-C. Ryu, and C. M. Collins, “Radiofrequency field enhancement with high dielectric constant (HDC) pads in a receive array coil at 3.0T.,” *J. Magn. Reson. Imaging*, vol. 38, no. 2, pp. 435–40, Aug. 2013.

[61] A. Rennings, K. Wang, L. Chen, F. Wetterling, and D. Erni, “An Electromagnetic-Simulation based Investigation of the Dielectric padding approach for head imaging at 7T,” in *Proc. Intl. Soc. Mag. Reson. Med. 22*, 2014, vol. 10, no. 2701, pp. 3–7.

[62] Q. X. Yang, Z. G. Herse, M. Ketterman, J. Wang, C. Sica, C. Collins, M. Lanagan, and C. C, “Enhancement of RF field by high dielectric constant pad at 3T : Cervical Spine Imaging,” in *Proc. Intl. Soc. Mag. Reson. Med.*, 2011, vol. 203, no. 2, p. 2771.

[63] Q. X. Yang, J. Wang, J. Wang, C. M. Collins, C. Wang, and M. B. Smith, “Reducing SAR and enhancing cerebral signal-to-noise ratio with high permittivity padding at 3 T.,” *Magn. Reson. Med.*, vol. 65, no. 2, pp. 358–62, Feb. 2011.

[64] P. de Heer, W. M. Brink, B. J. Kooij, and a G. Webb, “Increasing signal homogeneity and image quality in abdominal imaging at 3 T with very high permittivity materials.,” *Magn. Reson. Med.*, vol. 68, no. 4, pp. 1317–24, Oct. 2012.

[65] W. M. Teeuwisse, W. M. Brink, K. N. Haines, and a G. Webb, “Simulations of high permittivity materials for 7 T neuroimaging and evaluation of a new barium titanate-based dielectric.,” *Magn. Reson. Med.*, vol. 67, no. 4, pp. 912–8, Apr. 2012.

[66] T. K. F. Foo, C. E. Hayes, and Y.-W. Kang, “Reduction of Rf Penetration Effects in High-Field Imaging,” *Magn. Reson. Med.*, vol. 23, no. 2, pp. 287–301, 1992.

[67] S. M. Wright and L. L. Wald, “Theory and application of array coils in MR spectroscopy.,” *NMR Biomed.*, vol. 10, no. 8, pp. 394–410, Dec. 1997.

[68] R. F. Harrington, *Time-harmonic electromagnetic fields*. IEEE Press : Wiley-Interscience, 2001.

[69] A. B. G. Herbert J. Carlin, *Network Theory:An Introduction to Reciproval and Nonreciprocal Circuits*. Prentice-Hall, Inc., Englewood cliffs, N.J., 1946.

[70] M. Kozlov and R. Turner, "Influence of Shield Distance on RF Transmit Performance for a 7T Multi-channel MRI Loop Array," *Prog. Electromagn. Res. Symp. Proc.*, pp. 255–259, 2012.

[71] N. I. Avdievich, J. W. Pan, and H. P. Hetherington, "Resonant inductive decoupling (RID) for transceiver arrays to compensate for both reactive and resistive components of the mutual impedance," *NMR Biomed.*, vol. 26, no. 11, pp. 1547–1554, Nov. 2013.

[72] P. B. Roemer, W. A. Edelstein, C. E. Hayes, S. P. Souza, and O. M. Mueller, "The NMR phased array," *Magn. Reson. Med.*, vol. 16, no. 2, pp. 192–225, Nov. 1990.

[73] A. Kordzadeh and N. De Zanche, "Optimal Permittivity of Dielectric Liners and their Effects on Transmit Array Performance Purpose," in *Proc. Intl. Soc. Mag. Reson. Med. 23*, 2015.

[74] M. Kozlov and R. Turner, "Assessment of Decoupling between MRI Array Elements at 300 MHz," vol. 9, pp. 1020–1024, 2013.

[75] R. F. Lee, R. O. Giaquinto, and C. J. Hardy, "Coupling and decoupling theory and its application to the MRI phased array.," *Magn. Reson. Med.*, vol. 48, no. 1, pp. 203–13, Jul. 2002.

[76] A. M. Maunder, M. Daneshmand, P. Mousavi, B. G. Fallone, and N. De Zanche, "Stray Capacitance Between Magnetic Resonance Imaging Coil Elements: Models and Application to Array Decoupling," *IEEE Trans. Microw. Theory Tech.*, vol. 61, no. 12, pp. 4667–4677, Dec. 2013.

[77] X. Zhang and A. Webb, "Design of a capacitively decoupled transmit/receive NMR phased array for high field microscopy at 14.1T," *J. Magn. Reson.*, vol. 170, no. 1, pp. 149–55, Sep. 2004.

[78] C. Von Morze, J. Tropp, S. Banerjee, D. Xu, K. Karpodinis, L. Carvajal, C. P. Hess, P. Mukherjee, S. Majumdar, and D. B. Vigneron, "An eight-channel, nonoverlapping phased array coil with capacitive decoupling for parallel MRI at 3 T," *Concepts Magn. Reson. Part B Magn. Reson. Eng.*, vol. 31, no. 1, pp. 37–43, 2007.

[79] J. Jevtic, "Ladder networks for capacitive decoupling in phased-array coils," *Proc. 9th Annu. Meet. ISMRM,* vol. 9, p. 10437, 2001.

[80] M. Weiger, K. P. Pruessmann, C. Leussler, P. Röschmann, and P. Boesiger, "Specific coil design for SENSE: a six-element cardiac array," *Magn. Reson. Med.*, vol. 45, no. 3, pp. 495–504, Mar. 2001.

[81] D. I. Hoult, D. Foreman, G. Kolansky, and D. Kripiakevich, "Overcoming high-field RF problems with non-magnetic Cartesian feedback transceivers.," *MAGMA*, vol. 21, no. 1–2, pp. 15–29, 2008.

[82] I. R. O. Connell, K. M. Gilbert, M. A. Abou-Khousa, and R. S. Menon, "Design of a parallel transmit head coil at 7T with magnetic wall distributed filters," *IEEE Trans. Med. Imaging*, vol. 34, no. 4, pp. 836–845, 2015.

[83] I. R. O. Connell, K. M. Gilbert, M. A. Abou-Khousa, and R. S. Menon, "MRI RF array decoupling method with magnetic wall distributed filters," *IEEE Trans. Med. Imaging*, vol. 34, no. 4, pp. 825–835, 2015.

[84] B. Wu, P. Qu, C. Wang, J. Yuan, and G. X. Shen, "Interconnecting L/C components for decoupling and its application to low-field open MRI array," *Concepts Magn. Reson. Part B Magn. Reson. Eng.*, vol. 31, no. 2, pp. 116–126, Apr. 2007.

[85] C. D. Constantinides, E. Atalar, and E. R. McVeigh, "Signal-to-noise measurements in magnitude images from NMR phased arrays," *Magn. Reson. Med.*, vol. 38, no. 5, pp. 852–857, 1997.

[86] M. Kozlov and R. Turner, "Influence of a Dielectric Insert of High Permittivity on the Transmit Performance of a 300 MHz Multi-channel MRI Loop Array," *PIERS online*, pp. 116–120, 2011.

[87] J. Hong and M. J. Lancaster, "Microstrip Filters for RF / Microwave," vol. 7, pp. 0–471, 2001.

[88] K. J. Chang and I. R. Kamel, "Abdominal imaging at 3T: Challenges and solutions," *Appl. Radiol.*, vol. 39, no. 10, 2010.

[89] C. J. Snyder, L. DelaBarre, G. J. Metzger, P.-F. van de Moortele, C. Akgun, K. Ugurbil, and J. T. Vaughan, "Initial results of cardiac imaging at 7 tesla," *Magn. Reson. Med.*, vol. 61, no. 3, pp. 517–524, Mar. 2009.

[90] G. J. Metzger, C. Snyder, C. Akgun, T. Vaughan, K. Ugurbil, and P.-F. Van de Moortele, "Local B1+ shimming for prostate imaging with transceiver arrays at 7T based on subject-dependent transmit phase measurements," *Magn. Reson. Med.*, vol. 59, no. 2, pp. 396–409, Feb. 2008.

[91] A. de Boer, J. M. Hoogduin, P. J. Blankestijn, X. Li, P. R. Luijten, G. J. Metzger, A. J. E. Raaijmakers, L. Umutlu, F. Visser, and T. Leiner, "7 T renal MRI: challenges and promises," *Magn. Reson. Mater. Physics, Biol. Med.*, vol. 29, no. 3, pp. 1–17, 2016.

[92] T. S. Ibrahim, A. Kangarlu, and D. W. Chakeress, "Design and performance issues of RF coils utilized in ultra high field MRI: Experimental and numerical evaluations," *IEEE*

Trans. Biomed. Eng., vol. 52, no. 7, pp. 1278–1284, 2005.

[93] J. T. Vaughan, G. Adriany, M. Garwood, E. Yacoub, T. Duong, L. DelaBarre, P. Andersen, and K. Ugurbil, "Detunable transverse electromagnetic (TEM) volume coil for high-field NMR," *Magn. Reson. Med.*, vol. 47, no. 5, pp. 990–1000, May 2002.

[94] J. T. Vaughan, G. Adriany, C. J. Snyder, J. Tian, T. Thiel, L. Bolinger, H. Liu, L. DelaBarre, and K. Ugurbil, "Efficient high-frequency body coil for high-field MRI.," *Magn. Reson. Med.*, vol. 52, no. 4, pp. 851–9, Oct. 2004.

[95] J. Vaughan, "Transmitter Arrays for Cardiac Imaging at 7T," *Proc. ISMRM 17th ISMRM*, pp. 1–4, 2009.

[96] J. Tian, R. Lagore, and J. T. Vaughan, "Design Considerations for Dipole for Head MRI at 10.5T," in *IEEE MTT-S 2015 International Microwave Workshop Series on RF and Wireless Technologies for Biomedical and Healthcare Applications (IMWS-BIO), Taipei,* 2015, pp. 99–100.

[97] A. J. E. Raaijmakers, O. Ipek, D. W. J. Klomp, C. Possanzini, P. R. Harvey, J. J. W. Lagendijk, and C. A. T. Van Den Berg, "Design of a radiative surface coil array element at 7 T: The single-side adapted dipole antenna," *Magn. Reson. Med.*, vol. 66, no. 5, pp. 1488–1497, 2011.

[98] A. J. E. Raaijmakers, M. Italiaander, I. J. Voogt, P. R. Luijten, J. M. Hoogduin, D. W. J. Klomp, and C. A. T. van den Berg, "The fractionated dipole antenna: A new antenna for body imaging at 7 Tesla," *Magn. Reson. Med.*, vol. 1374, pp. 1366–1374, 2016.

[99] L. Winter, C. Ozerdem, W. Hoffmann, D. Santoro, A. MUller, H. Waiczies, R. Seemann, A. Graessl, P. Wust, and T. Niendorf, "Design and Evaluation of a Hybrid Radiofrequency Applicator for Magnetic Resonance Imaging and RF Induced Hyperthermia: Electromagnetic Field Simulations up to 14.0 Tesla and Proof-of-Concept at 7.0 Tesla," *PLoS One*, vol. 8, no. 4, 2013.

[100] L. Winter, C. Oezerdem, W. Hoffmann, T. van de Lindt, J. Periquito, Y. Ji, P. Ghadjar, V. Budach, P. Wust, and T. Niendorf, "Thermal magnetic resonance: physics considerations and electromagnetic field simulations up to 23.5 Tesla (1GHz).," *Radiat. Oncol.*, vol. 10, no. 1, p. 201, 2015.

[101] D. Oloumi, P. Mousavi, M. I. Pettersson, and D. G. Elliott, "A Modified TEM Horn Antenna Customized for Oil Well Monitoring Applications," *IEEE Trans. Antennas Propag.*, vol. 61, no. 12, pp. 5902–5909, Dec. 2013.

[102] Constantine A. Balanis, *Antenna Theory Analysis and Design Third Edition*, no. 3. 2005.

[103] A. Kolokotronis, Y. Huang, and J. T. Zhang, "Design of TEM Horn Antennas for Impulse

Radar," no. September, pp. 120–126, 1999.

[104] B. Van Den Bergen, C. A. T. Van Den Berg, D. W. J. Klomp, and J. J. W. Lagendijk, "SAR and power implications of different RF shimming strategies in the pelvis for 7T MRI," *J. Magn. Reson. Imaging*, vol. 30, no. 1, pp. 194–202, 2009.

[105] A. Note, "Agilent Basics of Measuring the Dielectric Properties of Materials," *Meas. Tech.*, vol. 2007, p. 32, 2005.

[106] U. Kaatze, "Measuring the dielectric properties of materials. Ninety-year development from low-frequency techniques to broadband spectroscopy and high-frequency imaging," *Meas. Sci. Technol.*, vol. 24, no. 1, p. 012005, Jan. 2013.

[107] L. L. and K. R. Kevin K.M. Chan, Adrian Eng-Choon Tan, "Material Characterization of Arbitrarily Shaped Dielectrics based on Reflected Pulse Characteristics," *IEEE Trans. Microw. Theory Tech.*, 2014.

[108] O. V Tereshchenko, F. J. K. Buesink, and F. B. J. Leferink, "An overview of the techniques for measuring the dielectric properties of materials," in *General Assembly and Scientific Symposium, URSI*, 2011, pp. 1–4.

[109] P. A. Bottomley, "A technique for the measurement of tissue impedance from 1 t o 100 MHz using a vector impedance meter," *J. Phys. E.*, vol. 11, no. 5, pp. 413–414, 1978.

[110] D. R. Lide, "'Permittivity (Dielectric constant) of water at various frequencies' in CRC Handbook of Chemistry and Physics," *CRC Press. Boca Raton, FL*, p. 3485.

[111] A. Sihvola, "Mixing rules with complex dielectric coefficients," *Subsurf. Sens. Technol. Appl.*, vol. 1, no. 4, pp. 393–415, 2000.

[112] S. R. Gough, "A Low Temperature Dielectric Cell and the Permittivity of Hexagonal Ice to 2 K," *Can. J. Chem.*, vol. 50, no. 18, pp. 3046–3051, 1972.

[113] B. a Mazzeo, S. Chandra, B. L. Mellor, and J. Arellano, "Temperature-stable parallel-plate dielectric cell for broadband liquid impedance measurements," *Rev. Sci. Instrum.*, vol. 81, no. 12, p. 125103, Dec. 2010.

[114] T. T. Grove, M. F. Masters, and R. E. Miers, "Determining dielectric constants using a parallel plate capacitor," *Am. J. Phys.*, vol. 73, no. 1, p. 52, 2005.

Appendix A

Permittivity Measurement of Liquids, Powders and Suspensions using a Parallel-Plate Cell[5]

A.1. Introduction

The measurement of the dielectric properties of materials is of significant importance in science and engineering, and numerous techniques have been developed to perform permittivity measurements over different ranges of frequencies [105], [106]. In the transmission line method, a sample of material is placed inside a section of a transmission line (waveguide or coaxial) and the permittivity (and permeability) are deduced from the transmission line's scattering (S) parameters. This is a broadband technique [105] but the mechanical construction of the transmission line is challenging. Similarly, a resonant cavity can also be used to measure permittivity by inserting a sample of the material and measuring the spectrum of resonances. While simpler in construction, it is a narrow band technique and is applicable only to low-loss materials. In the free-space method, electromagnetic waves are sent to a flat sample and the material's permittivity is deduced from the reflected signal. This technique requires a large, flat sample of material and is applicable at high frequencies (1 GHz or more) due to wavelength limits on minimum sample size [105], [107]. Coaxial probe methods are those most commonly used at radio frequencies because only a contact with the material is required and they are applicable over a large frequency range (approximately 100 MHz to 100 GHz). However, coaxial probes lose accuracy at the lower end of the frequency range and can be used only for isotropic and homogeneous materials such as liquids, or solids with a flat surface. They are also not simple to make, while most commercial versions are aimed at higher frequencies and can only work with specific network analyzers.

[5] This section is published as A. Kordzadeh, N. De Zanche, "Permittivity Measurement of Liquids, Powders, and Suspensions Using a Parallel-Plate Cell", Concepts in Magnetic Resonance Part B: Magnetic Resonance Engineering, 46, 1; 19-24; 2016, DOI: 10.1002/cmr.b.21318.

This work describes the parallel-plate (capacitive) technique, which consists of sandwiching the sample between electrodes and measuring the impedance of the resulting capacitor [105]. The method is simple, accurate, and is applicable at the relatively low frequencies encountered in MRI (well below 64 MHz to 400 MHz) [108]. We apply the parallel-plate technique to ceramic powders and suspensions which can have relative permittivities of 100 or more. While coaxial probes are sensitive to local inhomogeneities in the material or occasional air bubbles, the parallel-plate cell is largely insensitive to these imperfections.

A.2. Methods

A.2.1. Construction

The parallel-plate cell used in this work, shown in Figure A.1, consists of two circular copper electrodes 30 mm in diameter, etched on FR4 circuit board and separated by a 6-mm-thick acrylic (PMMA) flange. One of the plates is glued to the flange and a connecting lead is soldered near the edge of each electrode to minimize connection lengths. A rubber O-ring provides a tight seal between the second plate and the flange when the six nylon screws are tightened to prevent leakage of liquids.

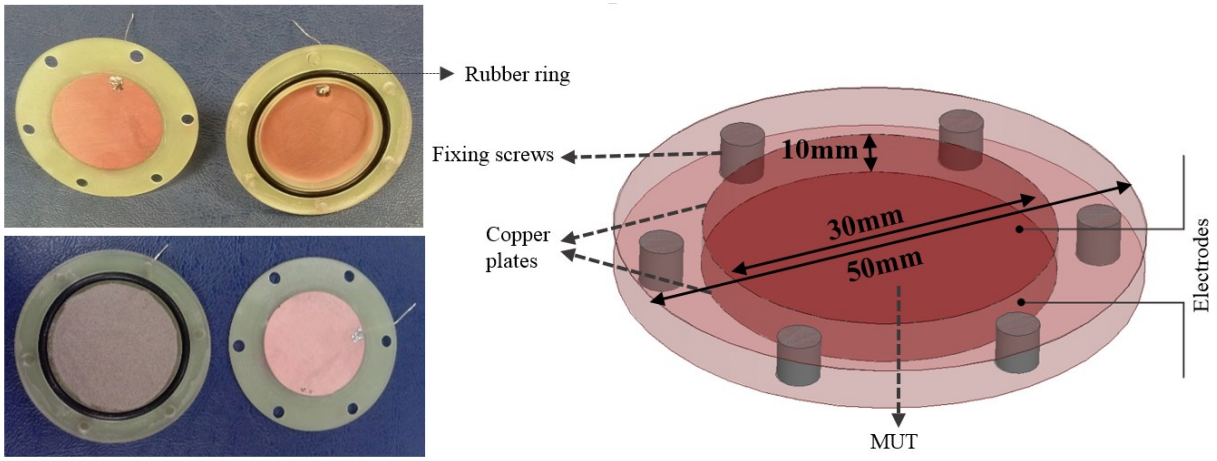

Figure A.1. Parallel plate cell: (a) drawing and dimensions, (b) fabricated prototype.

A.2.2. Theory

Equivalent circuits of the cell filled with a dielectric of unknown permittivity, including parasitics from the measurement setup, are shown in Figure A.2, including the one proposed in [109] and a modified version.

Series or parallel resistances (R_s and R_p, respectively) and inductances (L_s and L_p) are mostly due to the test set up while R_d is dominated by the losses in the material under test (MUT). Total capacitance $C = C_0 + C_d$ is the combination of that of the empty cell (C_0) and MUT (C_d). The impedance of the circuits shown in Figure A.2 are given, respectively by

$$Z_{in}(\omega) = R_s + j\omega L_s + \frac{R_d}{1+j\omega C R_d},$$

and

$$Z_{in}(\omega) = \frac{1}{\frac{1}{R_{P1}} + \frac{1}{j\omega L_P} + j\omega C_P} + \frac{R_d}{1 + j\omega C R_d}. \quad \text{(A.1)}$$

Impedance measurements are performed at a number of frequencies and the circuit parameters are obtained by least-squares fitting to these equations in MATLAB (The Mathworks, Natick, MA) using the *fminsearch* function. Alternatively, the freely-available Zfit program (http://www.exality.com/blog/fitting-equivalent-circuits-to-impedance-data/) provides the same functionality with a user-friendly interface and additional equivalent circuit models.

A.2.3. Calibration and Measurement

The relative permittivity and conductivity (in general, complex permittivity $\varepsilon = \varepsilon_r - i\varepsilon''$) of the MUT are related to C_d and R_d , respectively, according to [105]

$$\varepsilon_r = C_d \left(\varepsilon_0 \frac{A}{d}\right)^{-1} = C_d K^{-1} \quad \text{(A.2)}$$

and

$$\sigma = \omega \cdot \varepsilon'' = \frac{1}{R_d}\left(\frac{d}{A}\right) = \frac{1}{K' \cdot R_d}. \quad \text{(A.3)}$$

Here K is the parallel-plate constant (in units of Farads) which depends on the cell's dimensions and $K' = \frac{K}{\varepsilon_0}$. All other circuit parameters are assumed to be constant. To find K and C_0 (stray capacitance due to edge fields through the PMMA flange), at least two materials with known dielectric properties are needed for calibration. In this work we chose air (empty cell, ε_r=1) and deionized water (ε_r=78.36 at 100 MHz and 25°C [110]) due to its availability and large permittivity. Introducing appropriate subscripts in (A.2) for the standard materials and rearranging we obtain

$$K = \frac{C_{Water} - C_{Air}}{\varepsilon_{Water} - \varepsilon_{Air}} \tag{A.4}$$

and

$$C_0 = C_{Air} - K \cdot \varepsilon_{r(air)}. \tag{A.5}$$

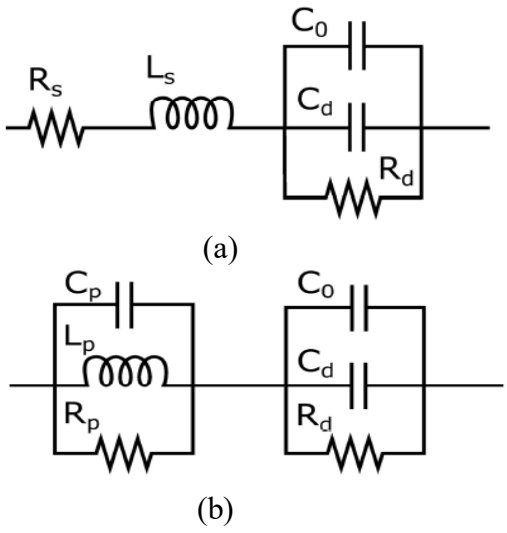

Figure A.2. Equivalent circuits for the capacitive measurement cell. (a) standard circuit used in [109] and (b) modified circuit that improves fits in high-loss or high-permittivity materials.

The cell's interior space is then filled with the material of interest (liquid, powder or suspension) and the cap is sealed by tightening the screws. Impedance of the cell is measured over the 10–300 MHz frequency range using the common Agilent 4396B combination analyzer in impedance

analyzer mode through a 43961A impedance test adapter and 16092A test fixture (Figure A.3). Data are saved and exported for further processing on a PC as described in the **Theory**.

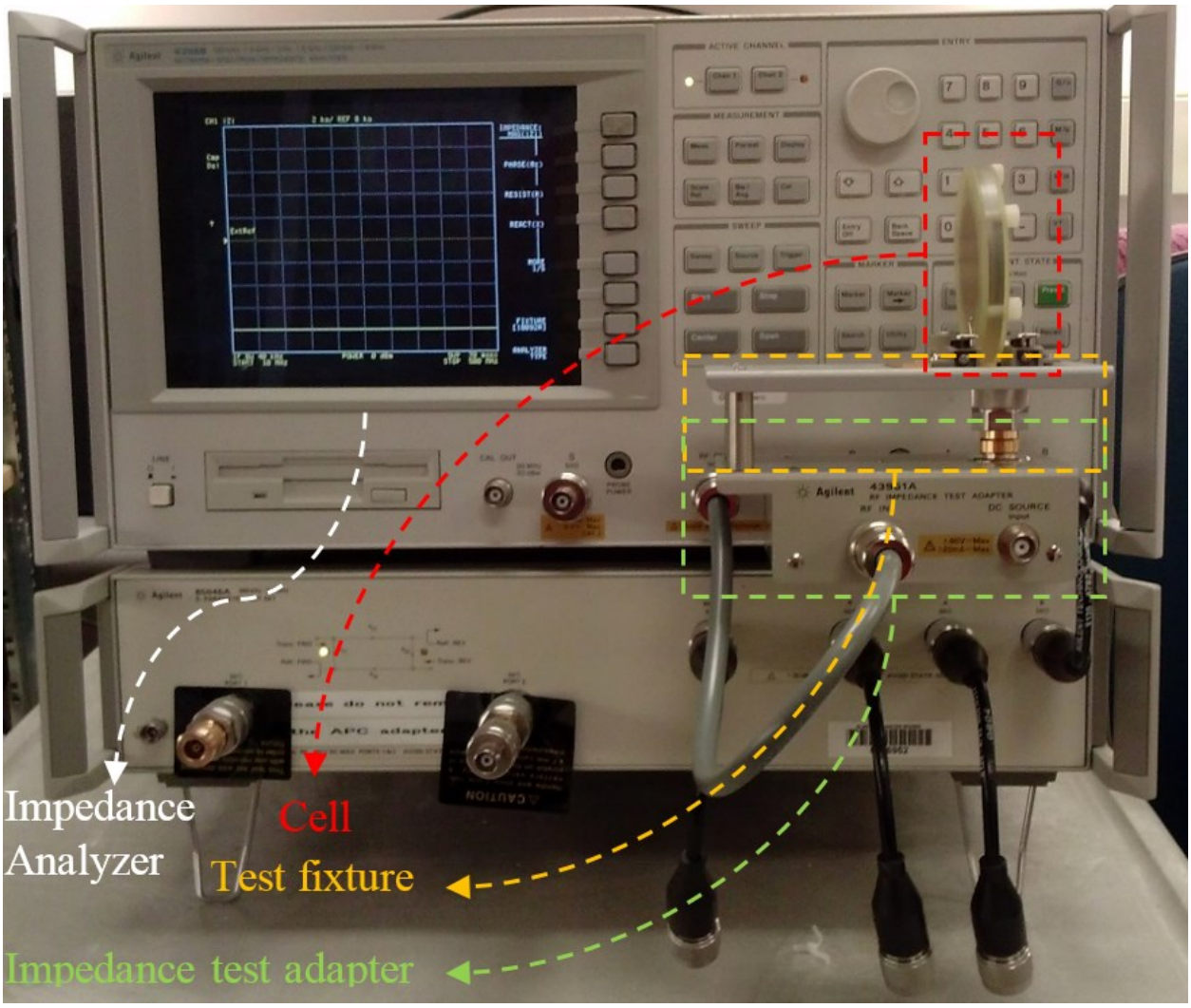

Figure A.3. Impedance measurement setup, including Agilent 4396B combination analyzer, 43961A impedance test adapter and 16092A test fixture.

A.2.4. Materials

Measurements on powders, liquids and suspensions were performed, including 220-mesh alumina (Al_2O_3, Manus Abrasive Systems Inc.) and much finer $BaTiO_3$ (superscript A: Fisher Scientific, superscript B: Alfa Aesar, MA, USA). These ceramics in powder form have much lower bulk permittivity than the corresponding solid form due to presence of air between powder particles. Furthermore, the permittivity is strongly dependent on the grain size [56]. To eliminate

the effect of air between particles, the powder is mixed with varying amounts of demineralized water to achieve suspensions. Using Lichtenecker's logarithmic power law [111],

$$\varepsilon_r^{eff} = {\varepsilon_{rp}}^f \times \varepsilon_{rw}^{(1-f)} \ , \tag{A.6}$$

we can determine the permittivity of the solid ε_{rp} by knowing the volume fraction, f, the measured permittivity of the suspension ε_r^{eff}, and that of the liquid (water), ε_{rw}. The volume fraction is determined by measuring the masses of the two components and their respective densities.

Methanol, demineralized water and 4, 20, and 40 mM solutions of sodium chloride were also measured. However, there can be inaccurate permittivity measurements in such high-conductivity liquids due to electrolytic polarization that results from the ions in the dielectric-electrode boundary of the parallel-plate cell [106], [112], [113]. Also, as conductivity of the material under test increases, the phase angle of the complex permittivity will be larger and the real part of the permittivity will be more difficult to resolve [114]. To have detectable capacitance and avoid excessive stray fields, a small gap between plates is preferred but this enhances electrolytic polarization effects [109], [114].

A.2.5. Comparison to Coaxial Probes

The accuracy of the capacitive cell was evaluated by comparing the measurements to those obtained using coaxial probes from both Keysight (Santa Rosa, CA, USA) and Keycom (Tokyo, Japan). The Keysight 85070E Dielectric Probe Kit was connected to an Agilent E8362B network analyzer while the Keycom DPS16 (3.6 mm diameter) Open Mode Probe was connected to a Rohde and Schwarz ZVA67. The probes were immersed in the material taking care to avoid trapping air pockets or bubbles near the probe's sensitive volume (end of the coaxial line). This proved most challenging for the Keycom probe because its sensitive area is slightly recessed within the surrounding ground electrode.

A.3. Results and Discussion

The measured and fitted impedance (resistance, *R*, and reactance, *X*) is shown in Figure A.4 for some representative materials. As expected, the cell is capacitive over the chosen frequency

range for materials with relatively low permittivity, while for higher permittivities the large capacitance and small inductance become resonant and the impedance is inductive at higher frequencies. In such cases fitting using the model of Figure A.2 (a) must be confined to smaller frequencies in the capacitive region to avoid errors (Figure A.4 (c) and (d)), or a modified circuit model such as that in Figure A.2 (b) must be used. Calibration constants for the cell obtained from air and water measurements are K = 3.22 pF and C_0 = 2.29 pF. Complete complex permittivity results of the three measurement methods are listed in Table A.1.

Table A.1. Complex permittivity measured using the dielectric cell and coaxial probes at 100 MHz.

Material	**Agilent probe ε**	**Keycom probe ε**	**Dielectric Cell ε**
$BaTiO_3^A$ powder	3.66+j0.07	2.50-j0.09	6.14+j0.15
$BaTiO_3^B$ powder	3.36+j0.08	13.8-j0.93	8.97+j0.15
Al_2O_3 powder	3.03+j0.04	2.82+j0.15	2.64+j0.087
Demineralized water	78.4-j0.75	80.1-j0.51	78.5-j1.45
Methanol	33.5-j1.92	33.6-j1.98	31.5-j1.04
Saline 4 mM	77.4-j40.5	78.9-j40.2	72.3-j10.0
Saline 20 mM	74.3-j316	74.9-j319	103-j589
Saline 40 mM	73.2-j541	75.9-j574	177-j1619
f=0.5 alumina suspension	41. 8-j5.82	41.1-j3.64	33.5-j3.23
f=0.53 alumina suspension	37.1-j4.16	26.8-j2.44	26.5-j1.85
f=0.353 $BaTiO_3^A$ suspension	284-j184	221-j89.6	261-j15.6
f=0.42 $BaTiO_3^A$ suspension	327-j206	216-j78.6	280-j17.0
f=0.353 $BaTiO_3^B$ suspension	271-j29.1	228-j17.4	265-j19.6
f=0.246 $BaTiO_3^B$ suspension	120-j30.5	179-j13.3	177-j14.4

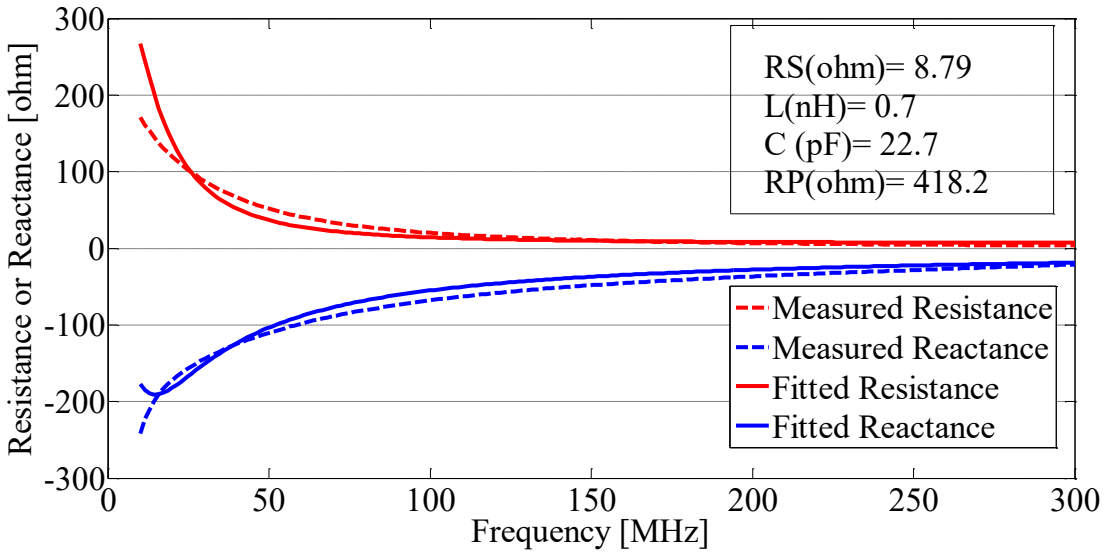
RS(ohm)= 8.79
L(nH)= 0.7
C (pF)= 22.7
RP(ohm)= 418.2
Measured Resistance
Measured Reactance
Fitted Resistance
Fitted Reactance
Resistance or Reactance [ohm]
Frequency [MHz]
300
200
100
0
-100
-200
-300
0
50
100
150
200
250
300

(a)

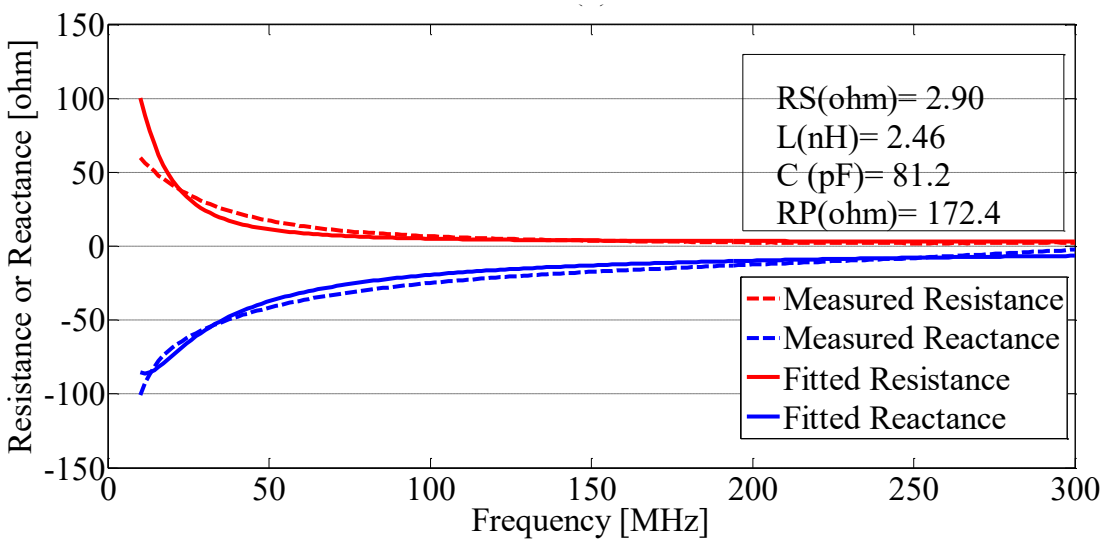
RS(ohm)= 2.90
L(nH)= 2.46
C (pF)= 81.2
RP(ohm)= 172.4
Measured Resistance
Measured Reactance
Fitted Resistance
Fitted Reactance
Resistance or Reactance [ohm]
Frequency [MHz]
150
100
50
0
-50
-100
-150
0
50
100
150
200
250
300

(b)

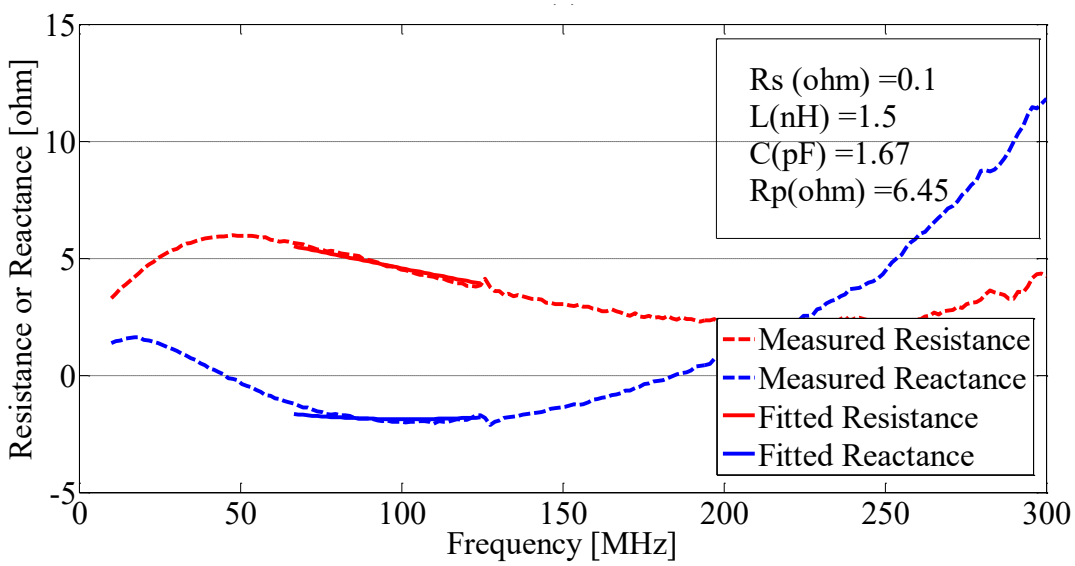

(c)

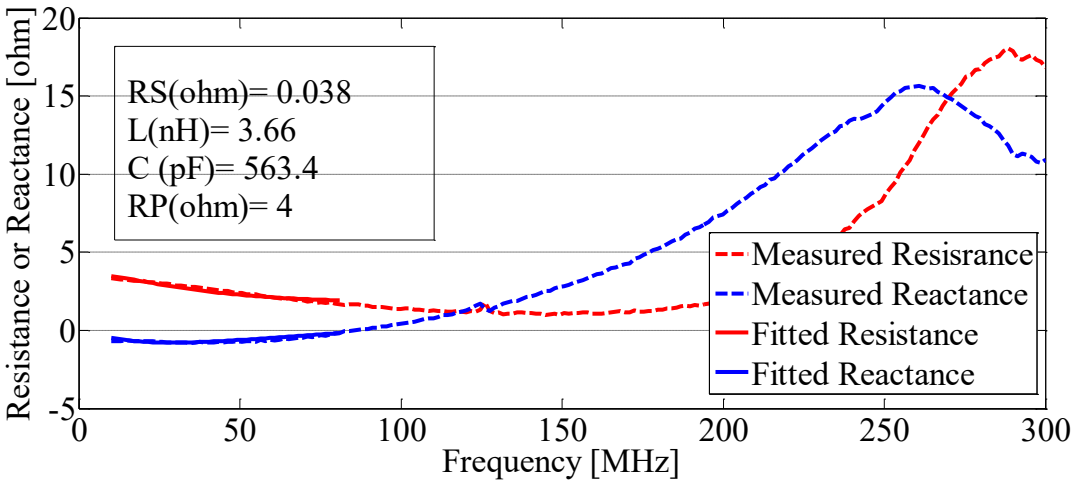

(d)

Figure A.4. Resistance and reactance measured (dash) and fitted (solid) for some representative samples (a) $BaTiO_3^A$ powder, (b) methanol, (c) 4 mM saline, (d) f=0.353 $BaTiO_3^B$ suspension. Fitting results for the model of Figure A. 2(a) are shown within rectangles and the corresponding frequency range is indicated by the support of the solid black lines. Improved fitting results for (c) and (d) are obtained using the model of Figure A. 2. (b) (black dash-dot lines).

For powders, the permittivity of the solid material is calculated from that of its suspension in water ($\varepsilon_{rw} = 78.5$) by knowing the volume fraction and applying (A.5). (Table A.2). The real part of the permittivity is compared graphically in Figure. A.5 and Figure A.6, while Figure A.6. (b) shows the loss tangent ($tan\ \delta = {\varepsilon^{"}}/{\varepsilon_r}$) of each material.

Table A.2. Volume fractions and permittivity (real part) of the dry powders.

	Al_2O_3	**$BaTiO_3{}^A$**	**$BaTiO_3{}^B$**
Mass density (g/mL)	Appx. 4.0	6.08	5.85
Volume fraction ($f=V_{powder}/V_{total}$)	0.5	0.35	0.35
Calculated ε_r of the solid material	14.25	2360.3	2464.6

Agreement between the methods is excellent with the exception of powders and saline solutions. Discrepancies for $BaTiO_3$ powders are expected because of the difficulty of maintaining the same amount of packing among the three measurements, while those for saline solutions are due to electrolytic polarization as discussed in Materials. No systematic differences were found between the results from the dielectric cell and those from the coaxial probes. For powders and saline, the differences between the two coaxial probes are of the same order as differences between the dielectric cell and the coaxial probes.

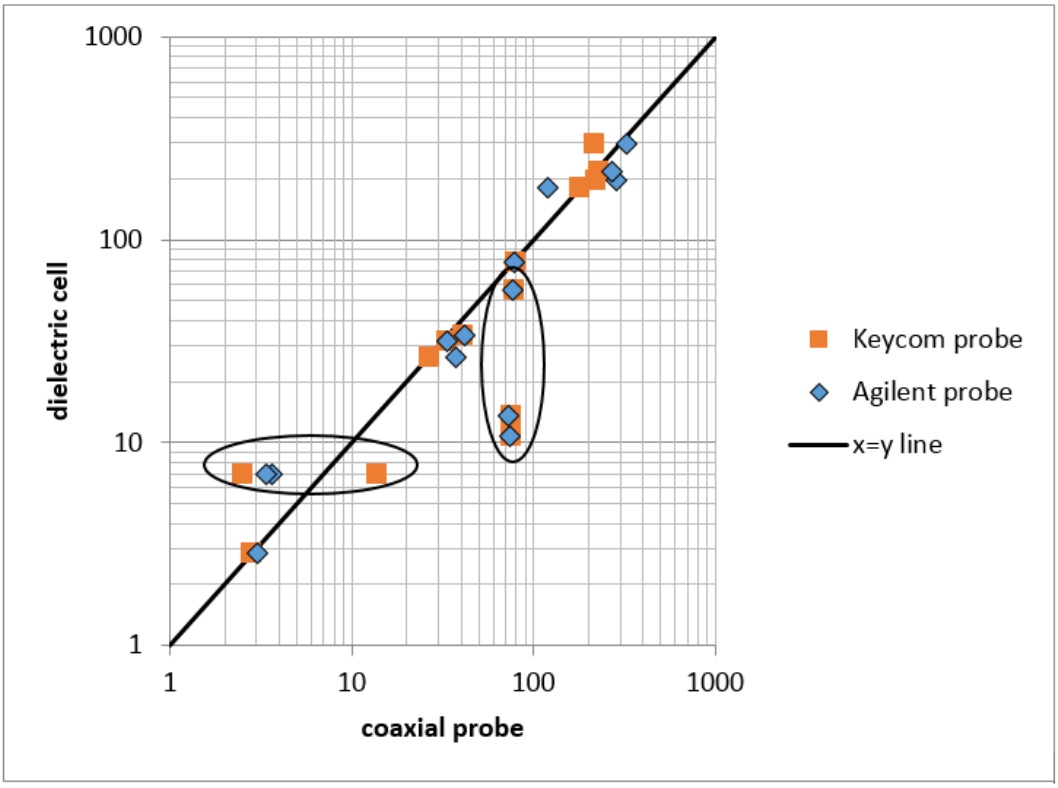

Figure A.5. Comparison between cell (model in Figure 2a) and coaxial probe measurements of real permittivity (ε_r) at 100 MHz. Agreement is excellent with the exception of powders and saline solutions (horizontal and vertical ellipses, respectively).

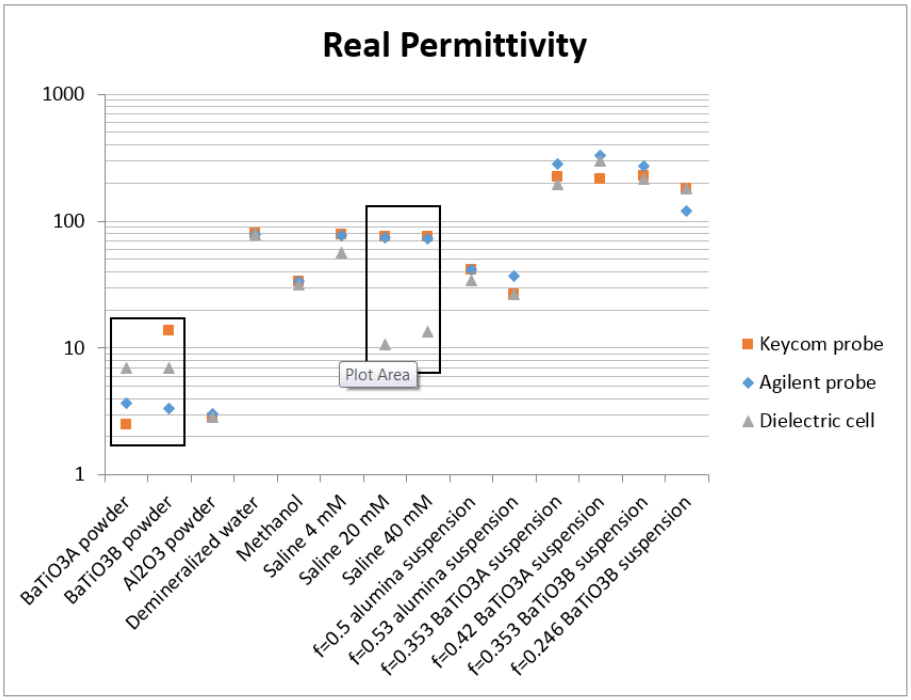
Real Permittivity
1000
100
10
1
Plot Area
Keycom probe
Agilent probe
Dielectric cell
BaTiO3A powder
BaTiO3B powder
Al2O3 powder
Demineralized water
Methanol
Saline 4 mM
Saline 20 mM
Saline 40 mM
f=0.5 alumina suspension
f=0.53 alumina suspension
f=0.353 BaTiO3A suspension
f=0.42 BaTiO3A suspension
f=0.353 BaTiO3B suspension
f=0.246 BaTiO3B suspension

(a)

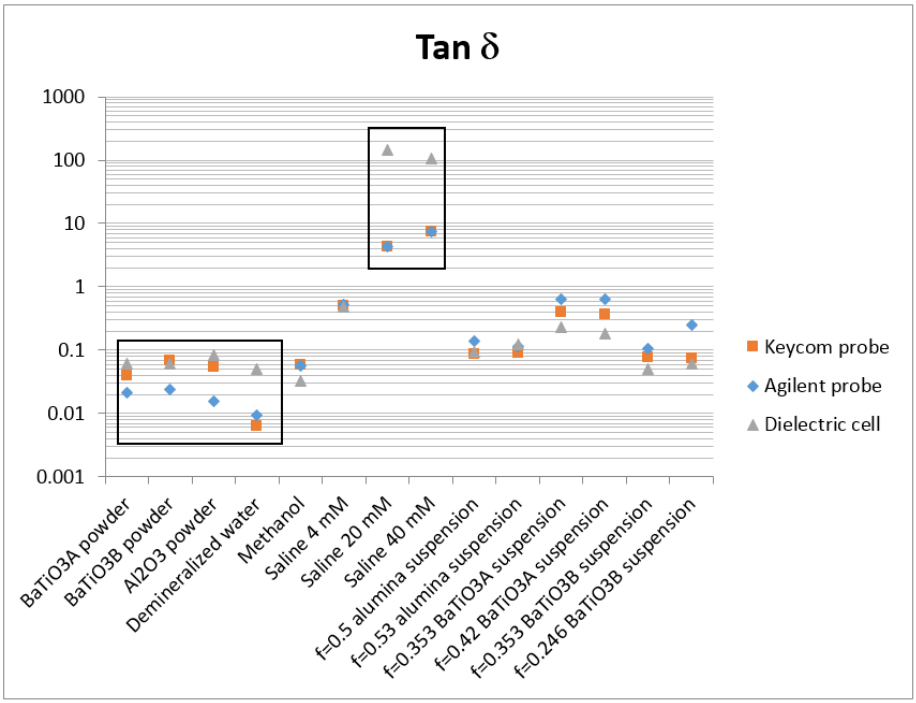
Tan δ
1000
100
10
1
0.1
0.01
0.001
Keycom probe
Agilent probe
Dielectric cell
BaTiO3A powder
BaTiO3B powder
Al2O3 powder
Demineralized water
Methanol
Saline 4 mM
Saline 20 mM
Saline 40 mM
f=0.5 alumina suspension
f=0.53 alumina suspension
f=0.353 BaTiO3A suspension
f=0.42 BaTiO3A suspension
f=0.353 BaTiO3B suspension
f=0.246 BaTiO3B suspension

(b)

Figure A.6. Comparison of (a) real permittivity and (b) loss tangent $(\tan \delta)$ for each material at 100 MHz. Dielectric cell measurements use the model in Figure A.2 (a). Largest differences are highlighted in rectangles.

A.4. Conclusions

Measurement of the complex permittivity of powders and suspensions can be challenging with standard coaxial probes due to the common presence of inhomogeneities within the sample and air gaps between the probe and sample. The dielectric cell presented in this work is simple to fabricate and gives results that are comparable to those from coaxial probes over a wide range of materials. While coaxial probes lose accuracy at lower frequencies, the dielectric cell can be readily fabricated to operate at any frequency of interest in MRI and works with any impedance analyzer. The sensitive volume is larger than that of coaxial probes and therefore skewed results due to settling, bubbles or inhomogeneities are less likely. The dielectric cell is therefore well-suited for suspensions used for high-dielectric-constant pads.

Results show that measurements from different coaxial probes can differ as much as those between the dielectric cell and coaxial probes. Therefore, we conclude that the accuracy of the dielectric cell method is comparable to that of coaxial probes. Electrolytic polarization effects in ionic liquids can be reduced or prevented by using platinum electrodes, by adding insulating layers, or by using a larger gap between the electrodes.